ISTANBUL TECHNICAL UNIVERSITY ★ GRADUATE SCHOOL OF SCIENCE ENGINEERING AND TECHNOLOGY

MODELLING, ANALYSIS AND EXPERIMENTAL VALIDATION OF VIBRATION OF ELECTRIC MOTORS

M.Sc. THESIS

Deniz BİLGİLİ

Department of Mechanical Engineering

Machine Dynamics, Vibration & Acoustics Programme

DECEMBER 2018

ISTANBUL TECHNICAL UNIVERSITY ★ GRADUATE SCHOOL OF SCIENCE ENGINEERING AND TECHNOLOGY

MODELLING, ANALYSIS AND EXPERIMENTAL VALIDATION OF VIBRATION OF ELECTRIC MOTORS

M.Sc. THESIS

Deniz BİLGİLİ
(503161403)

Department of Mechanical Engineering

Machine Dynamics, Vibration & Acoustics Programme

Thesis Advisor: Prof. Dr. Kenan Yüce ŞANLITÜRK

DECEMBER 2018

ISTANBUL TEKNİK ÜNİVERSİTESİ ★ FEN BİLİMLERİ ENSTİTÜSÜ

ELEKTRİK MOTORLARININ TİTREŞİMLERİNİN MODELLENMESİ, ANALİZİ VE DENEYSEL OLARAK DOĞRULANMASI

YÜKSEK LİSANS TEZİ

Deniz BİLGİLİ
(503161403)

Makine Mühendisliği Anabilim Dalı

Makina Dinamiği, Titreşim ve Akustiği Programı

Tez Danışmanı: Prof. Dr. Kenan Yüce ŞANLITÜRK

ARALIK 2018

Deniz Bilgili, an M.Sc. student of İTU Graduate School of Science Engineering and Technology with student ID 503161403, successfully defended the thesis entitled "Modelling, Analysis and Experimental Validation of Vibration of Electric Motors", which he prepared after fulfilling the requirements specified in the associated legislations, before the jury whose signatures are below.

Thesis Advisor : **Prof. Dr. Kenan Yüce Şanlıtürk** ....
İstanbul Technical University

Jury Members : **Prof. Dr. Vahit Mermertaş** ....
İstanbul Technical University

Dr. Egemen Tınar ....
Arçelik A.Ş.

Date of Submission : 12 November 2018
Date of Defense : 03 December 2018

To my mother, father and brother,

FOREWORD

Firstly, I would like to thank my friends and colleagues Emre HAS and Burak Taha KEKLİK for helping me with preparing the parts needed for the tests, Tunç KARAÇALI for helping me with building up the necessary test setup and conducting the tests. Additionally, I would like to thank dear Metin GÜL, the manager of Machine Dynamics & Cleaning Technologies Division of Arçelik A.Ş. R&D Centre, for providing necessary test equipment and test space, dear Kutay EDİS, the manager of Digital Modelling & Structural Design Division of Arçelik A.Ş. R&D Centre, for sharing with me his technical and non-technical knowledge and experience throughout the thesis work and proving me guidance and mentorship.

Secondly, I would like to send my highest gratitude to my thesis advisor, Prof. Kenan Yüce ŞANLITÜRK, for not only his continuous support and guidance both with theory and practice, but also for being a visionary and sharing his vision not just in my field but also in other fields and helping me gain a much deeper insight into mechanical engineering. His work ethics, discipline and patience have been a great example for me to learn that an engineer should not only possess technical skills, but also these virtues which complete the philosophy of engineering.

Finally, I would like to send my love and thanks to my family, my mother, my father and my brother, for always being there for me and supporting me through all difficulties in my thesis work and in life.

December 2018 | Deniz BİLGİLİ
(Mechanical Engineer)

TABLE OF CONTENTS

Page

FOREWORD .... **ix**
TABLE OF CONTENTS .... **xi**
ABBREVIATIONS .... **xiii**
SYMBOLS .... **xv**
LIST OF TABLES .... **xix**
LIST OF FIGURES .... **xxi**
SUMMARY .... **xxv**
ÖZET .... **xxvii**
1. INTRODUCTION **1**
1.1 Definition of the Problem 1
1.2 Literature Survey 2
1.3 Objectives and Scope of the Thesis 12
2. THEORY **15**
2.1 Electromagnetics 15
2.1.1 Electric field and electric force 15
2.1.2 Magnetic field and magnetic force 16
2.1.3 Electromagnetic field and electromagnetic force 18
2.1.4 Electromagnetic induction: Faraday’s Law and Lenz’s Law 19
2.2 Structure and Dynamics of Ball Bearings 21
2.2.1 General structure of deep-groove ball bearings 21
2.2.2 Load carrying characteristics of ball bearings 22
2.2.3 Rolling element – raceway contact mechanism in ball bearings 26
2.3 Theoretical and Experimental Modal Analysis 32
2.3.1 Experimental modal analysis 33
2.3.2 Theoretical modal analysis 35
2.4 Electric Motors 36
2.4.1 Direct current (DC) electric motors 36
2.4.2 Alternating current (AC) electric motors 38
2.4.3 Mechanical causes of noise and vibration in electric motors 39
2.4.4 Electrical causes of noise and vibration in electric motors 42
2.5 Component Mode Synthesis 44
2.6 Numerical Calculation of the Contact Forces in MSC Adams 46
3. TESTS AND MEASUREMENTS **47**
3.1 FRF Measurements of the Motor Components 48
3.2 Campbell Diagram Measurements 56
4. NUMERICAL MODELLING AND SIMULATIONS **63**
4.1 The Rotary Group 63
4.1.1 The bearing model 63
4.1.2 The rotor model 67
4.1.3 The flywheel model 68
4.2 The Nonrotary Group 69
4.2.1 Finite element model of the KT cover 70

4.2.2 Finite element model of the KTA cover 72
4.2.3 Finite element model of the stator 74
4.2.4 Finite element model of the nonrotary assembly 76
4.3 The Multibody Dynamic Model of the Atlas Motor 78
4.3.1 Modelling the electromagnetic excitations in the Atlas motor 80
4.3.2 Defining the motion and numerical integrator settings 81
5. COMPARISONS OF NUMERICAL AND EXPERIMENTAL RESULTS ... 83
5.1 The Effects of the Bearing Model on Predicted Steady-State Response of the Motor 83
5.2 Comparison of the Experimental and Numerical Steady-State Response Levels 85
5.3 Comparison of the Numerical and Experimental Campbell Diagrams and Overall Vibration Levels 88
5.4 Simulations of Motor with a Faulty Ball Bearing 91
6. CONCLUSIONS AND SUGGESTIONS FOR FUTURE WORK 95
6.1 Conclusions 95
6.2 Suggestions for Future Work 96
7. REFERENCES 99
CURRICULUM VITAE 103

ABBREVIATIONS

AC	: Alternating Current
BEM	: Boundary Element Method
BLDC	: Brushless DC Motor
BPF	: Ball Pass Frequency
BPFI	: Ball Pass Frequency Inner Race
BPFO	: Ball Pass Frequency Outer Race
BSF	: Ball Spin Frequency
C	: Coulombs
CAD	: Computer-aided Drawing
CPU	: Central Processing Unit
dB	: Decibels
DC	: Direct Current
DOF	: Degree of Freedom
EHD	: Elastohydrodynamic
EMF	: Electromotive Force
FE	: Finite Element
FEM	: Finite Element Method
FRF	: Frequency Response Function
FT	: Fourier Transform
FTF	: Fundamental Train Frequency
Hz	: Hertz
IRF	: Impulse Response Function

KT	: Belt Side (Turkish)
KTA	: Opposite of Belt Side (Turkish)
m	: Meters
MBD	: Multibody Dynamics
MBS	: Multibody System
mm	: Millimeters
N	: Newtons
RBE2	: Rigid Body Element
RPM	: Revolutions per minute
sec	: Seconds

SYMBOLS

E	: Magnitude of electric field of charged particle
k	: A constant equal to 8.99 x $10^9 \mathrm{Nm}^2/\mathrm{C}^2$
q	: Charge of particle
r	: Distance from charged particle
$\overrightarrow{\mathbf{F_e}}$	: Electric force vector
$\vec{\mathbf{E}}$	: Electric field vector
$\mathbf{F_e}$	: Magnitude of electric force
B	: Magnitude of magnetic field
$\boldsymbol{\mu_0}$	: Permeability of free space
I	: Magnitude of current
$\overrightarrow{\mathbf{F_B}}$	: Magnetic force vector
ν	: Charged particle's velocity
$\vec{\mathbf{B}}$	: Magnetic field vector
$\overrightarrow{\mathbf{F_{EB}}}$	: Electromagnetic field vector
$\boldsymbol{\Psi_L}$	: Half of the angular width of the load zone
Ψ	: Angular position of a rolling element
$\mathbf{c_d}$	: Bearing's radial clearance
$\mathbf{x_m}$	: Displacement of the inner ring with respect to the outer ring
ω	: Frequency of shaft rotation
N	: Number of balls in a ball bearing
d	: Ball diameter

$\mathbf{d_m}$	: Pitch diameter
$\mathbf{R_{in}}$	: Inner raceway radius
$\mathbf{R_{out}}$	: Outer raceway radius
$\mathbf{R}_i$	: Inner groove radius
$\mathbf{R_o}$	: Outer groove radius
$\boldsymbol{\alpha}$	: Contact angle
$\mathbf{F_c}$	: Hertzian contact force
$\mathbf{k_c}$	: Hertzian contact stiffness
$\boldsymbol{\delta}$	: Combined elastic deformation of contacting bearing elements
$\boldsymbol{\delta}*$	: Hertzian contact constant
$\boldsymbol{\rho}$	: Curvature of a surface in contact
$\sum \rho$	: Curvature sum of contacting surfaces
$\mathbf{t}$	: Time
$\mathbf{h(t)}$	: Impulse response function
$\mathbf{H(\omega)}$	: Frequency response function
$\mathbf{[K]}$	: Stiffness matrix
$\mathbf{[M]}$	: Mass matrix
$\boldsymbol{\omega_r}$	: r-th natural frequency of the system
$\mathbf{U_r}$	: r-th mode shape of the system
$\mathbf{[H]}$	: Frequency response function matrix
$[\boldsymbol{\Phi}]$	: Mass-normalised mode shape matrix
$\mathbf{N_s}$	: Synchronous speed
$\mathbf{F_L}$	: Line frequency
$\mathbf{P}$	: Number of stator poles
$\mathbf{N_{rotor}}$	: Rotor speed of electric motor

1X : 1 times the frequency of shaft rotation

$\mathbf{T_{cog}}$: Cogging torque

L : Axial dimension of the rotor of an electric motor

$\boldsymbol{\theta_s}$: Angular displacement of the stator

$\mathbf{B_r}$: Flux density of the inner surface of the stator

$\mathbf{B_\theta}$: Flux density of the outer surface of the stator

LIST OF TABLES

Page

Table 4.1: The geometric and material properties used for the calculation of the contact stiffnesses of the SKF 6202 bearing. **66**
Table 4.2: Comparison table of the numerical and experimental natural frequencies of the KT cover. **71**
Table 4.3: Comparison table of the numerical and experimental natural frequencies of the KTA cover. **73**
Table 4.4: Comparison table of the numerical and experimental natural frequencies of the stator. **75**
Table 4.5: Comparison table of the numerical and experimental natural frequencies of the nonrotary assembly. **78**

LIST OF FIGURES

Page

Figure 1.1: Finite element mesh used for the numerical approach in [2]. **2**
Figure 1.2: Finite Element (FE) model developed in [3] to calculate vibration amplitudes... **3**
Figure 1.3: The FE models of rotors used in [4].. **4**
Figure 1.4: The numerical procedure followed in [5] to calculate electromagnetic forces in the motor.. **5**
Figure 1.5: Numerical model used and the comparison of numerical and experimental results in [7]. **6**
Figure 1.6: Numerically-calculated field distribution in [12]. a) Traditional motor geometry. b) Proposed motor design with lower squeaking noise in the motor.. **7**
Figure 1.7: The elastic ball bearing model developed in [13]. **8**
Figure 1.8: The 4-DOF model developed in [15]. **9**
Figure 1.9: The numerical models of **a)** the deep-groove ball bearing and **b)** the bearing-shaft-rotor system developed in [19].. **11**
Figure 1.10: The simplified flexible numerical model for the outer ring of the ball bearing model presented in [20]. **12**
Figure 2.1: Electric field lines of positive and negative charges. **15**
Figure 2.2: Magnetic field lines sprouting from the north pole of the magnet and going into the south pole. **16**
Figure 2.3: Segregated magnetic field lines of the same poles of two magnets put next to one another. **17**
Figure 2.4: Direction of magnetic field created by current flow. **17**
Figure 2.5: Magnetic field (red) created by the changing electric field (blue). **18**
Figure 2.6: Electromagnetic force, F, on a charged particle. **19**
Figure 2.7: Experimental setup to observe electromagnetic induction. **20**
Figure 2.8: A magnetic field and current are induced as a result of increasing magnetic field through the loop.. **21**
Figure 2.9: Components of a deep-groove ball bearing [23]. **21**
Figure 2.10: Important geometric features of ball bearing [24, 25].......................... **22**
Figure 2.11: Load zone of a ball bearing [23]... **23**
Figure 2.12: Varying normal loads on different rolling elements of a ball bearing. Note that the inner ring is rotating counterclockwise [1, 26]. **24**
Figure 2.13: Point contact between a rolling element and the inner raceway. **26**
Figure 2.14: Elliptical contact area between the ball and the inner raceway. **27**
Figure 2.15: Combined deflection of the contacting rolling element and inner raceway as denoted with δ. **28**
Figure 2.16: Curvatures defined for a contacting pair with curved surfaces [28]. ... **30**
Figure 2.17: Values of the unitless constant $\delta *$ for various values of the curvature function, $F\rho$ [27, 29]. **31**
Figure 2.18: Routes in experimental and theoretical modal analysis in order to obtain spatial, modal and response models. **32**

Figure 2.19: A depiction of general experimental modal analysis procedure........... **34**
Figure 2.20: Modal hammers and shakers used for experimental modal analysis.... **35**
Figure 2.21: Electromagnetic forces and torque generated by a DC motor [1]. **37**
Figure 2.22: Torque generation mechanism in a typical brushless DC motor. **37**
Figure 2.23: The stator and rotor of an induction motor [1]. **38**
Figure 2.24: Spectrum of vibration due to unbalance [31]. **40**
Figure 2.25: Spectra of axial and radial vibrations caused by misalignment [31]. ... **40**
Figure 2.26: Eccentricity due to a, b) faults in mounting of the bearings; c) rotor faults; d) stator lamination faults [1]. **41**
Figure 2.27: Axial and radial vibrations caused by bent shaft [31]. **41**
Figure 2.28: Spectrum of vibrations caused by mechanical looseness [31]. **42**
Figure 2.29: Eccentric rotor and stator in an electric motor [1]. **43**
Figure 2.30: A generic finite element model of a system consisting of interconnected sub-structures [34]. **45**
Figure 2.31: A contact situation occurring in MSC Adams [36]. **46**
Figure 3.1: FRF measurement scenario for the front cover. **48**
Figure 3.2: Measured FRF of the front cover. **49**
Figure 3.3: a) Suspended KTA specimen for FRF measurement and b) one of the measured FRFs. **50**
Figure 3.4: a) Suspended stator specimen for FRF measurements and b) one of the measured FRFs. **52**
Figure 3.5: Horizontally suspended rotor. **53**
Figure 3.6: Apparent mass of the horizontally-suspended and axially-excited rotor. **53**
Figure 3.7: a) Vertically-suspended rotor and b) one of the FRF measurements using radial excitation. **54**
Figure 3.8: Suspended assembly of the front and rear covers and the stator. **55**
Figure 3.9: Measured FRF of the assembly without rotor. **56**
Figure 3.10: Manually-created damage on the raceway of the outer ring used in one of the bearings of a test specimen. **57**
Figure 3.11: One of the specimens used for Campbell Diagram measurements. **58**
Figure 3.12: Experimental Campbell diagrams for the specimens a) S1 and b) S2 (with damaged ball bearing). **59**
Figure 3.13: Spectrum of the measured steady-state acceleration of loaded motor at 10000 RPM. **60**
Figure 3.14: Sidebands around the 7X frequency with a gap of nearly 15 Hz. **61**
Figure 3.15: Trial sideband markers for identification of the number of sideband pairs around the 7X frequency. **62**
Figure 4.1: The contact lines used to define the contacts in the bearing model. An example contact definition between lines is shown as a spring-damper pair. **64**
Figure 4.2: The effect of the contact angle (α) on the radii of the contact circles. ... **65**
Figure 4.3: An example of Hertzian-based non-linear contact definition used in the ball bearing model in MSC Adams. **67**
Figure 4.4: Isometric view of the bearing model for the SKF 6202 bearing. **67**
Figure 4.5: The rigidbody model of the rotor. **68**
Figure 4.6: The ridigbody model of the flywheel. **69**
Figure 4.7: The finite element mesh generated for the KT cover to be used for its flexbody model. **70**

Figure 4.8: A comparison of the numerical and experimental FRFs of the KT cover. **71**
Figure 4.9: The finite element mesh generated for the KTA cover to be used for its flexbody model. **72**
Figure 4.10: A comparison of the numerical and experimental FRFs of the KTA cover. **73**
Figure 4.11: The finite element model of the stator. Purple indicates the armature material that estimates equivalent mass and stiffness for the armatures. Orange indicates steel. **74**
Figure 4.12: The numerically-computed shape of the third mode of the stator, which is an out-of-plane mode with respect to the measurement direction. .. **76**
Figure 4.13: A comparison of the numerical and experimental FRFs of the stator. . **76**
Figure 4.14: The finite element model of the nonrotary assembly. The beam model without pretension is used to model the screws to reduce the computation time. **77**
Figure 4.15: A comparison of the numerical and experimental FRFs of the nonrotary assembly. **78**
Figure 4.16: The flywheel, the inner rings of the bearings and the shaft as they are coupled at the corresponding interface nodes of the shaft (yellow, red and blue markers). **79**
Figure 4.17: The isometric view of the assembled multibody dynamic model of the Atlas motor. The black triangles indicate ground connection, red elements represent suspension springs in the test rig. **80**
Figure 4.18: Rotation of the shaft as defined in MSC Adams. **82**
Figure 5.1: Numerical acceleration spectra obtained from the models M1 (top), M2 (middle) and M3 (bottom) at steady-state conditions. **84**
Figure 5.2: Sidebands around 1X in the acceleration spectra obtained from the motor models M1, M2 and M3. .... **85**
Figure 5.3: Comparison of the numerical and the experimental steady-state acceleration spectra at 10000 RPM. Res. Reg. stands for resonance region. **86**
Figure 5.4: Numerical and experimental sidebands around the second harmonic of the shaft speed at 10000 RPM. **87**
Figure 5.5: Numerical and experimental sidebands around the second harmonic of the shaft speed at 10000 RPM. **88**
Figure 5.6: Comparison of the experimental (top) and the numerical (bottom) Campbell diagrams of the Atlas motor. Res. Reg. stands for resonance region. **90**
Figure 5.7: Ratio of numerical overall vibration to experimental overall vibration calculated between 6500 – 10000 RPM for two different frequency ranges. **91**
Figure 5.8: Predicted amplitudes of the ball pass frequency outer race (BPFO) obtained from the motor models with various levels of faults modelled in their bearing models. **92**
Figure 5.9: Amplitudes of the third and the fourth harmonics of the ball pass frequency outer race obtained from the healthy and the faulty models……………………………………………………………….**93**

MODELLING, ANALYSIS AND EXPERIMENTAL VALIDATION OF VIBRATION OF ELECTRIC MOTORS

SUMMARY

Electric motors are fundamental components of many machines and processes which provide mechanical power to the systems they are coupled to. Consequently, the performance and efficiency of these motors directly affect the performance and efficiency of the machines or processes they power. Therefore, it is always in engineers' best interest to improve the designs of electric motors in order to obtain higher efficiency, higher reliability as well as better performance from vibration and acoustics points of view.

In most design processes in industrial applications, numerical simulations are extensively utilised to minimise the number of design iterations and to reduce testing and prototyping costs. Finite element and multibody dynamic simulations are often used in these simulations and methodologies to build numerical models of electric motors which represent the real behaviour of these motors with acceptable accuracy are widely sought after in industry. The aim of this thesis is to develop a comprehensive methodology to build robust numerical models of electric motors and demonstrate the validity of the models using experimental data.

The Atlas motor, which is a small brushless DC motor manufactured by Arcelik A.S. to power Arcelik brand washing machines, is selected as a specimen to demonstrate the modelling and validation procedure proposed and used in this thesis. Firstly, the individual components of the Atlas motor are identified as the front and back covers, the stator, the bearings, the rotor and the flywheel. The flywheel is used here to simulate the loading the Atlas motor is subjected to during its operation in a washing machine. Then, each component is subjected to frequency response function measurements and their natural frequencies in the frequency range of interest (0 – 3200 Hz) are determined experimentally for model validation purposes. Finally, the Campbell Diagrams of the specimens are obtained using measured data between 1000 RPM – 10000 RPM range and this data is used later for the validation of the multibody dynamic models of the Atlas motor for the same frequency range of interest.

After the required tests and measurements are completed, finite element models are developed for individual components and their natural frequencies and corresponding mode shapes are calculated by means of modal analyses within the frequency range of interest. The results are compared with the test results and the models are then validated. The components which do not have elastic modes within the frequency range of interest are modelled as rigid bodies. Subsequently, flexible body models of the parts are created based on their finite element models. The generated flexible and rigid body models are then assembled using multibody dynamics simulation software, MSC Adams, by means of appropriate kinematic constraints between the parts. Although the rings and the balls of the ball bearing are modelled as rigid bodies, the nonlinear elastic contacts between the ball bearing elements (the rings and the rolling

elements) are included in the model using Hertzian contact approach. Both steady-state and Campbell Diagram simulations are conducted and the numerical results are compared with the experimental results for model validation purposes.

In this thesis, the complex contact mechanism between the front and back covers of the motor and the stator is simplified by assuming that these parts are perfectly joined (welded) together at the matching surfaces in the modelling stage. It is shown that this modelling approach yields results with less than 5 percent error in terms of natural frequencies of the assembly of the front cover, the back cover and the stator. Another important finding of this thesis is that, the use of primitive joints or bushings to model the ball bearings does not produce satisfactory results as the nonlinear behaviour of the ball bearings due to the contacts between their elements are neglected in this approach. It is further shown that the detailed bearing model developed in this thesis, which is based on the Hertzian contact theory, is able to produce results with satisfactory accuracy in terms of the nonlinear effects. Finally, it is discovered that the frequencies of the sidebands around the shaft rotation frequency and its harmonics are strongly affected by the contact angle and bearing clearance. A comparison between the results obtained from two different motor models, one with a bearing model that includes the effects of contact angle and bearing clearance and one that does not, revealed that the sidebands are predicted with less than 4 percent error in the former model. It is concluded that the proposed model can be used to predict not only the natural frequencies, but also the forced response characteristics of electric motors as a function of rotational speed with acceptable accuracy.

ELEKTRİK MOTORLARININ TİTREŞİMLERİNİN MODELLENMESİ, ANALİZİ VE DENEYSEL OLARAK DOĞRULANMASI

ÖZET

Elektrik motorları, günümüzde bir çok makineye ve işleme mekanik güç sağlayan önemli bileşenlerdir. Endüstriyel uygulamalarda elektrik motorlarının kullanıldığı alanlar, beyaz eşyaların sürülmesi, pompa, kompresör, fan gibi makinelere güç sağlanması, otomobillerde ve uçaklarda ana motorlara başlangıç enerjisinin sağlanması gibi uygulamalarda kullanılmakla beraber; günümüzde elektrik motorları, elektrikli otomobil ve uçakların geliştirilmeye başlamasıyla bu araçlarda ana motor olarak yer almak konusunda hızlıca ilerlemektedirler. Elektrik motorlarının burada bahsedildiği gibi bir çok farklı endüstriyel uygulamada kullanılıyor olması, uygulamaya özel elektrik motoru tasarımlarının geliştirilmesi ihtiyacını doğurmuş ve bunun sonucu olarak da bir çok farklı tipte elektrik motoru ortaya çıkmıştır. Elektrik motorlarının performansı ve verimliliği, bu motorların güç sağladıkları makine ve sistemlerin performans ve verimliliğini direkt olarak etkiler. Bu sebeple, elektrik motorlarının tasarımlarının iyileştirilmesi, motorun titreşim ve akustik olarak performansının artırılması maksadıyla mühendislerin önemli amaçlarındandır.

Elektrik motorlarının güç sağlamak için kullanıldığı sistem ve proseslerin verimlerinin artırılması maksadıyla elektrik motorlarının tasarımlarının iyileştirilmesinde iki ana yol mevcuttur. Bunlar, geleneksel yol ve modern yol olarak isimlendirilebilir. Geleneksel yolda, motor tasarımı güncellendikten sonra yeni tasarıma sahip bir prototip üretilir, sonrasında ise bu prototip, çeşitli test ve ölçüm senaryolarından geçirilerek, beklenen yükleme durumu altında yeni tasarıma sahip motorun performansı ve verimi incelenir. Protipin testlerde başarısız olması durumunda tasarım tekrar güncellenir ve testler tekrarlanır. Tekrarlanan bu prototipleme ve test uygulamaları pahalı ve çok zaman alan işlemlerdir. Modern yolda ise, tasarım iyileştirme iterasyonlarını ve ayrıca test ve prototip maliyetlerini azaltmak için sayısal modeller ve simülasyonlar etkin olarak kullanılmaktadır. Modern yolda, elektrik motorunun tasarımı güncellendikten sonra, yeni tasarıma ait bir prototip üretmek yerine, yeni tasarımın detaylarını ve bilgilerini içeren bilgisayar simülasyonu modelleri kurulur. Sonrasında ise prototip üzerinde test ve ölçüm yapmak yerine, yapılacak testler, bahsedilen bu bilgisayar modeli üzerinde, bilgisayar simülasyonu ortamında gerçekleştirilir ve elde edilen simülasyon sonuçları incelenir. Sonuçların başarısız olması durumunda elektrik motoru tasarımı güncellenir ve tekrar prototipleme yerine, önceki bilgisayar simülasyon modelindeki tasarım güncellenerek, test simülasyonları bu güncellenmiş model üzerinde tekrarlanır. Böylece, zaman alan ve pahalı olan prototip ve test iterasyonları azaltılmış olur. Dolayısıyla, elektrik motorlarının gerçek davranışlarını tatmin edici bir isabetle modelleyebilen sonlu eleman simülasyonu ve çoklu cisim dinamiği simülasyonu yöntemlerine endüstride sıklıkla ihtiyaç duyulmaktadır. Bu tezin amacı, elektrik motorlarının sayısal olarak

modellenmesi üzerine derinlemesine bir yöntemin geliştirilmesi ve ortaya çıkan modelin doğruluğunun deneysel verilerle kıyaslanarak gösterilmesidir.

Tezde geliştirilen modelleme yöntemleri ve deneysel doğrulama işlemleri için numune olarak, Arçelik A.Ş. tarafından üretilmekte olan bir fırçasız DC motor olan Atlas motor seçilmiştir. İlk olarak, Atlas motorun bileşenleri, ön kapak, arka kapak, stator, rulmanlar, rotor ve volan olarak ayrı ayrı belirlenmiştir. Elektrik motorunun çamaşır makinası içinde çalışması sırasında maruz kaldığı tambur yükünü temsil etmesi amacıyla volan kullanılmıştır. Daha sonra, belirlenen bu bileşenler ayrı ayrı frekans cevap fonksiyonu ölçümünden geçirilerek, daha sonra model doğrulama işlemlerinde kullanılmak üzere bu bileşenlerin 0 – 3200 Hz aralığındaki doğal frekansları belirlenmiştir. Son olarak, 1000 – 10000 RPM aralığında numunelerin Campbell diyagramları ölçülmüş ve elde edilen deneysel veriler daha sonra Atlas motorun çoklu cisim dinamiği modelinin doğrulanması için kullanılmıştır.

Gerekli test ve ölçümlerin tamamlanmasından sonra, Atlas motorun daha önce bahsedilen bileşenleri için ayrı ayrı sonlu eleman modelleri oluşturulmuş ve bileşenler üzerinde sayısal modal analizler gerçekleştirilerek, ilgilenilen frekans aralığında bu bileşenlerin doğal frekansları ve mod şekilleri hesaplanmış; sonrasında ise deneysel veriler ile doğrulanmıştır. İlgilenilen frekans aralığında doğal frekansı bulunmayan bileşenler rijit olarak modellenmiştir. İlgilenilen frekans aralığında doğal frekansı bulunan bileşenler içinse esnek cisim modelleri oluşturulmuştur. Oluşturulan esnek cisim ve rijit cisim modelleri, MSC Adams programı içerisinde uygun kinematik ilişkiler kullanılarak birleştirilmiş ve Atlas motorun çoklu cisim dinamiği modeli oluşturulmuştur. Rulman bileşenlerinden olan iç ve dış bilezik ve bilyaların rijit olarak modellenmesine ragmen, bu bileşenler arasında gerçekleşen doğrusal olmayan elastic temasları modellemek için Hertz temas teorisine dayanan bir temas modeli kullanılmıştır. Hem dinamik denge hali, hem de Campbell diyagramı simülasyonları gerçekleştirilmiş ve elde edilen sayısal sonuçlar, deneysel sonuçlarla kıyaslanarak doğrulanmıştır.

Ön ve arka kapaklar ile stator arasındaki karmaşık temas durumu, bu bileşenlerin temas eden yüzeylerinden mükemmel olarak birleştirildiği (veya kaynaklandığı) varsayılarak basitleştirilerek modellenmiştir. Sonuçlarda, bu basitleştirilmiş yaklaşımın modellemede kullanılmasıyla, ön ve arka kapaklarla birlikte statordan oluşan montaj grubunun doğal frekanslarının yüzde beşten daha düşük bir hatayla ifade edilebildiği gösterilmiştir. Bu tez çalışmasında elde edilen önemli bir diğer bulgu ise, motordaki rulmanları modellemek üzere basit mafsalların veya bushing adı verilen doğrusal elastik elemanların kullanılmasının, bahsedilen bu elemanların, rulman bileşenleri arasındaki temaslardan dolayı meydana gelen doğrusal olmayan (nonlinear) etkileri ihmal etmesi sebebiyle motorun titreşimi ve dinamiği hakkında yeterli doğrulukta sonuçlar üretemeyeceği olmuştur. Ayrıca, rulman bileşenleri arasındaki temasları, Hertz temas teorisi üzerine kurulu bir temas modeliyle ifade eden detaylı bir rulman modelinin bahsedilen bu doğrusal olmayan etkileri ifade etmekte tatmin edici sonuçlar ürettiği gösterilmiştir. Son olarak, şaft dönme frekansının ve harmoniklerinin çevresinde görülen yan bantların frekanslarının, rulmanda meydana gelen temas açısı ve rulman boşluğundan kuvvetli bir şekilde etkilendiği görülmüştür. Birinde temas açısı ve rulman boşluğu etkilerini içeren bir rulman modeli bulunan, diğerinde ise bu etkileri ihmal eden bir rulman modeli bulunan iki farklı motor modelinden alınan sayısal sonuçlar karşılaştırılmış ve ilk modelden alınan verilerin, yan bantları yüzde dörtten daha düşük bir hata ile tahmin edebildiği gösterilmiştir.

Sonuç olarak, bu tezde ortaya konulan motor modelinin, sadece motor doğal frekanslarını değil, ayrıca elektrik motorunun zorlanmış titreşim karakteristiklerini de şaft dönme hızının bir fonksiyonu olarak tatmin edici bir isabetle tahmin edebildiği gösterilmiştir. Bunun yanında, yine bu tez çalışmasında, elektrik motorlarının bahsedilen doğal frekans ve zorlanmış titreşimlerinin karakteristiklerini sadece tek bir şaft dönme hızında değil, şaft dönme hızının çeşitli değerler aldığı geniş bir aralıkta, bu aralıktaki tüm şaft dönme hızı değerleri için tatmin edici bir isabetle tahmin edebildiği, deneysel verilerle birebir kıyaslama yapılarak gösterilmiştir.

1. INTRODUCTION

1.1 Definition of the Problem

A wide variety of machines are used in industry such as compressors, pumps, turbines and many more. Electric motors are responsible for providing power to many of these machines; thus, they are indispensable components in today's industry. An electric motor can be considered as the heart of the machine it powers. Therefore, the operational characteristics of an electric motor directly affect the performance of the machine it drives.

In industrial applications, there are mainly two situations where a numerical model of an electric motor would be needed. One of the situations is that, a numerical model of an electric motor is needed for design purposes. Due to the fact that mechanical, acoustic and electrical characteristics of electric motors directly affect the performances of the machines, appropriate mechanical, acoustic and electrical designs of electric motors must be carried out by the manufacturers of electric motors. Having numerical models of electric motors during early design phases greatly reduces prototyping costs. The second situation is when a system comprising an electric motor is to be designed an optimised. For instance, white appliance manufacturers often develop numerical models for their products for the purpose of research or product development. In these models, electric motors belong to the non-design space and only serve as excitation and vibration/noise sources in the system (e.g., in washing machines). In order to achieve the desired accuracy of the numerical models for such systems, it is also crucial to develop numerical models of electric motors with acceptable accuracy. Although accuracy is important, in most cases, higher accuracy means higher cost of modelling. Industrial design problems have time constraints too. Therefore, the computational time requirements for numerical models of electric motors must be reasonable too.

Taking into account the points made above, it is of critical importance to develop numerical models of electric motors which are sufficiently accurate while still being fast enough to meet industry's demands.

1.2 Literature Survey

Though this thesis discusses numerical modelling of a small, brushless DC motor, literature survey is conducted by taking into account two major issues in numerical models of electric motors; namely, numerical modelling of electromagnetic forces in electric motors and multibody dynamic (MBD) modelling of ball bearings.

Current literature includes a number of studies on modelling of electromagnetic forces and torques in electric motors [1]. Low et al. [2] present a hybrid model consisting of numerical and analytical approaches in order to model the electromagnetic forces and torques in electric machines. It is shown that, using a purely numerical approach leads to increased numerical error, especially at the interior parts of the airgap. Therefore, a hybrid model which uses an analytical approach for the interior parts of the airgap and a numerical approach for the rest of the structure is proposed. Figure 1.1 depicts the finite element (FE) mesh used in [2].

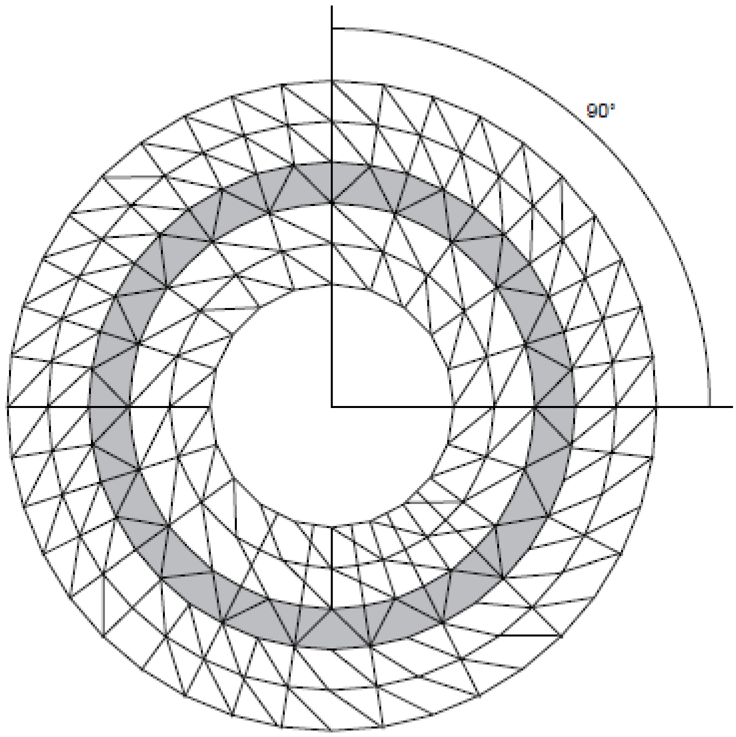

Figure 1.1 : Finite element mesh used for the numerical approach in [2].

Ishibashi et al. [3] present a study on numerical simulations of electromagnetic vibrations of small induction motors. Both numerical and experimental results are provided in order to validate the numerical results. It is shown that vibration amplitudes and modes are numerically calculated with acceptable accuracy by the study of fluxes, Maxwell forces and mechanical deformations. Figure 1.2 shows the FE model used in [3].

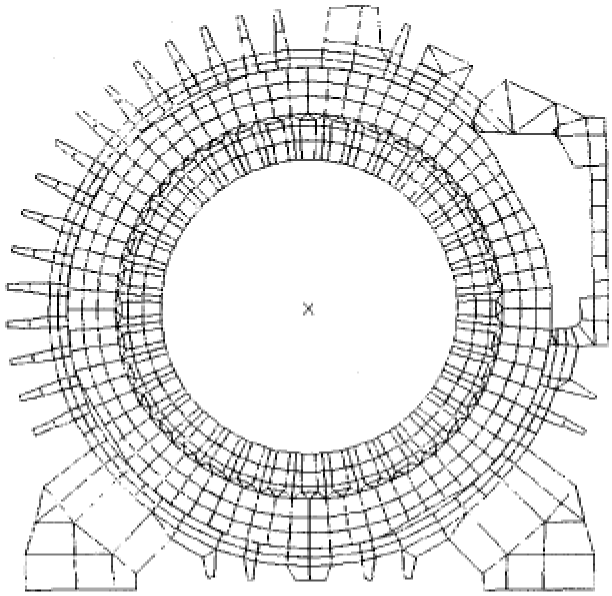

Figure 1.2 : Finite Element (FE) model developed in [3] to calculate vibration amplitudes.

Furlan et al. [4] propose a coupled numerical model to predict the acoustic field of a DC motor. In this study, geometric attributes and material properties of the DC motor in a finite element model are used to build an electromagnetic model of the motor. The results for vibration of the motor are presented in the form of velocity values on the outer surface of the motor. It is noted in [4] that, though finite element method (FEM) was used to model the electromagnetic forces, it would be more convenient to use boundary element method (BEM) since only the outer surface of the motor is discretised for numerical calculations. Figure 1.3 shows the FE models of rotors used in [4].

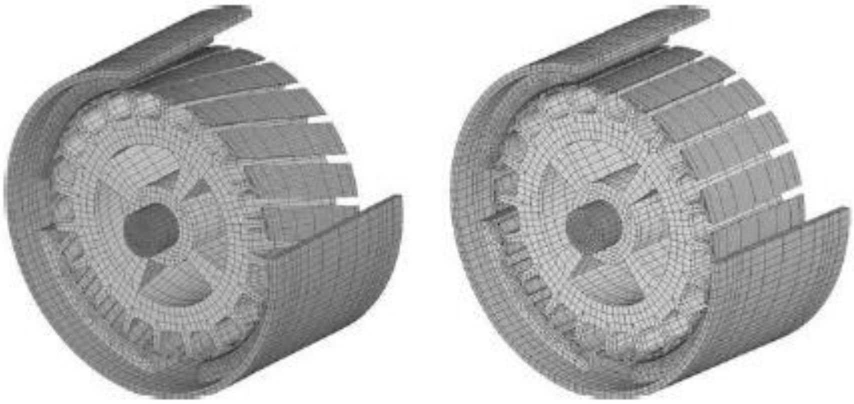

Figure 1.3 : The FE models of rotors used in [4].

Neves et al. [5] present a study, which is a combination of numerical and experimental processes, on identification of magnetic-based vibration sources in induction motors. Firstly, a 2D electromagnetic FEM analysis is conducted on the motor to evaluate the electromagnetic forces. Subsequently, the spectrum of these forces is generated. Thirdly, a series of modal tests are conducted in order to find the motor's modal parameters. Finally, accelerations of the motor are measured. It is shown in [5] that there is a strong relation between the modal parameters of the motor and the electromagnetic forces. Figure 1.4 shows the numerical procedure used to calculate electromagnetic forces in [5].

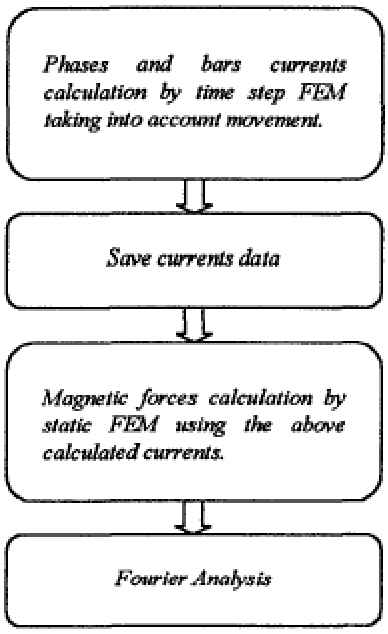

Figure 1.4 : The numerical procedure followed in [5] to calculate electromagnetic forces in the motor.

Giet et al. [6] conduct a comparative study which highlights the differences between 2D and 3D methods for coupled electromagnetic and structure-dynamic modelling of electrical machines. It is pointed out that 2D models demand less computational effort at the expense of accuracy in the results. It is further shown that the results of the 2D models can exhibit an acceptable level of correlation with those of 3D models if the axial effects are not strong.

Samoto et al. [7] propose a numerical procedure which can be used to calculate the vibrations of an electric machine due to higher harmonics of electromagnetic forces. A 2D magnetic field analysis and a 3D vibration analysis are used in conjunction to model the electric machine's dynamics. It is stated that a 2D approach for the calculation of the magnetic field will result in satisfactory accuracy as there are no major axial effects in terms of electromagnetic field distribution. However, it is also stated that a 3D numerical approach needs to be taken to model the structural dynamic behaviour due to the varying mass and stiffness distribution along the axial direction. Subsequently, the vibration responses are calculated in the form of radial accelerations to specific harmonics of the electromagnetic forces and these numerical results are validated with experimental results. Finally, it is shown that numerical and the experimental results are in good agreement. Figure 1.5 shows the numerically and experimentally obtained results in [7].

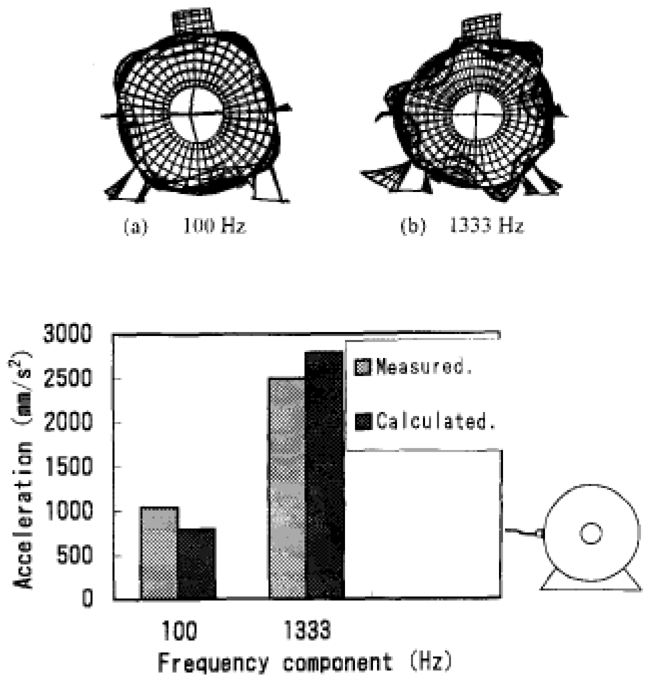

Figure 1.5 : Numerical model used and the comparison of numerical and experimental results in [7].

Mohammed et al. [8] computationally show that magnetostriction, defined as a behaviour of ferrous alloys which causes them to show straining in a magnetic field, is a significant reason for noise in electrical machines. Numerical results of Mohammed’s previously-developed transient model, given in [9], are presented to show that the electromagnetic forces due to magnetostriction are potent and should be taken into account for the electrical machine’s design.

Hwang et al. [10] present numerical results of variation of air-gap flux, obtained from a finite element model, in an electric motor due to rotor eccentricity. They also present experimental results for model validation. Firstly, vibration data are acquired from both finite element model and the test unit, which are then converted to air-gap data by correlating the changes in vibration with the changes in air-gap length.

Kobayashi et al. [11] demonstrate a numerical procedure to examine the influence of slot combination on an induction motor’s noise. On the computational side, a combination of a transient FEM approach and harmonic analysis by Fourier series expansion is used in order to calculate the electromagnetic forces in the machine. To verify the computational results, acoustic measurements are taken from the machine, which are later compared with the numerical results. Finally, it is shown that the calculated and measured vibration modes have good correlation.

Li et al. [12] present a numerical study validated by experiments to investigate and solve the squeaking noise of a permanent-magnet DC brush motor. A finite element approach is used to represent the radial forces based on Maxwell Stress Tensor Method. As a result of the numerical analysis of magnetic field, it is discovered that the examined motor has asymmetrical magnetic field distribution in the air-gap. It is verified by experiments that a motor design which leads to lower amount of unbalanced radial electromagnetic forces results in considerably less squeaking noise. Figure 1.6 depicts the numerically-calculated field distributions in [12].

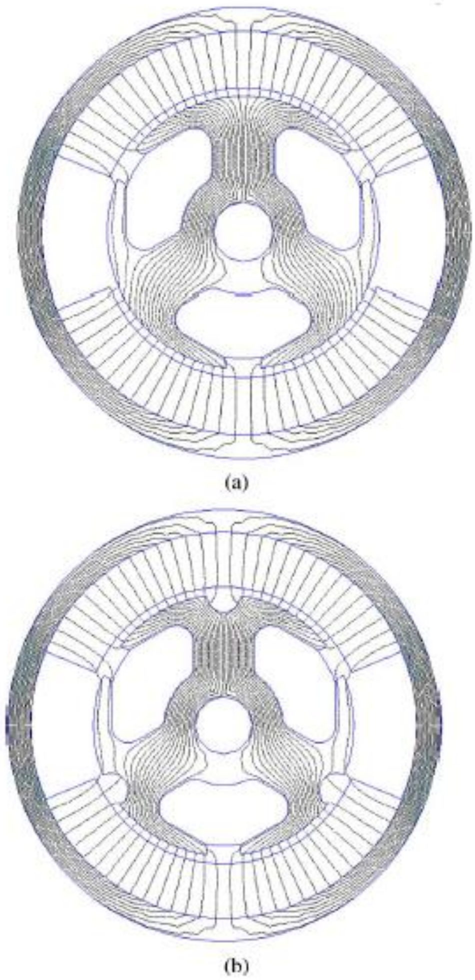

Figure 1.6 : Numerically-calculated field distribution in [12]. a) Traditional motor geometry. b) Proposed motor design with lower squeaking noise in the motor.

As stated before, literature survey on modelling ball bearings is also carried out in this thesis. Li-xin et al. [13] develop a dynamic model for multibody systems with deep-groove ball bearings. The contact relation between the rolling elements and the raceways are modelled using the Hertzian contact theory which allows for the calculation of normal contact forces on each rolling element. It is stated that these individual forces can be used for bearing life prediction and estimating bearing strength. Figure 1.7 shows a graphical representation of the elastic ball bearing model developed in [13].

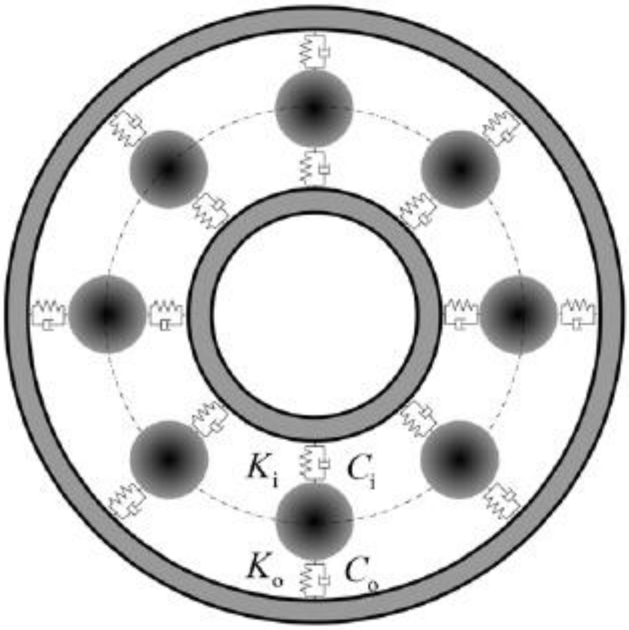

Figure 1.7 : The elastic ball bearing model developed in [13].

Yao et al. [14] propose a multibody system dynamics (MBS) model with the aim of bringing up a new 3D approach in order to represent the flexibility of bearing rings in a multibody model. The flexibility of the rings is represented by means of discrete equivalent rigid elements connected with curved Timoshenko beam elements. For comparison, a FEM and an analytical model of the rings are also presented. Comparisons between these models are made using the results of vibration response and static deformations of the rings. It is shown that the results produced by the proposed MBS model correlate well with the results from the FEM and the analytical model.

Yu et al. [15] offer a mathematical model with 4 degrees of freedom (DOFs) to model the dynamics of a deep-groove ball bearing. These 4 DOFs represent the horizontal and vertical DOFs of the inner and outer rings. The axial clearance of the ball bearing and lubrication effects are ignored in this study. The individual rolling elements are represented as pairs of spring and damper. Equations of motion of the 4 DOF model are derived and solved numerically using the fourth order Runge-Kutta Method in order to calculate displacements, velocities and accelerations. Responses of the bearing under different loads and running speeds are investigated using the model and the differences between responses taken from models running under different conditions are laid out. Finally, the numerical results are verified by experimental results. Figure 1.8 shows the 4-DOF model developed in [15].

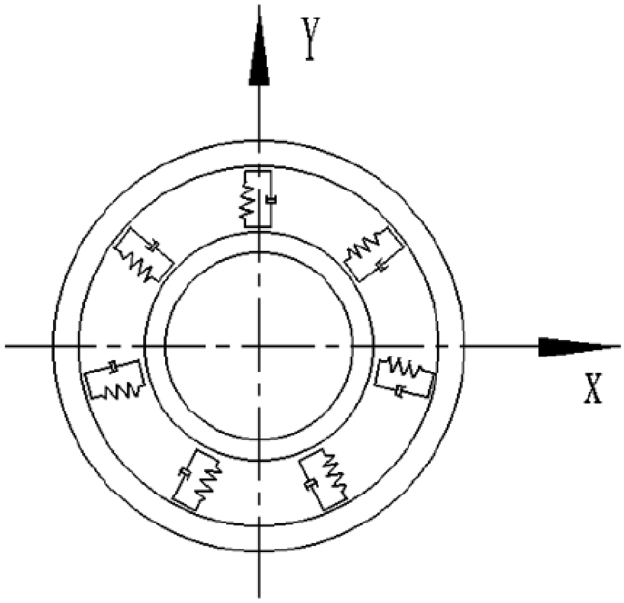

Figure 1.8 : The 4-DOF model developed in [15].

Yao et al. [16] propose a new multibody dynamic analysis procedure for mechanisms comprising deep-groove ball bearings with radial clearances and impacts between its elements. Contacts between the rolling elements and the rings as well as the rolling elements and the cage are taken into account in the model, based on the Hertzian contact theory. The elasticity of the rings, the cage and the rolling elements are not considered in the model. In order to reduce computational complexity, elastohydrodynamic (EHD) lubrication effects are also ignored. Only the Hertzian contact relationships and Coulomb friction between the contacting parts are considered. It is further assumed that the outer ring is rigidly fitted to the bearing housing and the inner ring is rigidly attached to the journal. It is stated that, joint forces are much larger in real deep-groove ball bearing joints than ideal joints due to the dynamics of ball bearings and clearances in the bearing. Finally, it is shown that the performance and the accuracy of motion of the mechanism are affected by the dynamics of the ball bearings the mechanism comprises.

Sopanen and Mikkola [17] present a 6-DOF dynamic model for a deep-groove ball bearing, which takes into account the effects of bearing defects. The contacts between the bearing components are modelled using non-linear Hertzian contact theory. Elastohydrodynamic effect of the lubricant film is also included in the model. The inputs to the model are the bearing geometry, material properties of the bearing components and bearing clearance. The proposed model is designed to simulate the effects of both distributed faults such as raceway waviness and localised faults such as a dent on one of the raceways. Some simplifications are made in the model in order to reduce computational costs. The centrifugal forces on the rolling elements are ignored and the distance between the balls are assumed to remain constant for the duration of the analysis. Also, the bending of the rings is ignored and it is assumed that there is no slipping or sliding between the bearing components. The continuation of [17], by the same authors, is given in [18] where the bearing model developed in [17] is applied in a multibody dynamic model of an electric motor to represent the bearings carrying the motor's shaft. It is shown that bearing clearance has a strong influence on the natural frequencies and the vibration of the motor. It is further shown that localised defects create vibrations at their respective bearing frequency. The numerical results obtained by the model are validated with analytical and experimental results by comparing the vibration spectra obtained by the model and reported experiments in the literature.

Çakmak and Şanlıtürk [19] propose a detailed numerical model of a deep-groove ball bearing and apply the bearing model in an overhung rotor model. The model is implemented using a well-known commercial multibody dynamics simulation software, MSC Adams. To increase the computational efficiency, the elasticity of the rings is neglected. In addition, the cage structure is represented as a series of massless rigid links between consecutive rolling elements. Furthermore, it is assumed that the components of the bearing remain planar for the duration of the analysis and the contact forces between the bodies are transferred only through the circular curves defined on the contacting elements to represent the raceways and the circumference of the rolling elements. The contacts between the rolling elements and the rings are modelled using the Hertzian contact theory. Both flexible and rigid models for the rotor are created for comparisons of the system's response. Campbell diagrams are numerically calculated using the model and experimentally measured using a test rig in order to validate the numerical model. It is shown that the bending and torsion modes of the system are predicted with acceptable correlation with the test results. Additionally, it is demonstrated by Campbell diagrams that, to better represent the unbalanced dynamic system's characteristics, the shaft must be modelled as flexible rather than rigid. It is further shown that, when a localised defect is included on the outer ring of the bearing model, the model accurately represents the faulty bearing's dynamics by means of increased vibration amplitudes at the corresponding bearing frequency, which is also validated by tests. The ball bearing model and the bearing-shaft-rotor model developed in [19] are shown in Figure 1.9.

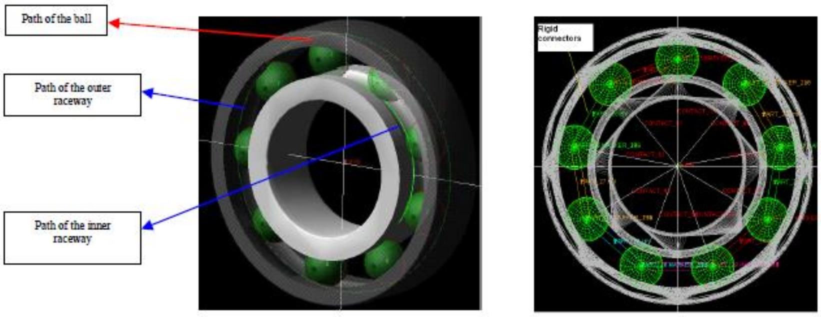

(a)

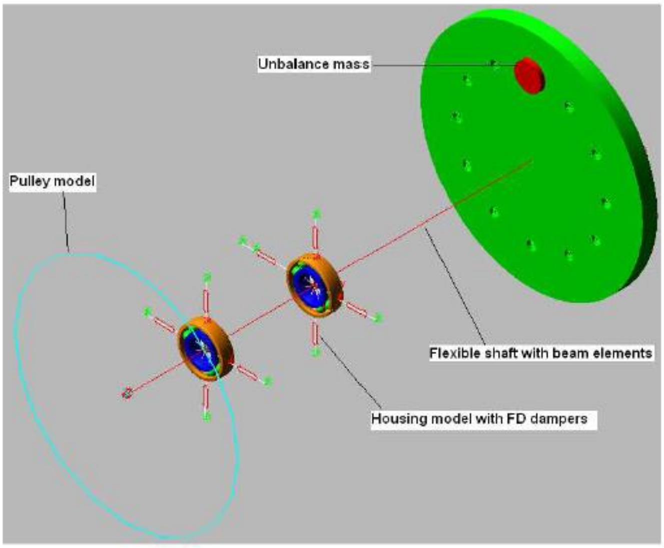

(b)

Figure 1.9 : The numerical models of **a)** the deep-groove ball bearing and **b)** the bearing-shaft-rotor system developed in [19].

Wagner et al. [20] present a transient ball bearing model that includes the elasticity of the outer ring for high-speed applications. Unlike many other models, the model in [20] considers the centrifugal forces and spinning of the rolling elements to meet the aim of developing a model to accurately represent high-speed conditions. Also, gyroscopic effects are considered in the model. The outer ring's elasticity is taken into account in the model. For comparison, another model with a rigid outer ring is used to investigate the effects of outer ring's elasticity on the model's accuracy. To simplify the model, the radii of the inner and outer ring's raceways are assumed to be constant. Further simplifications in the model include neglecting the cage's inertia, bearing clearance and the effects of lubrication and simplification of the flexible outer ring geometry. It is shown that the high-speed dynamic characteristics of the ball bearing model are significantly affected when the flexibility of the outer ring is included in a high-speed model. The flexible outer ring model used in [20] is shown in Figure 1.10.

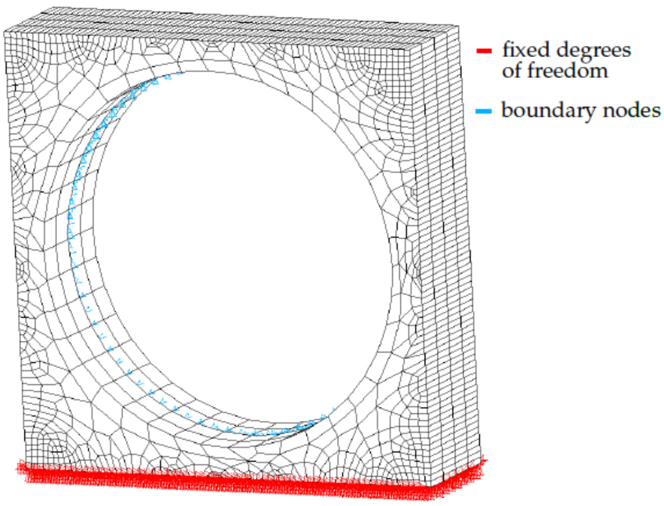

Figure 1.10 : The simplified flexible numerical model for the outer ring of the ball bearing model presented in [20].

1.3 Objectives and Scope of the Thesis

This thesis primarily aims to create a sufficiently accurate multibody dynamic model for the brushless DC motor, Atlas which is designed, developed and manufactured by Arcelik A.S., to be used in Arcelik's and its sub-brands' washing machines. This motor model is aimed to be used as a model for the purposes of updating/optimising the current motor design as well as a sub-model in multibody dynamic models of washing machines designed and manufactured by Arcelik. Therefore, complementing the primary aim of this thesis, natural frequencies and the corresponding modes shapes as well as the forced vibrations of the Atlas electric motor are aimed to be predicted accurately with the model developed in this thesis.

The secondary aim of the thesis is to keep the computation time of the presented model within acceptable limits with respect to typical time constraints in industry.

The work carried out in this thesis are organised as follows. The first chapter makes an introduction to the problem and presents a literature survey on the problem.

The second chapter summarises the theory used in the development of the electric motor model. The theory used here includes Hertzian Contact Theory, rotor dynamics, dynamics of ball bearings, electromagnetism and electromagnetic forces generated in an electric motor.

The third chapter describes the test procedures for model validation, introduces the designed test rig to obtain vibration measurements and Campbell diagrams of both loaded and unloaded electric motors, also presents necessary test and measurement results.

The fourth chapter discusses how the numerical models are created for the individual parts of the electric motor and subsequently, the assembled motor. The simplifications made in the motor's geometry, element type selection for the parts which are modelled as flexible, also the reasoning behind modelling some parts as rigid are discussed. Development of the bearing model is discussed in detail. Finally, the modelling of the electromagnetic excitation forces in the motor is discussed.

The fifth chapter is dedicated to validation of the numerical model with experimental results. Firstly, the numerical models of the individual parts of the motor are validated using the measured FRFs. Secondly, the numerical models of the individual parts are assembled and the model of the assembled motor is validated using the measured FRFs again under non-rotating conditions. Subsequently, the dynamic model for the assembled motor is generated and Campbell diagrams are calculated numerically. This is followed by comparisons of acceleration data are compared with the test results in order to validate the dynamic model. The parameters which can be used to update the dynamic model are identified and the details of model updating procedure are discussed.

The sixth chapter summarises the main findings and conclusions of this thesis including suggestions for ways of further improving the presented electric motor model.

2. THEORY

2.1 Electromagnetics

2.1.1 Electric field and electric force

Electric field is meaningful only for charged particles. It is defined as the surrounding vector field of a charged particle in which repulsive or attractive forces are created on other charged particles depending on the polarity of their charge. Electric fields are visualised as electric field lines going outward from positive charge into negative charge, as show below in Figure 2.1.

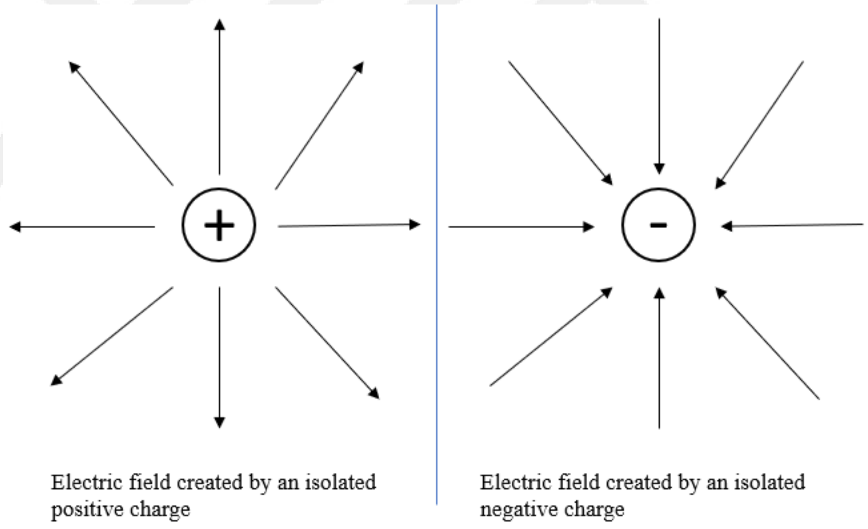

Figure 2.1 : Electric field lines of positive and negative charges.

The magnitude of the electric field of a charged particle at a given distance from the particle is calculated as:

$$E = \frac{kq}{r^2} \tag{2.1}$$

In equation 2.1, q is the charge of the particle, r is the distance from the particle and k is a constant which is equal to $8.99\ x\ 10^9 N\ m^2/C^2$.

Electric force is a force vector which is in the same direction as the electric field vector. Electric force vector of a charged particle in an electric field is calculated as below:

$$\overrightarrow{F_E} = q\vec{E} \tag{2.2}$$

where $\overrightarrow{F_E}$ denotes the electric force vector and $\vec{E}$ denotes the electric field vector. Additionally, an electric force is generated on a charged particle by another charged particle which is at a distance r from the first particle. The generated electric force is calculated by Coulomb's Law as below:

$$F_E = \frac{k * q_1 * q_2}{r^2} \tag{2.3}$$

where k is a constant, q_1 is the charge of the first particle and q_2 is the charge of the second particle [21].

2.1.2 Magnetic field and magnetic force

Magnetic fields are created by magnets, electric current or alternating electric field. Around a magnet, the magnetic field can be thought of as a series of lines going out from the north pole into the south pole of a magnet. A visualisation of a magnetic field lines is given in Figure 2.2.

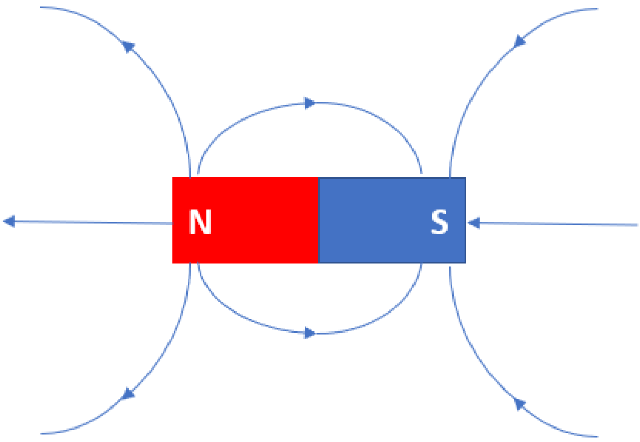

Figure 2.2 : Magnetic field lines sprouting from the north pole of the magnet and going into the south pole.

Magnetic field lines never intersect. Therefore, when same poles of two magnets are put next to one another, instead of crossing each other, magnetic field lines induce a repelling behaviour between the magnets which result in a segregated field line distribution between the magnets as shown in Figure 2.3.

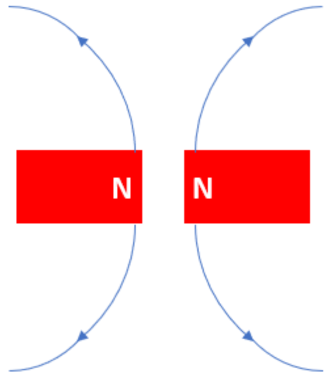

Figure 2.3 : Segregated magnetic field lines of the same poles of two magnets put next to one another.

Electric current flow also creates a magnetic field. When electric current flow in a wire is considered, the magnetic field created will be in the plane which is perpendicular to the current's direction of flow. In such case, the magnetic field lines have a circular direction around the current flow as shown in Figure 2.4.

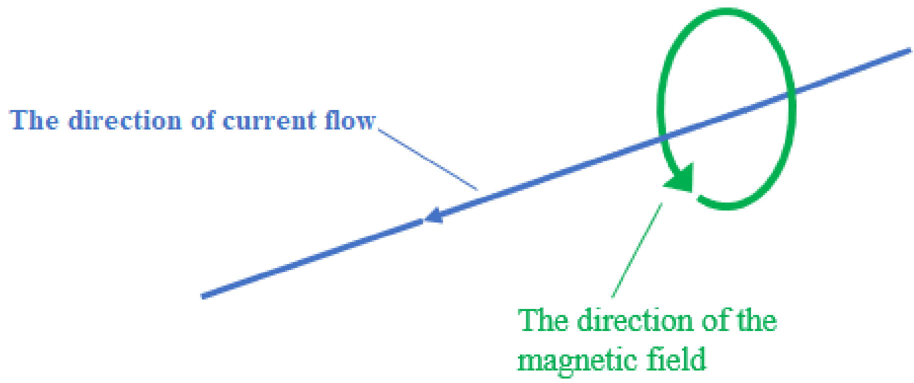

Figure 2.4 : Direction of magnetic field created by current flow.

The magnitude of the magnetic field created by current flow is calculated using Ampere's Law as given below, where the resulting unit is tesla [21].

$$B = \frac{\mu_0 I}{2\pi r} \tag{2.4}$$

In equation 2.4, μ_0 denotes the permeability of free space, I denotes the magnitude of the current and r denotes the distance from the wire to the point where the magnitude of the magnetic field is to be calculated.

Finally, an alternating electric field creates a magnetic field. Figure 2.5 shows how magnetic field changes with changing electric field.

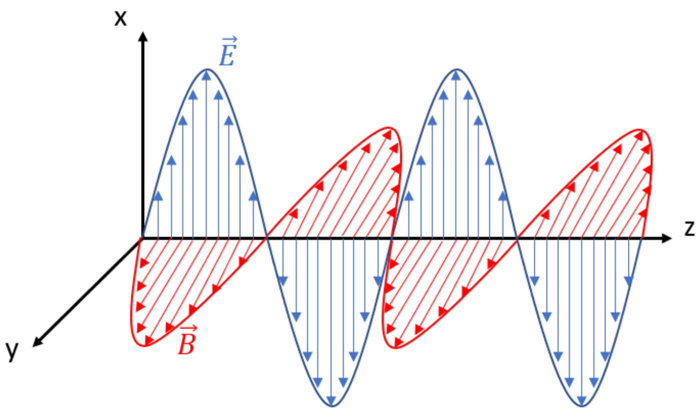

Figure 2.5 : Magnetic field (red) created by the changing electric field (blue).

When a charged particle moves in a magnetic field, a magnetic force is exerted on the particle by the magnetic field. The magnetic force exerted on the charged particle is calculated, in a vector form, by Lorentz Force Lawas given below:

$$\overrightarrow{F_B} = q\vec{v} \, x \, \vec{B} \tag{2.5}$$

where q is the charge of the particle, $\vec{v}$ is the particle's velocity vector, $\vec{B}$ is the magnetic field vector and $\overrightarrow{F_B}$ is the magnetic force applied on the moving particle [22].

2.1.3 Electromagnetic field and electromagnetic force

Electromagnetic field is the combination of an electric field and a magnetic field, which can be visualised as previously depicted in Figure 2.5 where the electric and magnetic fields are displayed together. The same analogy applies to the definition of electromagnetic force which is the sum of the electric force and the magnetic force, as defined by the Lorenz Force Law. Similar to equation 2.5, the electromagnetic force exerted on a charged particle moving in an electromagnetic field is calculated as

$$\overrightarrow{F_{EB}} = q\vec{E} + q\vec{v} \, x \, \vec{B} \tag{2.6}$$

The electromagnetic force acting on a charged particle which is subjected to an electric field E and a magnetic field B can be visualised as shown below.

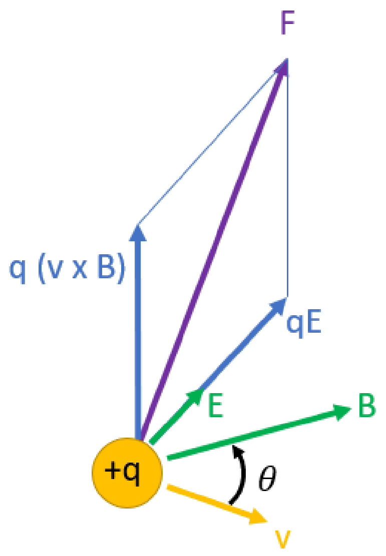

Figure 2.6 : Electromagnetic force, F, on a charged particle.

2.1.4 Electromagnetic induction: Faraday's Law and Lenz's Law

An important subject in electromagnetism is electromagnetic induction, which is explained by Faraday's Law and Lenz's Law. Essentially, Faraday's Law states that, when a conductor is subjected to a changing magnetic field, a current is induced on the conductor. Flow of the induced current indicates a potential difference, or a voltage which is called electromotive force (EMF), induced on the conductor. A possible experimental scenario to observe electromagnetic induction and Faraday's Law is depicted below in Figure 2.7. As seen, under constant magnetic field through the conducting loop, the galvanometer measures no current. However, when an increasing magnetic field is passed through the conducting loop, a current is induced in the wire, which is measured by the galvanometer.

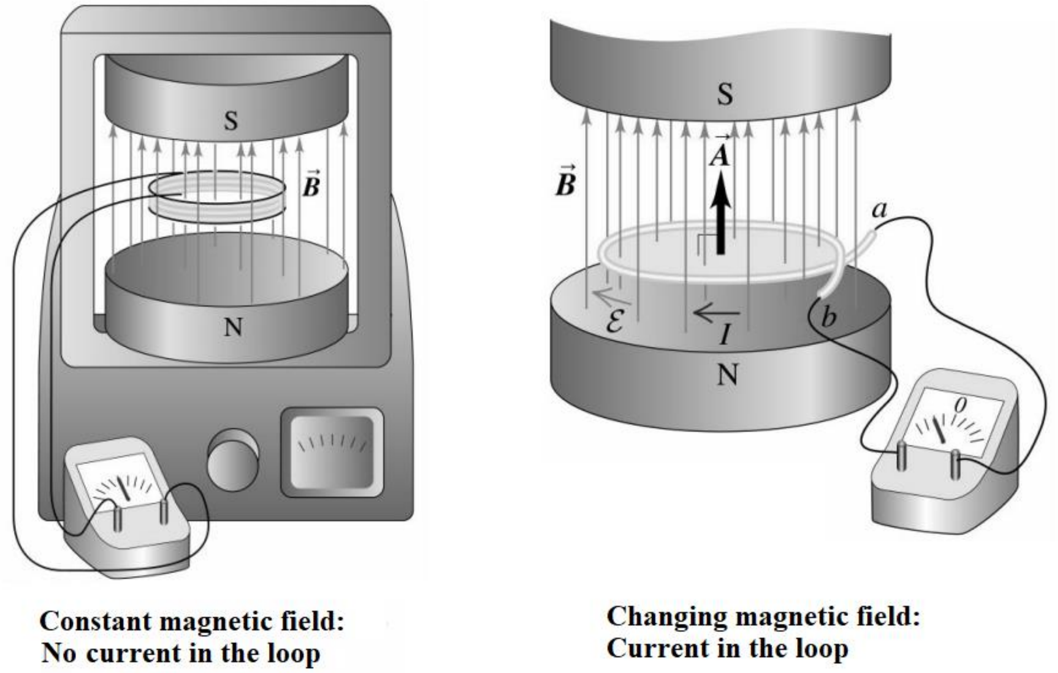

Figure 2.7 : Experimental setup to observe electromagnetic induction.

The direction of the magnetic field created by the induced current, and thus, the direction of the induced current, is precisely explained by Lenz's Law. Lenz's Law states that, the magnetic field which will be created by the induced current, will be in the opposite direction of the change in the magnetic field by which the current is induced. Figure 2.8 graphically shows how the directions of the induced magnetic field and current are determined. As seen in Figure 2.8, the magnetic field through the loop is increasing in the upward direction. This change in the magnetic field induces another magnetic field through the loop, which is in the opposite direction of the change, namely, the downward direction. Furthermore, it is found that the induced current's direction follows the circumference of the loop to satisfy the direction of the induced magnetic field.

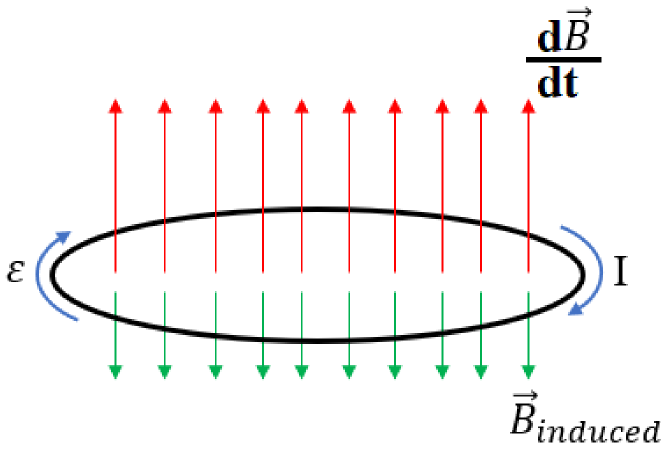

Figure 2.8 : A magnetic field and current are induced as a result of increasing magnetic field through the loop.

2.2 Structure and Dynamics of Ball Bearings

2.2.1 General structure of deep-groove ball bearings

A typical deep-groove ball bearing consists of 4 major components whose properties determine the bearing's dynamic behaviour. These major components are the inner and outer rings, the cage and the balls. Figure 2.9 shows these major components in assembly form in a typical deep-groove ball bearing.

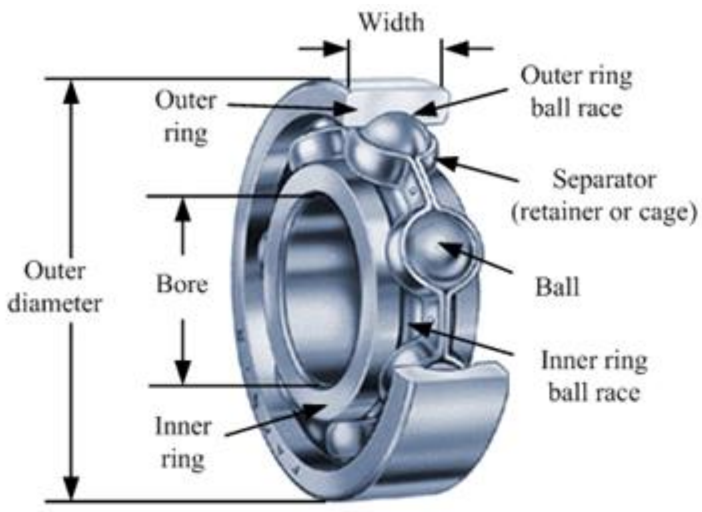

Figure 2.9 : Components of a deep-groove ball bearing [23].

Depending on application, either the inner or the outer ring can be fixed in a housing while the other can freely rotate. In most applications, the outer ring is placed in a housing and set fixed, and a shaft is fit in the inner ring to freely rotate with the inner ring.

Certain geometric features of the ball bearing are important to define its dynamic properties. These geometric features include the ball diameter (d), the number of balls (N), the pitch diameter (d_m), the inner raceway radius (R_{in}), the outer raceway radius (R_{out}), the inner groove radius (R_i), the outer groove radius (R_o) and the contact angle (α). Figure 2.10 shows these features graphically.

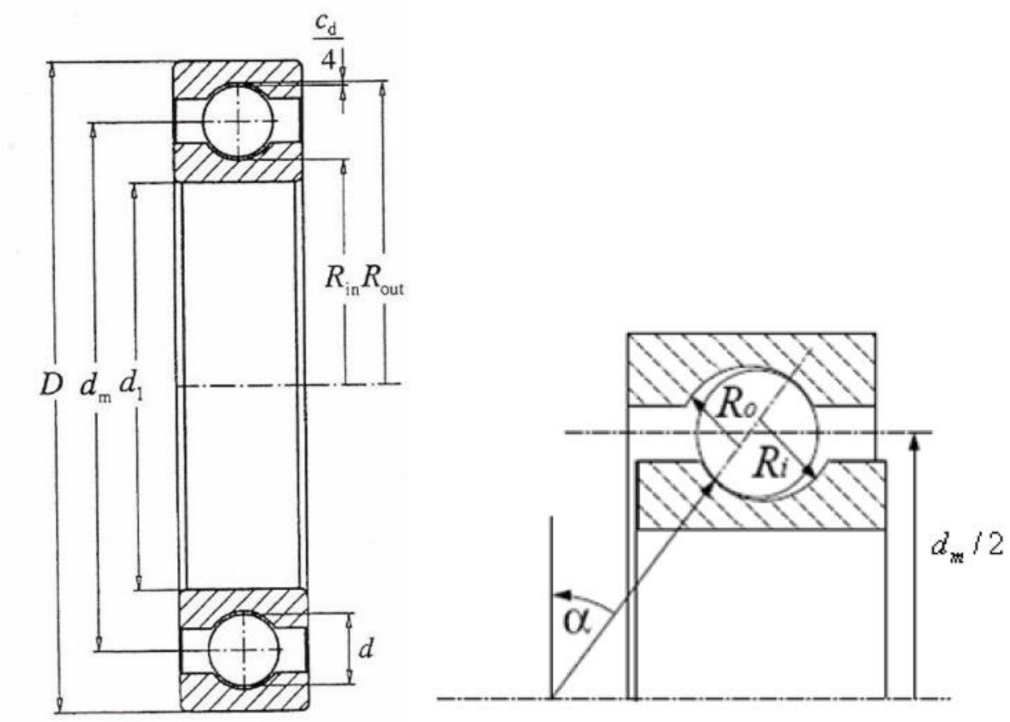

Figure 2.10 : Important geometric features of ball bearing [24, 25].

2.2.2 Load carrying characteristics of ball bearings

2.2.2.1 Load zone

An important phenomenon in ball bearing dynamics is the so-called load zone. Load zone is defined as the circumferential region in a ball bearing where the rolling elements actively carry load and nowhere else. In other words, only the balls within the load zone carry load, and thus, are subjected to deflection; while the balls which are not within the load zone do not carry any load, and thus, are not subjected to any deflection. A graphical representation of the load zone is given in Figure 2.11.

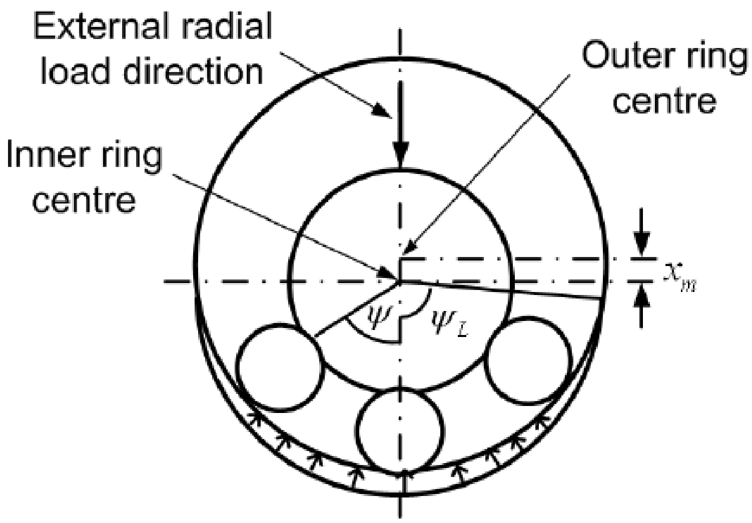

Figure 2.11 : Load zone of a ball bearing [23].

Load zone is quantified by the angle which sweeps around the geometric centre of the inner ring. In Figure 2.11, Ψ_L denotes the half of the load zone, Ψ denotes the angular position of any rolling element with respect to the centre of the load zone and x_m is the amount of relative displacement of the inner ring's geometric centre with respect to the outer ring's geometric centre.

An important point to infer from Figure 2.11 is that, the load zone occurs in the direction of the inner ring's displacement with respect to the outer ring's displacement, namely, x_m. This relative displacement is caused by the sum of the dynamic and static loads the bearing carries. In some rotary machines, static loads (i.e., the loads due to gravity) may dominate the dynamic loads (i.e., the unbalance loads, centrifugal loads etc.) while in some other machines, dynamic loads may be larger than static loads. It can be inferred from this interpretation that, in machines which are subjected to dominant dynamic loads, the load zone in those machines' bearings will be rotating around the geometric centre of the inner ring due to the fact that the net load will be dominated by dynamic loads, hence, it will be rotating. Similarly, in machines which are subjected to dominant static loads, the net load will be making very small, sometimes negligible oscillations around the static equilibrium position and thus, the load zone will be stationary.

The angular width of load zone is determined by the bearing's radial clearance, c_d, and the amount of relative displacement of the geometric centre of the inner ring with respect to the geometric centre of the outer ring, namely, x_m. The exact relationship to calculate the angular width of the load zone is given below [23].

$$\Psi_L = \cos^{-1}\left(\frac{c_d}{x_m}\right) \tag{2.7}$$

It should be remembered that the cage and the rolling elements are moving for the duration of the bearing's service. Therefore, as the cage of the bearing is rotating, different groups of rolling elements will be going in and out of the load zone. In other words, the group of rolling elements which are subjected to loads, and thus, deformations, will vary over time. The dynamic effects of this characteristic of ball bearings will be discussed in the next section.

2.2.2.2 Bearing frequencies

The load zone of a ball bearing, as discussed in section 2.2.2.1, has further effects on the dynamic behaviour of the bearing. As stated in previous sections, the individual rolling elements going into the load zone vary over time. Additionally, the individual normal load on each rolling element in the load zone is determined by the rolling element's angular position within the load zone, which is denoted by Ψ in Figure 2.11. This change of normal load on individual rolling elements causes individual deformations as the cage rotates. Therefore, the relative displacement between the inner and outer ring centres will change as a function of time. The situation explained here is depicted in Figure 2.12, for a ball bearing with 6 rolling elements.

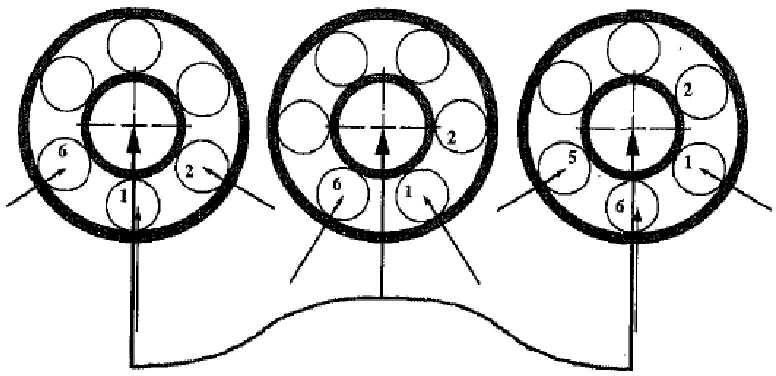

Figure 2.12 : Varying normal loads on different rolling elements of a ball bearing. Note that the inner ring is rotating counterclockwise [1, 26].

As expected, varying relative displacement between the inner and the outer rings will result in vibration. This vibration will be transferred from the inner ring to the shaft and from the outer ring to the bearing housing.

The frequency of the rolling elements passing through the load zone is called Ball Pass Frequency (BPF) and can be defined as the frequency of a rolling element passing through a reference point on the bearing. As can be inferred from the geometry of a ball bearing, the reference point may be on the outer raceway or on the inner raceway. Considering that the inner and outer rings rotate at different speeds, BPF for each raceway will be different. Therefore, there are two BPFs defined, one for each race. The frequency of a rolling element passing a fixed reference point on the outer race is called the Ball Pass Frequency Outer race (BPFO). Similarly, the frequency of a rolling element passing a fixed reference point on the inner race is called the Ball Pass Frequency Inner race (BPFI). The relationship between BPFO and BPFI is given below

$$BPFO + BPFI = \omega * N \tag{2.8}$$

where, N represents the number of rolling elements in the bearing and ω is the shaft speed.

It is possible to calculate both BPFs separately. The relationships given below show how BPFO and BPFI are calculated separately.

$$BPFO = \frac{N}{2}\omega\left(1 - \frac{d}{d_m}cos\alpha\right) \tag{2.9}$$

$$BPFI = \frac{N}{2}\omega\left(1 - \frac{d}{d_m}cos\alpha\right) \tag{2.10}$$

There are two other characteristic bearing frequencies which are related to geometric defects in the bearing. These frequencies are called the Ball Spin Frequency (BSF) and the Fundamental Train Frequency (FTF). Vibrations at BSF are seen when there is a defect on a rolling element itself. Similarly, vibrations at FTF are seen when the cage structure is defected. Similar to BPFs, it is possible to calculate BSF and FTF as shown below.

$$BSF = \frac{d_m}{2d}\omega\left(1-\left(\frac{d}{d_m}cos\alpha\right)^2\right) \tag{2.11}$$

$$FTF = \frac{\omega}{2}\left(1-\frac{d}{d_m}cos\alpha\right) \tag{2.12}$$

When new and healthy bearings are installed to a rotary machine and its vibration response is analysed, vibration components at the bearing frequencies will have significantly low amplitudes. However, as more and more defects start to occur in the bearing, a rise in the amplitudes of vibrations at corresponding frequencies is observed.

2.2.3 Rolling element – raceway contact mechanism in ball bearings

Some of the important characteristics of ball bearings are determined by the contact mechanism between the rolling elements and the rings. It was discussed in previous sections that, only the rolling elements which were within the load zone contribute to load carrying and are subjected to loads, leading to deflections. The rolling elements which are not within the load zone are not subjected to any deformations, hence, the contact between the unloaded rolling elements and the raceways is considered as a point contact. Figure 2.13 graphically illustrates a point contact occurring between a rolling element and the inner raceway.

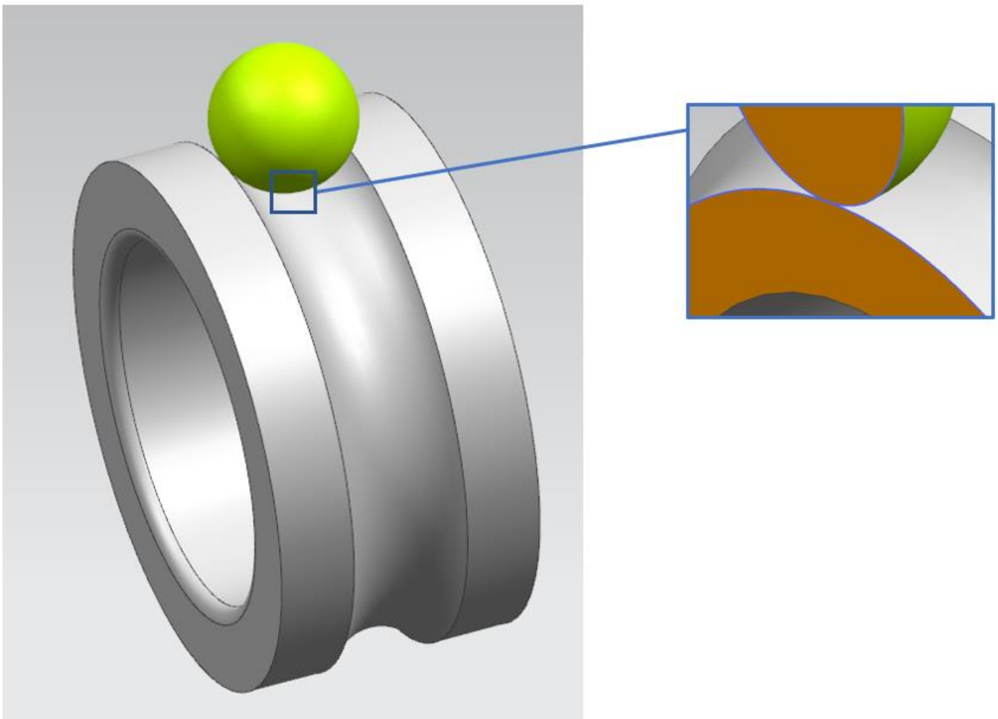

Figure 2.13 : Point contact between a rolling element and the inner raceway.

As seen in Figure 2.13, when the cross-section of the contacting rolling element – raceway pair is considered, it is seen that the contact is occurring between two circles, namely, the circumference of the rolling element and the momentary circumference of the raceway. The type of the contact between two pristine circles is a point contact, as two non-intersecting circles can only share a single point.

When a rolling element enters the load zone, the deflection seen in the rolling element and the raceway distorts the rolling element's and the raceway's circumferential cross-section, causing the point contact to turn into an area contact. The area formed by the deformations is an elliptical contact area, as shown in Figure 2.14.

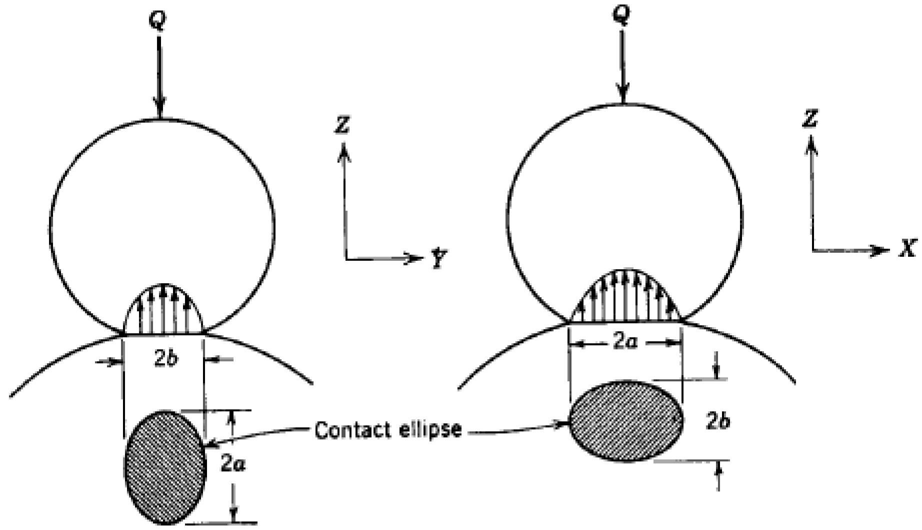

Figure 2.14 : Elliptical contact area between the ball and the inner raceway [27, 28].

For analytical and numerical models of ball bearings, this mechanism is of great importance due to the fact that the way the contact mechanism is modelled in an analytical or a numerical model greatly affects the accuracy of calculated contact forces; and thus, the estimated behaviour of the bearing. The well-known Hertzian contact theory is widely used to model the contact mechanisms of ball bearings. According to the Hertzian contact theory, the non-linear contact relationship is formulated as a non-linear spring between the contacting parts, as it is given below [23, 24, 28].

$$F_c = k_c \delta^{3/2} \tag{2.13}$$

In equation 2.13, F_c is the contact force in Newtons, k_c is the so-called contact stiffness in Newtons per $mm^{3/2}$ and finally, δ is the combined deformation of the contacting elements in mm.

Combined deformation of a rolling element and the raceway in contact is equal to the relative displacement of the rolling element's initial geometric centre with respect to the raceway's initial geometric centre, as depicted in Figure 2.15.

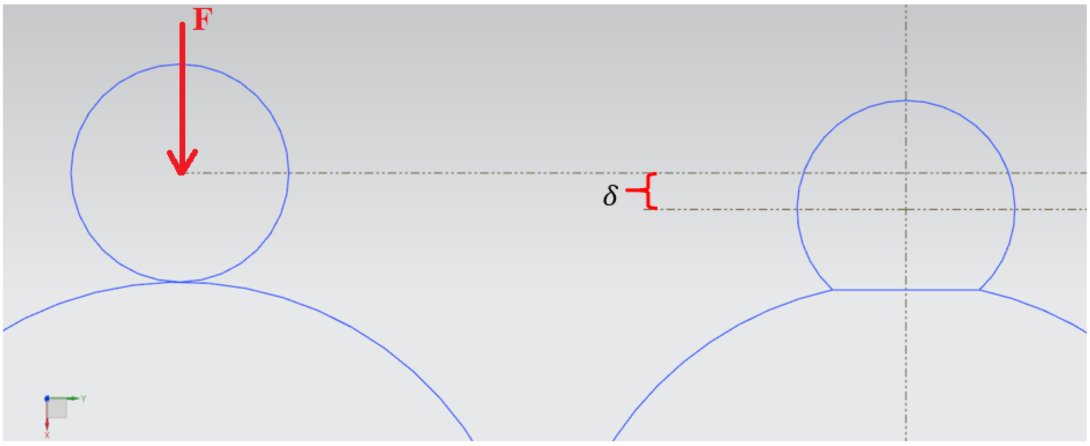

Figure 2.15 : Combined deflection of the contacting rolling element and inner raceway as denoted with δ.

Contact stiffness, k_c, is determined by the geometric and material properties of the ball bearing. As given in [27], the combined deflection of the bodies is calculated by equation 2.14.

$$\delta = \delta^* \left[\frac{3F_c}{2\sum\rho}\left(\frac{1-\upsilon_1}{E_1}+\frac{1-\upsilon_2}{E_2}\right)\right]^{2/3}\frac{\sum\rho}{2} \qquad (2.14)$$

In equation 2.14, υ_1 and υ_2 represent the Poisson's ratios of the contacting bodies (i.e., the rolling element and the raceway), E_1 and E_2 represent the Young's Moduli of the contacting bodies, $\sum\rho$ denotes the curvature sum of the contacting surfaces and δ^* denotes a unitless constant which is defined in a tabular form in [27].

Equation 2.14 is arranged to have the following form.

$$\delta^{3/2} = Y(\delta^*)^{3/2}\left(\sum\rho\right)^{1/2} F_c \qquad (2.15)$$

where, Y is defined as:

$$Y = \frac{3}{4\sqrt{2}}\left(\frac{1-\upsilon_1^2}{E_1} + \frac{1-\upsilon_2^2}{E_2}\right) \tag{2.16}$$

Equation 2.15 is arranged and put in the same form as equation 2.13 as shown below.

$$F_c = \left[\frac{1}{Y}\left(\sum \rho\right)^{-1/2} (\delta^*)^{-3/2}\right] \delta^{3/2} \tag{2.17}$$

Therefore, from equations 2.13 and 2.17, contact stiffness is deduced as below.

$$k_c = \frac{1}{Y}\left(\sum \rho\right)^{-1/2} (\delta^*)^{-3/2} \; [N/mm^{3/2}] \tag{2.18}$$

Curvature sum, $\sum \rho$, is calculated as:

$$\sum \rho = \rho_{I1} + \rho_{I2} + \rho_{II1} + \rho_{II2} = \frac{1}{r_{I1}} + \frac{1}{r_{I2}} + \frac{1}{r_{II1}} + \frac{1}{r_{II2}} \tag{2.19}$$

In equation 2.19, while the subscripts I and II represent the raceway and the rolling element, respectively, the subscripts 1 and 2 represent the two midplanes of the curvature. For a contacting pair of curved surfaces, aforementioned curvatures are depicted in Figure 2.16.

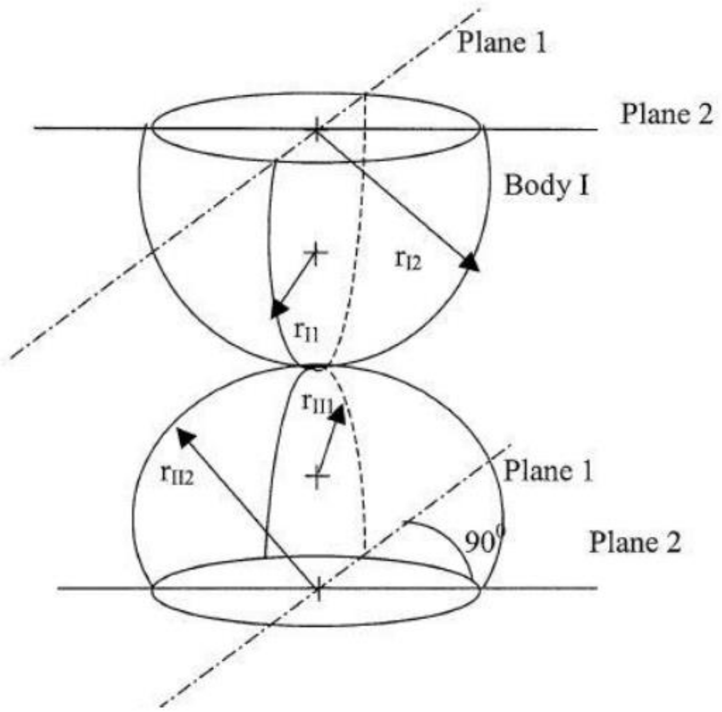

Figure 2.16 : Curvatures defined for a contacting pair with curved surfaces [28].

For the calculation of the unitless constant δ^*, the curvature function, $F(\rho)$, needs to be calculated first, using the following relationship as given in [27].

$$F(\rho) = \frac{(\rho_{I1} - \rho_{I2}) + (\rho_{II1} - \rho_{II2})}{\sum \rho} \tag{2.20}$$

Subsequently, using the table given by [27], the constant δ^* is calculated. The table used here is reproduced in Figure 2.17.

$F(\rho)$	δ^*
0	1
0.1075	0.997
0.3204	0.9761
0.4795	0.9429
0.5916	0.9077
0.6716	0.8733
0.7332	0.8394
0.7948	0.7961
0.83595	0.7602
0.87366	0.7169
0.90999	0.6636
0.93657	0.6112
0.95738	0.5551
0.97290	0.4960
0.983797	0.4352
0.990902	0.3745
0.995112	3176
0.997300	0.2705
0.9981847	0.2427
0.9989156	0.2106
0.9994785	0.17167
0.9998527	0.11995
1	0

Figure 2.17 : Values of the unitless constant δ^* for various values of the curvature function, $F(\rho)$ [27, 29].

2.3 Theoretical and Experimental Modal Analysis

When a mechanical system is considered, three types of distinct yet interrelated models of the system can be created. These models are named spatial model, modal model and response model. Spatial model represents the system by the system's spatial properties; namely, its overall stiffness and mass distribution. Modal model represents the system by its natural frequencies, damping and mode shapes. Response model, on the other hand, represents the system by its frequency response characteristics. It is possible to obtain the other two of the three models when one of them is known.

Additionally, it is possible take either a theoretical route or an experimental route to obtain all three models. Experimental route starts with measuring the system's frequency response functions in order to obtain the response model. Subsequently, through modal parameter identification, the modal model of the system is obtained using the response model. Finally, using the mathematical relationships between the modal parameters and the system's overall stiffness and mass distributions, the modal model is used to obtain the spatial model. On the other hand, theoretical route begins with theoretically (i.e., either numerically or analytically) creating the system spatial model by calculating the system's stiffness and mass distributions (matrices). Afterwards, an eigensolution is conducted to find the modal model of the system, using the information obtained from the spatial model. Finally, using in the modal model of the system, the system's response model is obtained. Figure 2.18 shows the theoretical and the experimental routes as well as how the three models are interconnected, depending on the selection of the route.

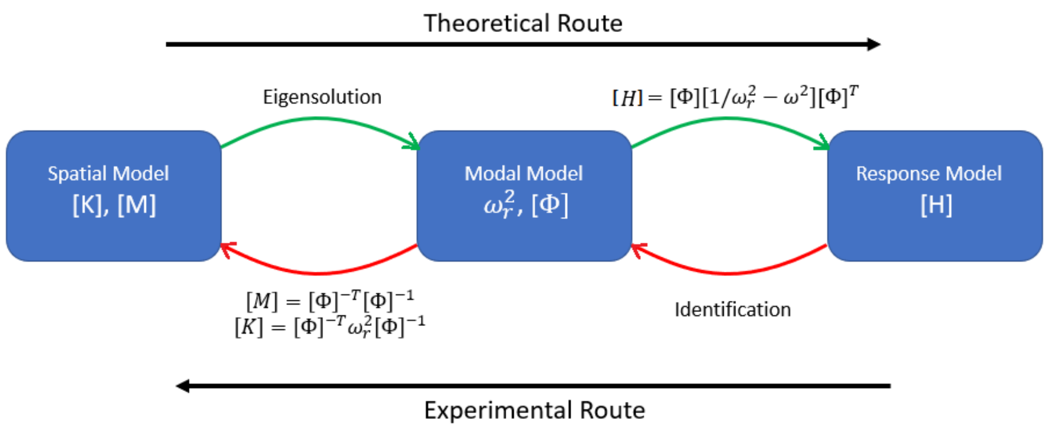

Figure 2.18 : Routes in experimental and theoretical modal analysis in order to obtain spatial, modal and response models.

Before discussing experimental and theoretical modal analyses, a number of important concepts need to be defined here. One of these concepts is the Impulse Response Function (IRF), $h(t)$, which is defined as a system's response in time domain to a unit-impulse input. The importance of impulse response function is due to the fact that it can be used to calculate a system's response in time domain to an arbitrary input as shown in a mathematical form in equation 2.21.

$$y(t) = \int_0^t x(t)\, h(t-\tau)\, d\tau \tag{2.21}$$

Equation 2.21 is also known as Duhamel's Integral. In equation 2.21, $x(t)$ and $h(t-\tau)$ are the arbitrary input to the system and the impulse response function of the system, respectively. $y(t)$ is the system's response in time domain to the arbitrary input.

The frequency domain counterpart of the impulse response function is the Frequency Response Function (FRF). Frequency response function is mathematically defined as given in equation 2.22.

$$H(\omega) = \frac{Y(\omega)}{X(\omega)} \tag{2.22}$$

In equation 2.22, ω is frequency, $H(\omega)$ is the frequency response function, $X(\omega)$ is the input and $Y(\omega)$ is the output, or the response, in frequency domain. Frequency response function of a system is the forward Fourier Transform (FT) of the system's impulse response function. Similarly, impulse response function of a system is the inverse Fourier transform of the system's frequency response function.

2.3.1 Experimental modal analysis

As stated previously, the experimental route begins with measuring necessary response characteristics in order to build the response model of the system. It is usually done by taking a planned set of FRF measurements by means of impact or shaker tests. For a typical FRF measurement, the structure to be tested is instrumented with appropriate vibration sensors. The reader is advised to read the literature on the subject for more details on how an appropriate accelerometer is selected for FRF measurement. Figure 2.19, shows the general steps of a typical experimental modal analysis procedure.

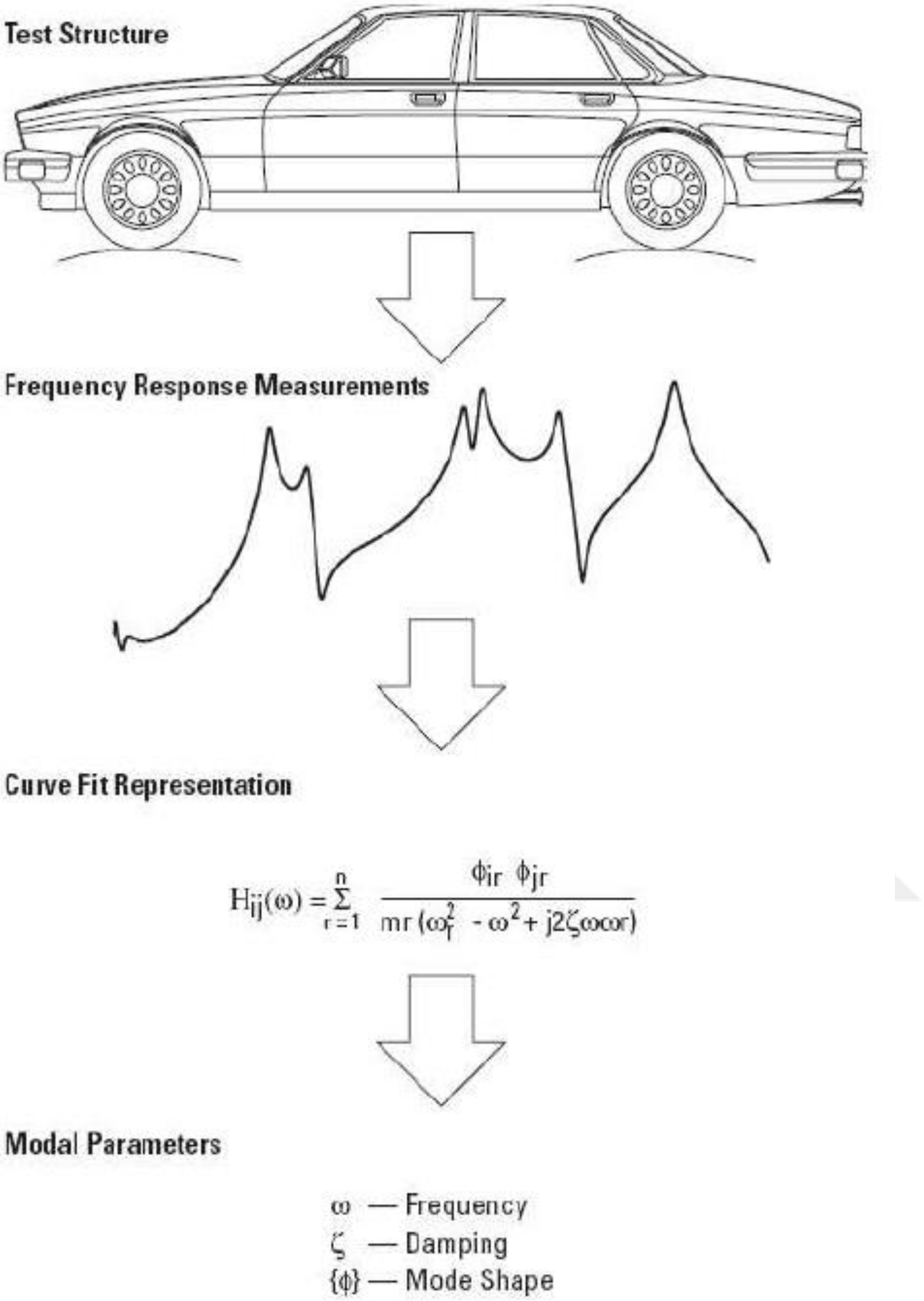

Figure 2.19 : A depiction of general experimental modal analysis procedure [1, 30].

As seen in Figure 2.19, firstly, frequency response measurements are conducted to obtain the FRFs of the system. Secondly, curve fit techniques are applied to the FRF data, which finally yield the modal parameters, namely, natural frequencies and their corresponding mode shapes as well as modal damping.

Instrumented impact hammers, also known as modal hammers, are used for impact tests. An impact excites the system in a wide frequency range. The upper limit of this frequency range depends on the material used on the tip of the hammer. In order to excite more complex structures, shakers can be used. A shaker has a rod which is used to attach the shaker to the system to excite it with a given frequency profile. Figure 2.20 shows some examples of modal hammers and shakers [1].

Figure 2.20 : Modal hammers and shakers used for experimental modal analysis [1].

The system's response to the excitation either by a modal hammer or a shaker is usually measured with an accelerometer as modern accelerometers can capture responses in a very wide frequency range.

2.3.2 Theoretical modal analysis

Theoretical modal analysis begins with building the spatial model, as outlined in Figure 2.18. Typically, a finite element method approach is taken to generate the system's global stiffness (K) and mass (M) matrices. The reader is advised to read the literature on finite element method for more details on how a system's global stiffness and mass matrices are calculated. Subsequently, the eigenproblem for the system is solved. The eigenproblem for a mechanical system whose spatial model is represented by the global matrices K and M is given in equation 2.23, where ω_r represent the natural frequencies and U_r represent the corresponding mode shapes of the system.

$$([K] - \omega_r^2[M])\{U_r\} = \{0\} \qquad (2.23)$$

The solution of the eigenproblem yields the modal model of the system. An additional step in theoretical modal analysis can be used to obtain the response model from the modal model using equation 2.24.

$$[H] = [\Phi]\begin{bmatrix} \ddots & & 0 \\ & \frac{1}{\omega_r^2 - \omega^2} & \\ 0 & & \ddots \end{bmatrix}[\Phi]^T \tag{2.24}$$

In equation 2.24, $[H]$ denotes the FRFs of the system, $[\Phi]$ denotes the mass-normalised mode shape matrix and ω denotes the excitation frequency.

2.4 Electric Motors

Although there are many different types of electric motors designed for various working conditions and requirements, only the most general types are covered in this section and the reader is advised to consult appropriate literature for more details on electric motors. Mainly, electric motors can be divided into two categories: Direct current (DC) motors and alternating current (AC) motors.

2.4.1 Direct current (DC) electric motors

A DC electric motor is an electrical machine which uses direct current to convert electrical power to mechanical power. Brushed and brushless DC motors are the two types of DC motors which are widely used in industry.

The power generation mechanism of a typical brushed DC motor consists of a permanent-magnet stator, a wound rotor and a commutator. A constant magnetic field is created by the stator around the rotor. The commutator transfers the direct current generated by the power source to rotor windings. As a result of current flow through the rotor windings in a constant magnetic field, electromagnetic forces are created on the windings of the rotor. These electromagnetic forces cause the rotor to rotate about its normal axis. The commutator is also responsible for controlling the direction of the direct current through the windings to ensure that the torque the motor generates is always in the same direction. The figure below, Figure 2.21, depicts the cycle of operation of a typical DC motor [1].

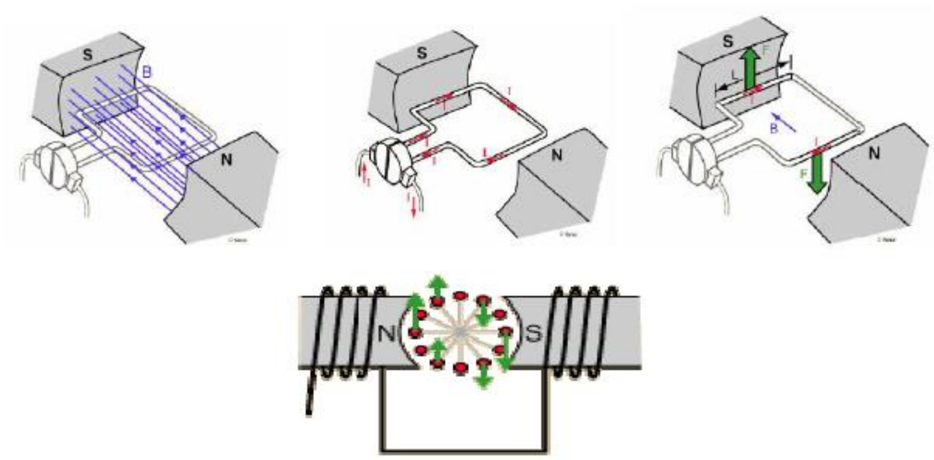

Figure 2.21 : Electromagnetic forces and torque generated by a DC motor [1].

The type of DC electric motor depicted in Figure 2.21, namely, the type which has a permanent-magnet stator is also called the brushed DC motor. Another kind of DC motor is the brushless DC motor, or BLDC. A BLDC consists of a permanent-magnet rotor and a wound stator. When direct current is flowing in the stator windings (or poles), the poles of the stator become electromagnets whose polarity depends on the direction of the current. After the poles are electromagnetised, the torque is generated by the electromagnetic force interaction between the electromagnet stator and the permanent-magnet rotor. The poles of the stator are polarised by the electronic controller unit such that while poles of opposite polarity from the magnets on the rotor pull the rotor in one direction, poles of same polarity as the magnets on the rotor push the rotor in the same direction. Figure 2.22, illustrates the torque generation mechanism in a typical BLDC.

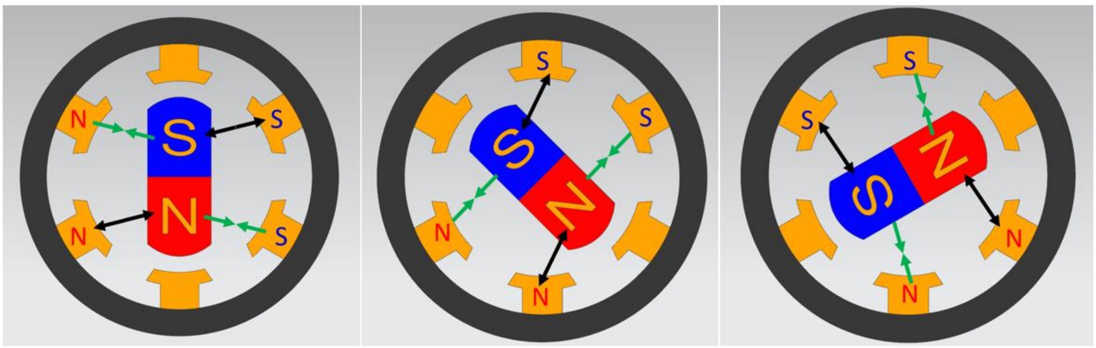

Figure 2.22 : Torque generation mechanism in a typical brushless DC motor.

When the BLDC’s torque generation mechanism is considered, it can be inferred that stator poles are polarised depending on the angular position of the rotor. Therefore, in a BLDC, the rotor’s angular position needs to be known by the electronic controller so that it can polarise the poles accordingly. For this purpose, usually a so-called “hall effect sensor” is used in BLDCs to sense the rotor’s angular position.

2.4.2 Alternating current (AC) electric motors

Though there are a number of different types of AC electric motors, induction motors are the ones mostly used in the industry. A typical AC motor consists of a wound stator and a squirrel cage rotor. The stator and rotor of a typical induction motor is shown in Figure 2.23.

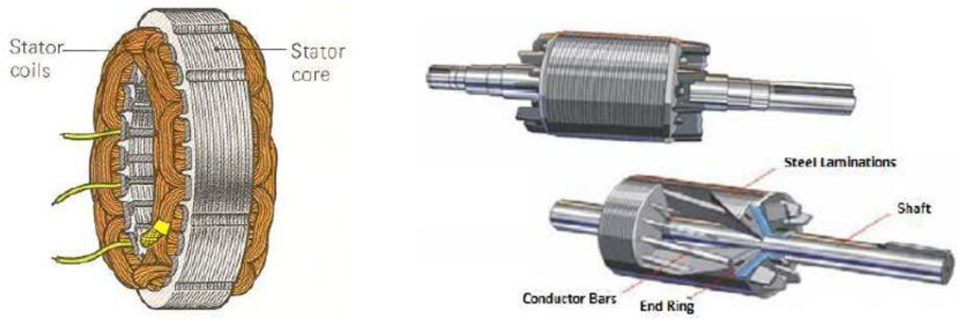

Figure 2.23 : The stator and rotor of an induction motor [1].

When the stator windings are powered with a three-phase alternating current, a rotating magnetic field is created around the stator. The speed of the rotating magnetic field is called the synchronous speed. The mathematical relationship between the synchronous speed, electrical line frequency and number of stator poles is given in equation 2.25, where N_S denotes the synchronous speed, F_L denotes the line frequency and P denotes the number of stator poles.

$$N_S = \frac{2F_L}{P} \tag{2.25}$$

When the conducting metal bars of the rotor and the rotating magnetic field are considered, current is generated in rotor bars according to Faraday’s Law. According to Lorentz’s Law, electromagnetic forces are generated on current-carrying loops in a magnetic field. Therefore, electromagnetic forces are generated on rotor bars which produce torque and rotate the rotor.

No electromagnetic forces are created on the conductor bars whenever the rotating magnetic field does not cut through the loop made by the rotor bars. At such instance, as there are no electromagnetic forces acting on the rotor bars, the rotor starts to slow down. As the rotor slows down, the stator's magnetic field keeps rotating and starts to cut through the rotor bar loops again which creates electromagnetic forces on the bars and speeds up the rotor. Due to this characteristic of the induction motor, the rotor speed is slightly lower than the synchronous speed. The difference between the rotor speed and the synchronous speed is called slip and defined as shown in equation 2.26, where N_S and N_{rotor} are the synchronous speed and the rotor speed in RPM, respectively.

$$slip\% = \frac{N_S - N_{rotor}}{N_S} x100 \tag{2.26}$$

2.4.3 Mechanical causes of noise and vibration in electric motors

There are a number of mechanical sources creating vibrations in electric motors. These vibration sources may emerge during manufacturing, installation or operation of the electric motor. The main mechanical sources of noise and vibration in electric motors are unbalance, misalignment, eccentricity, bent shaft, mechanical looseness and faulty ball bearings.

2.4.3.1 Unbalance

One of the causes of unbalance in electric motors is the centre of mass of the rotor not being aligned with the rotor's centre of geometry. When centre of mass is offset from centre of geometry, unbalance force is created at the centre of mass of the rotor, which pulls the rotor further away from the rotor's centre of geometry. Unbalance forces rotate at the same frequency as the rotor and thus, radially excite the machine at rotational frequency of the rotor. Unbalance forces show up as peaks at 1 times the rotor speed in the machine's vibration spectrum (the 1X frequency) as shown in Figure 2.24. Unbalance may occur due to a number of reasons which include manufacturing, operation of the machine and other external causes. It should be noted that the rotor may also be unbalanced even though the centre of mass of the rotor is aligned with the rotor's centre of geometry. This type of unbalance is usually called dynamic unbalance which requires a more complicated balancing operation. However, dynamic unbalance also produces vibrations at the rotational frequency of the rotor.

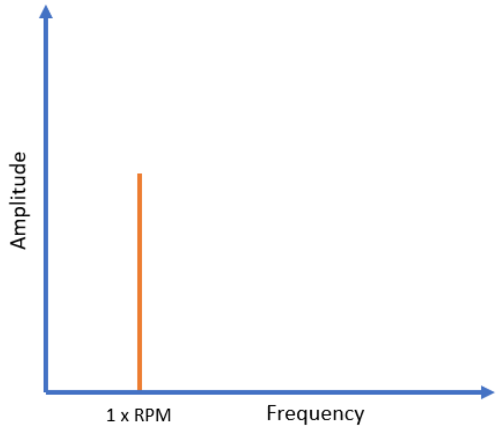

Figure 2.24 : Spectrum of vibration due to unbalance [31].

2.4.3.2 Misalignment in couplings

Misalignment between two coupled machines may occur in the coupling connecting the two machines. Misalignment is defined as the centres of geometry of the machines' shafts being offset from each other in radial, angular or both directions. Parallel misalignment occurs when the shafts are only radially offset. Similarly, angular misalignment occurs when the shafts are offset only in the angular direction. In most cases of misalignment in real applications, misalignment is a combination of parallel and angular misalignments. Misalignment creates a vibration spectrum with frequency components at 1, 2 and sometimes 3 times the rotor speed in both radial and axial directions as shown in Figure 2.25.

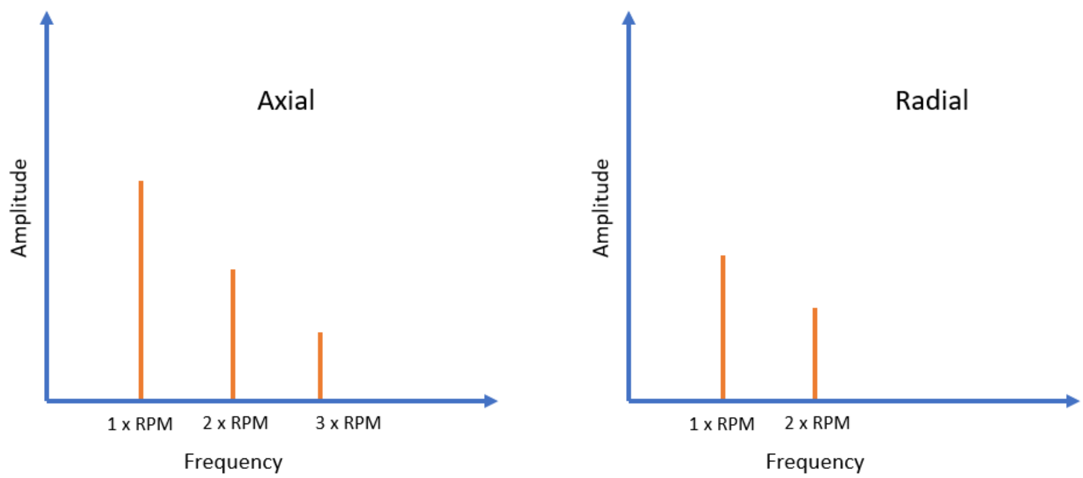

Figure 2.25 : Spectra of axial and radial vibrations caused by misalignment [31].

2.4.3.3 Shaft eccentricity

Eccentricity between the shaft's centre of geometry and rotation axis causes vibrations at 1X frequency in the radial direction. Eccentricity may occur due to bearing mounting faults, rotor faults or stator lamination faults as shown in Figure 2.26.

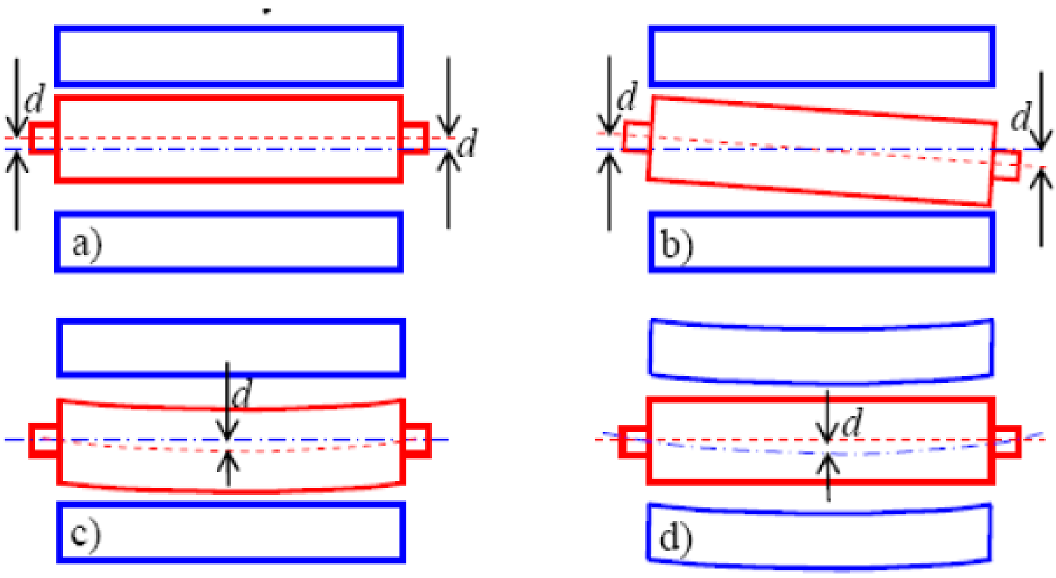

Figure 2.26 : Eccentricity due to a, b) faults in mounting of the bearings; c) rotor faults; d) stator lamination faults [1].

2.4.3.4 Bent shaft

Vibrations at 1X and 2X frequency occur in radial and axial directions when the shaft is excessively bent. Bent shaft may occur due to excessive shaft load or heat, insufficient shaft strength or excessive unbalance. Spectra of axial and radial vibrations caused by bent shaft is shown in Figure 2.27.

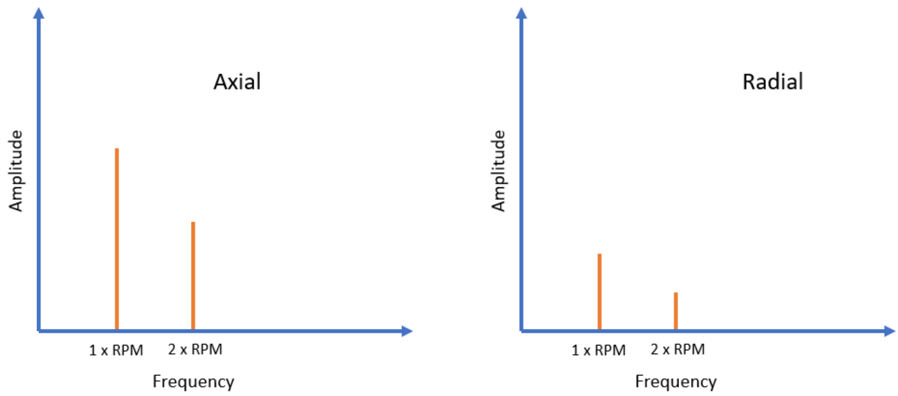

Figure 2.27 : Axial and radial vibrations caused by bent shaft [31].

2.4.3.5 Mechanical looseness

Mechanical looseness occurs when bearings are not installed tightly in the housings or the machine is not mounted tightly to the carrying structure. In the case of mechanical looseness, shaft rotation causes many small impacts either between the bearing and the housing or the machine and the carrying structure. Such impacts create vibration at 1X frequency and its harmonics up to 10X in the radial direction, as shown in Figure 2.28.

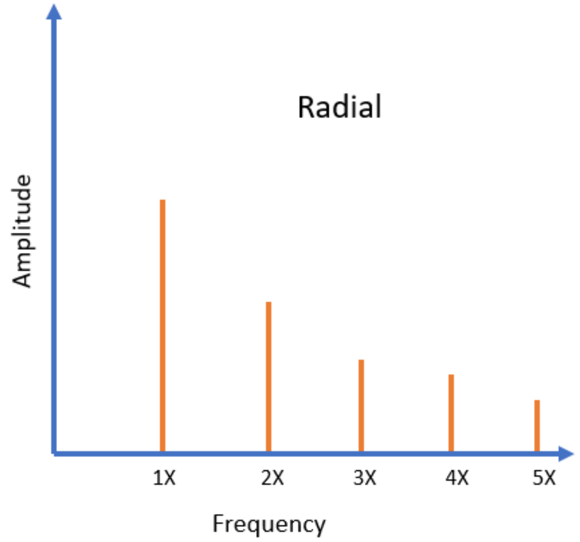

Figure 2.28 : Spectrum of vibrations caused by mechanical looseness [31].

2.4.3.6 Faulty ball bearings

Faults emerge in ball bearing components over time during their operation. Dents, cracks or similar defects occur in the rolling elements or the rings. Additionally, the cage structure may also become damaged or defected due to various reasons. It was shown previously that ball bearings always generate vibrations by their design and nature. Faulty ball bearings generate higher levels of vibrations at respective fault frequencies. For example, a ball bearing with a defected outer ring will generate increased level of vibrations at BPFO.

2.4.4 Electrical causes of noise and vibration in electric motors

Though there are many different electrical sources of noise and vibration in electric motors, only those which can be seen in BLDC motors are discussed in this thesis, including eccentricity, magnetostriction, cogging torque, fluctuation of forces between stator and rotor.

2.4.4.1 Eccentricity between stator and rotor

Eccentricity between the centres of geometry of rotor and stator cause vibration in electric motors. In the case of eccentricity, the airgap between the stator and the rotor changes as the rotor rotates. Due to the changing airgap, magnetic forces exciting the rotor change both in amplitude and in harmonic components, yielding vibrations in the rotor. A case of eccentricity between the rotor and the stator is shown in Figure 2.29.

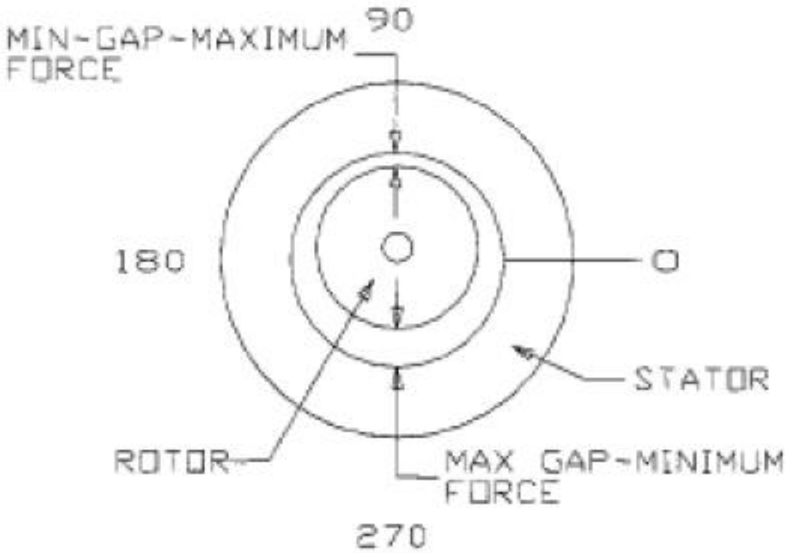

Figure 2.29 : Eccentric rotor and stator in an electric motor [1].

2.4.4.2 Magnetostriction

Magnetostriction is defined as straining of ferrous materials in a magnetic field. Straining of the laminations of stator causes changes in magnetic flux, which causes noise and vibration in the motor.

2.4.4.3 Cogging torque

Cogging torque is the fluctuating torque generated in the circumferential direction in the airgap of the electric motor. Cogging torque is calculated by equation 2.27, where L is the axial dimension of the rotor, R is the radius of an arbitrary circle taken to be in the air gap, μ_o is the permeability of rotor magnet, θ_s is the angular displacement of the stator, B_r and B_θ are the flux densities on the inner and outer surface of the stator, respectively [32].

$$T_{cog}(t) = \frac{LR^2}{\mu_o} \int B_r B_\theta d\theta_s \qquad (2.27)$$

Cogging torque creates vibrations at a frequency equal to 1X times the lowest common multiple of the number of slots and poles [32].

2.4.4.4 Ripples of mutual and reluctance torque

The output torque of BLDC motors has a constant and a fluctuating part. The fluctuating part is called the ripples of mutual and reluctance torque and creates excitations at 6X and its higher harmonics [32].

2.4.4.5 Attractive force fluctuations between stator and rotor

Fluctuations in attractive forces between the stator and the rotor are related to the spatial distribution of these forces. These fluctuations create vibrations at a frequency equal to 1X times the number of poles and its harmonics [32].

2.5 Component Mode Synthesis

Component mode synthesis is an important method which is extensively used in advanced dynamic simulations to reduce model complexity and computation times [33, 34]. Most modern finite element models consist of a significantly large number of DOFs, often on the order of millions. These million-DOF models demand a substantial amount of computing power and component mode synthesis methods are used to significantly decrease the number of DOFs required to model a mechanical system. Component mode synthesis methods are also useful when a complex mechanical system which can be represented as a combination of connected sub-systems [33].

One of the most widely-used component mode synthesis method is the Craig-Bampton Method [34, 35]. In the Craig-Bampton Method, the complex structure to be modelled is treated as an assembly of distributed sub-structures [35]. By definition, these sub-structures have boundary nodes which are used to interconnect one sub-structure to another or apply various boundary conditions to the sub-structure such as forces, moments or kinematic constraints [34]. Any node which is not a boundary node is called an interior node in the Craig-Bampton Method. A generic finite element model using interconnected sub-structures is depicted in Figure 2.30.

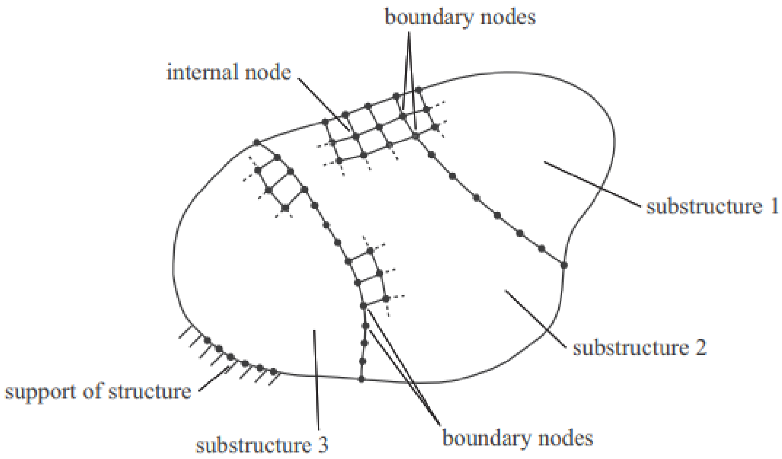

Figure 2.30 : A generic finite element model of a system consisting of interconnected sub-structures [34].

In the Craig-Bampton Method, the equations of motion are partitioned as below [34, 35]:

$$\begin{bmatrix} M_{bb} & M_{bi} \\ M_{ib} & M_{ii} \end{bmatrix} \begin{Bmatrix} \ddot{u_b} \\ \ddot{u_i} \end{Bmatrix} + \begin{bmatrix} C_{bb} & C_{bi} \\ C_{ib} & C_{ii} \end{bmatrix} \begin{Bmatrix} \dot{u_b} \\ \dot{u_i} \end{Bmatrix} + \begin{bmatrix} K_{bb} & K_{bi} \\ K_{ib} & K_{ii} \end{bmatrix} \begin{Bmatrix} u_b \\ u_i \end{Bmatrix} = \begin{Bmatrix} F_b \\ F_i \end{Bmatrix} \tag{2.28}$$

where u_b are the degrees of freedom of the boundary nodes and u_i are the degrees of freedom of the interior nodes. Subsequently, the so-called Craig-Bampton Transformation is applied as below [34, 35]:

$$\begin{Bmatrix} u_b \\ u_i \end{Bmatrix} = \begin{bmatrix} I & 0 \\ \Phi_c & \Phi_n \end{bmatrix} \begin{Bmatrix} u_b \\ q \end{Bmatrix} = [\Psi] \begin{Bmatrix} u_b \\ q \end{Bmatrix} \tag{2.29}$$

where Φ_c is the matrix of the normal modes calculated while all boundary DOFs are fixed, Φ_n is the matrix of the so-called static constraint modes, q are the generalised displacements and I is the identity matrix. Then, the reduced stiffness and mass matrices of the system, $[K_r]$ and $[M_r]$, are calculated as [34, 35]:

$$[K_r] = [\Psi^T][K][\Psi] \tag{2.30}$$
$$[M_r] = [\Psi^{\mathrm{T}}][M][\Psi] \tag{2.31}$$

Subsequently, the below eigenproblem is solved [34]:

$$[K_r]\{X\} = \rho[M_r]\{X\} \tag{2.32}$$

where ρ are the predictions for the eigenvalues. Finally, the predictions for the eigenvectors, $[\bar{\Phi}]$, are given as [34]:

$$[\bar{\Phi}] = [\Psi]\{X\} \tag{2.33}$$

2.6 Numerical Calculation of the Contact Forces in MSC Adams

A summary of the theory used by the multibody dynamic modelling software MSC Adams, which is used for the simulations in this thesis, to numerically calculate the contact forces is given for convenience. IMPACT function in MSC Adams is used to calculate the contact forces in the ball bearings of the motor. A depiction of a contact situation in an MSC Adams simulation is given below in Figure 2.31.

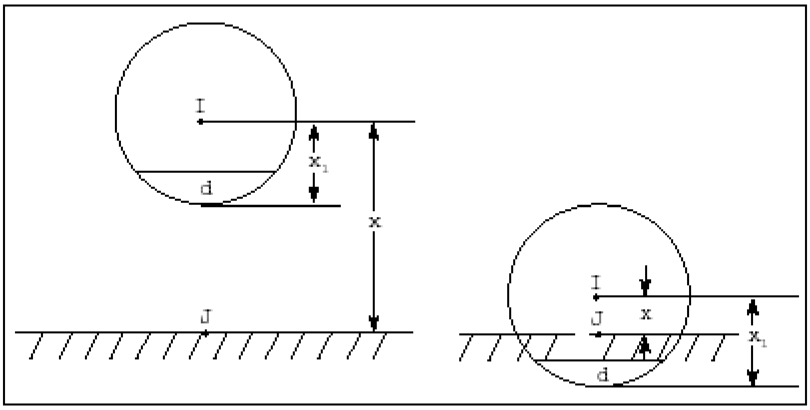

Figure 2.31 : A contact situation occurring in MSC Adams [36].

The contact force in MSC Adams has a stiffness and a viscous damping component. As seen in Figure 2.31, there is no contact when x is greater than or equal to x_1 so MSC Adams calculates zero contact force for such situation. However, when x is less than x_1, MSC Adams interprets such situation as a physical contact and calculates the value of the contact force using the below relationship [36]:

$$\begin{aligned} F_{contact} = MAX(0, k_{contact}(x - x_1)^e \\ - STEP(x, x_1 - d, c_{max}, x_1, 0) * \dot{x}) \end{aligned} \tag{2.34}$$

where e is the force exponent entered by the user, $k_{contact}$ is the contact stiffness entered by the user, c_{max} is the maximum damping coefficient entered by the user and x_1 is the free length of x.

3. TESTS AND MEASUREMENTS

A series of tests and measurements are conducted in order to identify the modal and dynamic characteristics of the Atlas motor experimentally and also to provide reference data for the validation of the numerical model. The so-called Atlas motor is a small, 500-Watt BLDC motor designed to drive some washing machines. The Atlas motor is designed to operate between 500 – 14000 RPM. The Atlas motor is commutated through an encoder instead of a Hall Effect sensor.

The outline of the measurements described and presented in the next subsections is as follows. Firstly, FRF measurements are taken from individual components of the motor, namely, the front cover (coded as KT, which is an abbreviation for “belt side” in Turkish), the rear cover (coded as KTA, which is an abbreviation for “opposite of belt side”), the stator and the rotor. Secondly, the FRFs of the assembly of KT, KTA covers and the stator are measured. This subassembly group is modelled as an assembly of flexible parts (flexbody) in the numerical models, therefore, it is considered important to identify the modal characteristics of this group experimentally for the validation of the flexible subassembly model. All FRFs are measured in the form of inertance, under free-free conditions. Thirdly, Campbell Diagrams of 6 fully-assembled motors, which had different features, are measured. These assemblies comprised loaded and unloaded motors with healthy and faulty bearing combinations, as explained later in a forthcoming section. Lastly, vibration measurements are made under steady-state operations of the motors in order to identify their steady-state characteristics as well as to use the measured data for model validation purposes. The maximum shaft speed is selected as 10000 RPM as the spin speed is 1000 RPM in most washing machines and there is a 1:10 speed ratio between the drum and the electric motor. Natural frequencies and vibrations up to 3200 Hz are measured.

The measurement setup used for necessary data acquisition and signal processing for the FRF measurements consists of a Brüel & Kjaer LAN-XI multi-channel data acquisition system, a portable computer, a Brüel & Kjaer Type 4507 B 1-axis accelerometer and a Dytran Dynapulse 5800 modal hammer. For Campbell Diagram measurements, a similar measurement setup is used with a Brüel & Kjaer Type 2981 laser tachometer to measure the shaft speed.

3.1 FRF Measurements of the Motor Components

FRFs of the KT cover are measured first. The measurement setup is illustrated in Figure 3.1. As can be seen, the KT cover is suspended using a highly flexible string, simulating free-free condition for FRF measurements.

Figure 3.1 : FRF measurement scenario for the front cover.

One of the measured FRFs is presented in Figure 3.2. The first five elastic modes of the KT cover between 0 and 3200 Hz are very clearly seen in Figure 3.2. The natural frequencies of these modes are, in ascending order, 872 Hz, 1341 Hz, 1930 Hz, 2175 Hz and 3113 Hz, respectively.

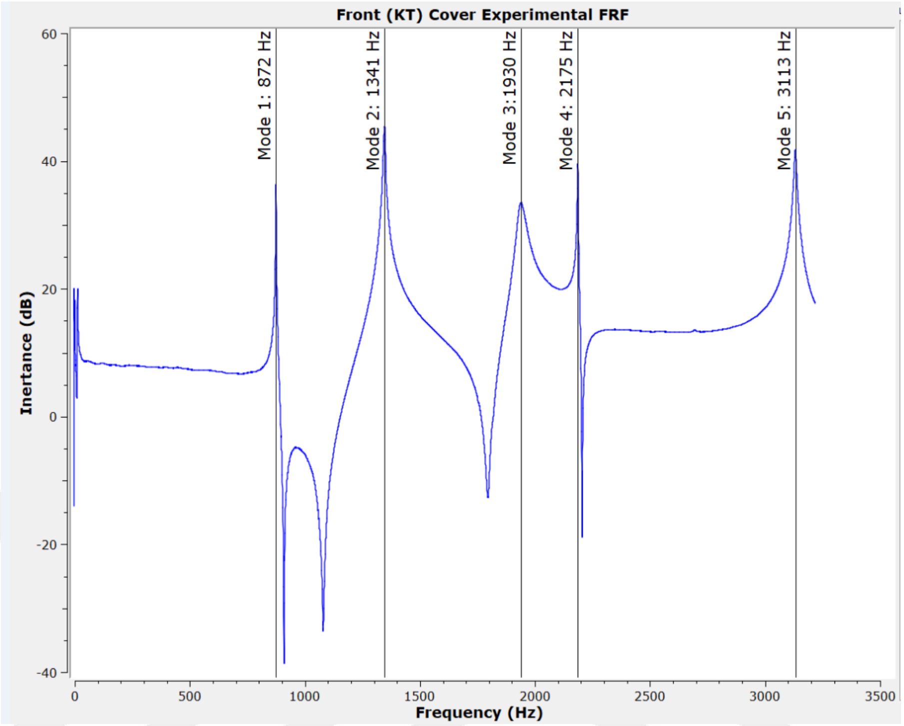

Figure 3.2 : Measured FRF of the front cover.

Next, FRFs of the KTA cover are measured under free-free conditions again. An image of the suspended specimen for the KTA cover and one of the measured FRFs are shown in Figure 3.3a and Figure 3.3b, respectively. As identified in Figure 3.3b, the first four natural frequencies for elastic modes of the KTA cover are determined to be 1157 Hz, 1252 Hz, 2390 Hz and 2938 Hz.

a)

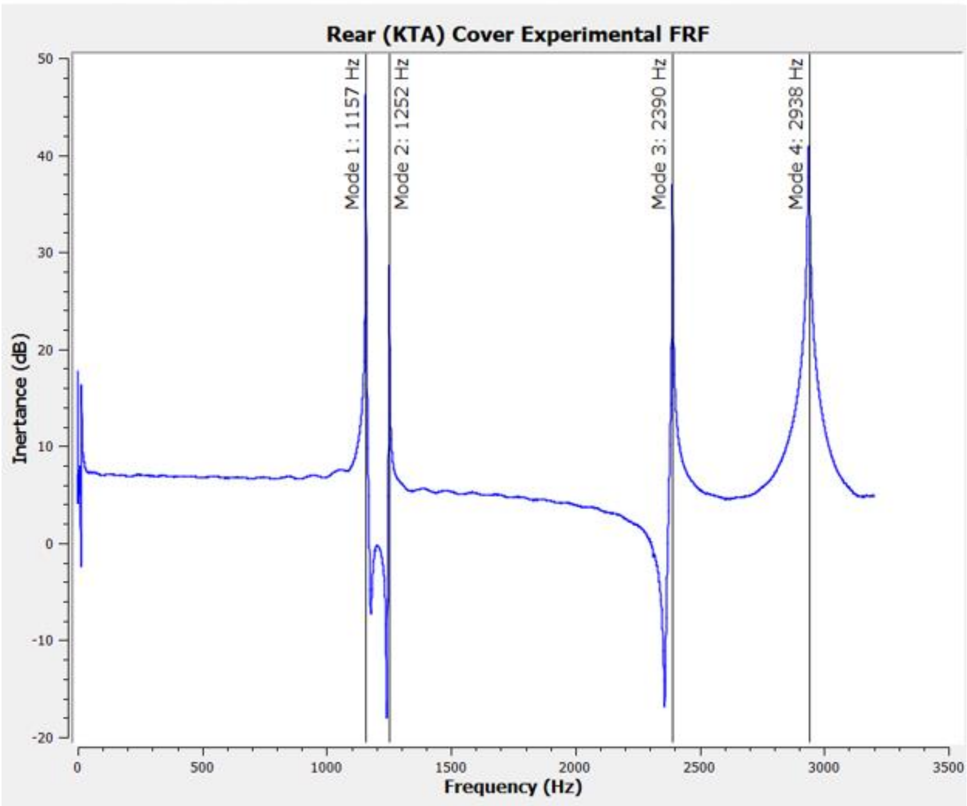

b)

Figure 3.3 : a) Suspended KTA specimen for FRF measurement and b) one of the measured FRFs.

The stator is the third component which is used for FRF measurements. The suspended stator is presented in Figure 3.4a which also shows the excitation and response directions for a particular FRF illustrated in Figure 3.4b. As shown in Figure 3.4b, there are three modes up to 3.2 kHz, which are identified at 986 Hz, 1516 Hz and 3133 Hz. The experimentally-identified modes at these frequencies correspond to the stator’s in-plane modes. When the stator vibrates at these modes, the laminations of the stator move in the same plane without any relative displacement/motion between individual laminations. The stator of the Atlas motor consists of 50 laminations attached together with four pins as well as the constraining friction force between them. Due to high levels of damping caused by the friction between the laminations, it is very difficult to measure the out-of-plane modes of the stator. Although not visible in the measured FRFs, the validated numerical models which are given in subsequent sections suggest that there may well be an out-of-plane stator mode between 1516 Hz and 3133 Hz.

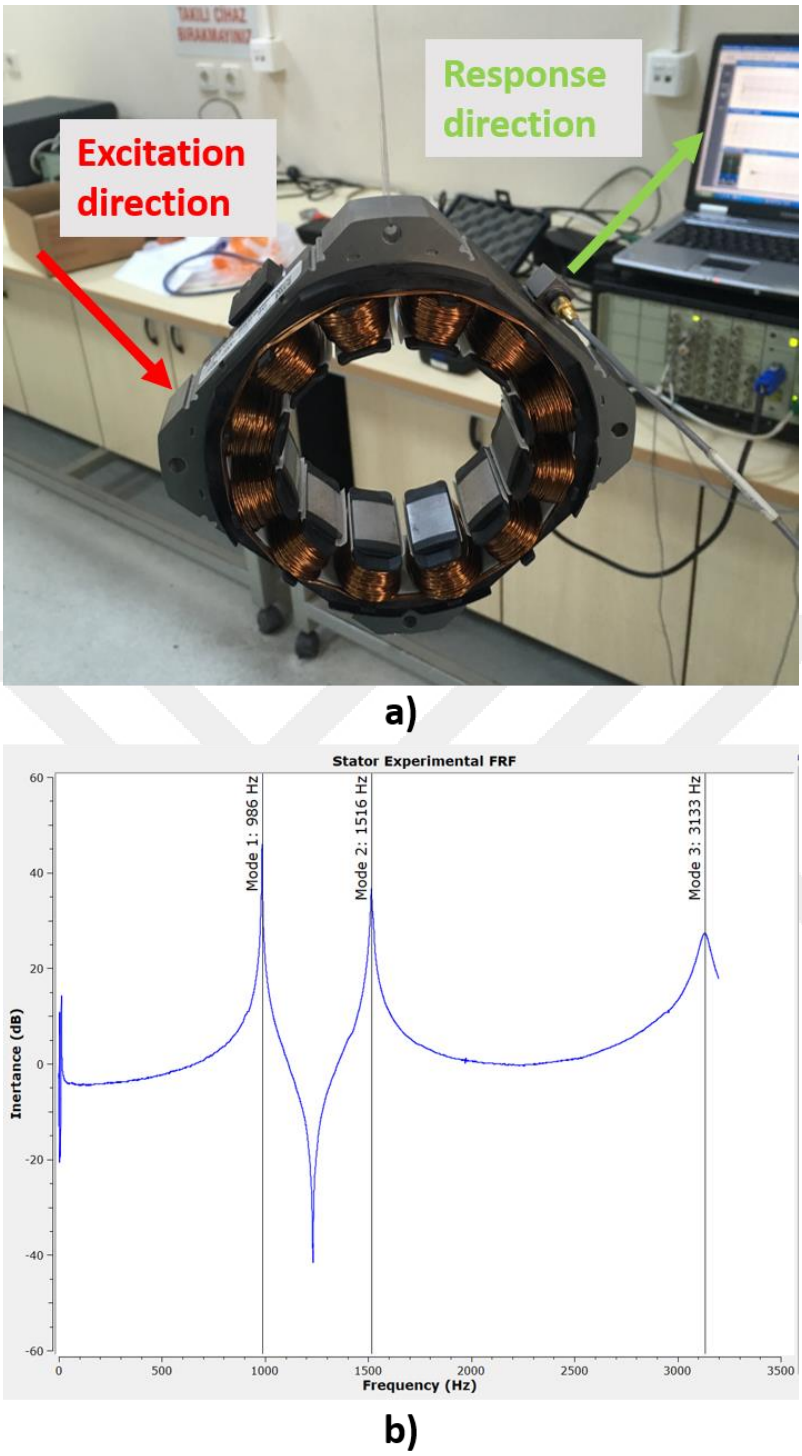

Figure 3.4 : a) Suspended stator specimen for FRF measurements and b) one of the measured FRFs.

Hammer test is also applied to the fourth component, the rotor, for FRF measurements. As opposed to the previous FRF measurements, the inverse of inertance, also known as the apparent mass, is measured. In the series of measurements, the rotor is suspended both vertically and horizontally with respect to the ground, which allowed for both radial and axial excitation of the rotor. Similarly, the accelerometer is mounted both radially and axially in order to collect data from both directions. Figure 3.5 shows one of the configurations used for the horizontal suspension of the rotor and accelerometer placement, where it was excited axially from the right side of the rotor shaft.

Figure 3.5 : Horizontally suspended rotor.

One of the measurements taken from the rotor in the configuration shown in Figure 3.5 and its phase information is shown in Figure 3.6.

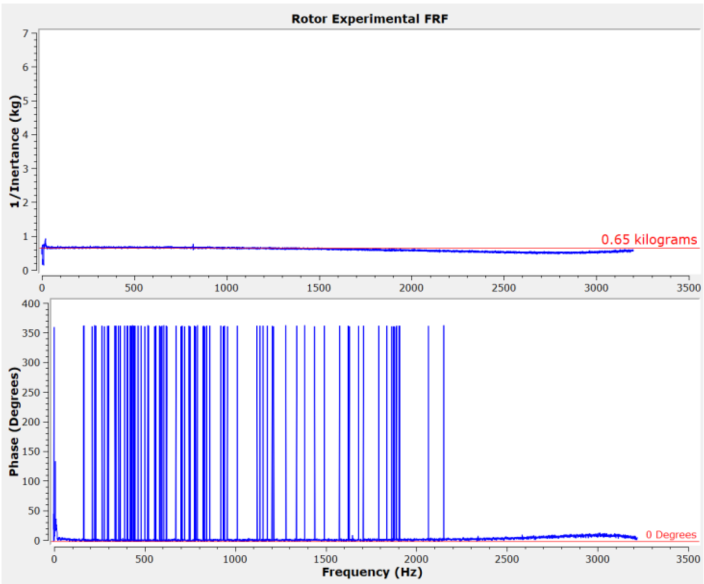

Figure 3.6 : Apparent mass of the horizontally-suspended and axially-excited rotor.

As seen in Figure 3.6, the apparent mass is almost a straight line and the phase information is nearly constant at zero degrees. The rotor's mass is measured to be around 0.65 kilograms, and the apparent mass of the rotor is almost constant and equal to the actual mass of the rotor. Similarly, the rotor is suspended vertically and excited radially. However, it should be noted that the front end of the rotor had to be cut to allow for the disassembly of the motor. Hence, the mass of the uncut rotor is higher and measured to be around 0.75 kilograms by the manufacturer. The vertically-suspended rotor and one of its measured FRFs corresponding to radial excitation are given in Figure 3.7a and Figure 3.7b, respectively. Consequently, it is inferred that between 0 and 3200 Hz, the rotor behaves almost as a rigid body in both axial and radial directions.

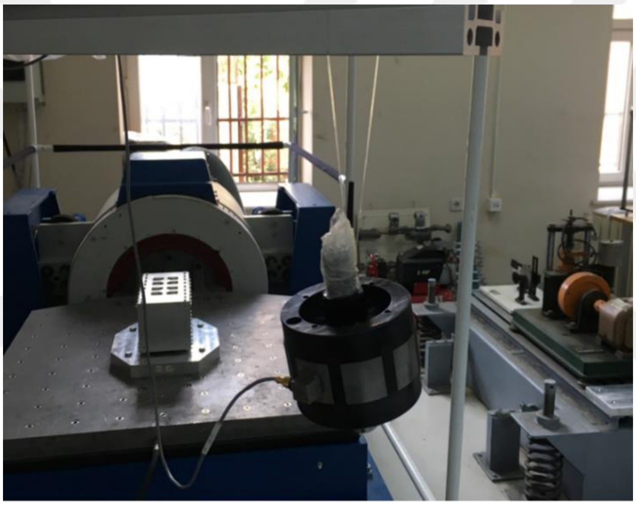

a)

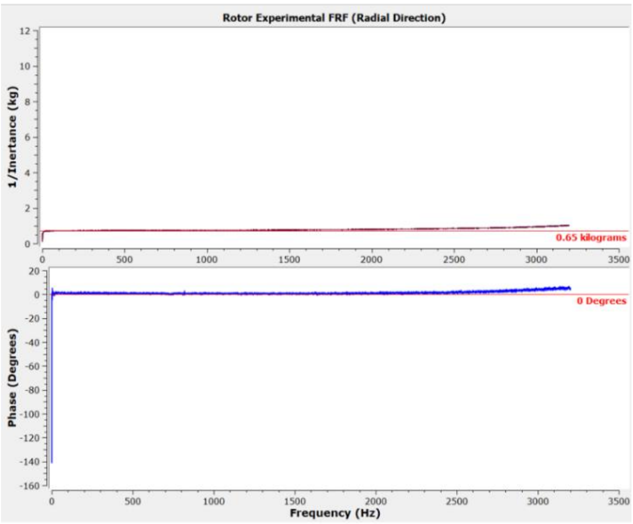

b)

Figure 3.7 : a) Vertically-suspended rotor and b) one of the FRF measurements using radial excitation.

Lastly, the assembly of the KT and KTA covers as well as the stator is used for FRF measurements. The covers and the stator are assembled by means of 4 screws. Figure 3.8 shows the suspended assembly. In the numerical models, this assembly group is modelled as a flexible system and the experimental data obtained here will be used in coming sections for the validation of this assembly model.

Figure 3.8 : Suspended assembly of the front and rear covers and the stator.

One of the measured FRFs of the assembly is plotted in Figure 3.9. It is seen that the first four natural frequencies of the elastic modes of the assembly are at 1306 Hz, 1997 Hz, 2667 Hz and 3180 Hz. The fourth mode at 3180 Hz is very close to the upper limit of the frequency range of interest (i.e., 3200 Hz), therefore it is not evident as much as the other three modes in the measured FRFs. It will be shown in validated numerical results in subsequent sections that there is indeed a mode at 3180 Hz.

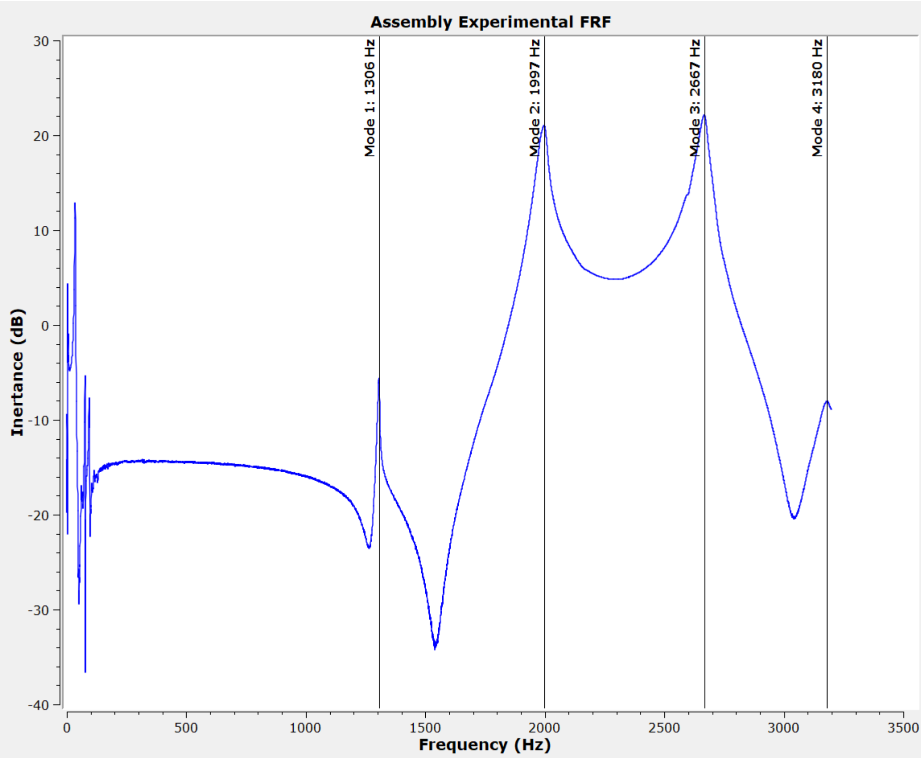

Figure 3.9 : Measured FRF of the assembly without rotor.

3.2 Campbell Diagram Measurements

Two fully-assembled motors are used as specimens for Campbell Diagram measurements. The first specimen, named S1, is an Atlas motor coupled with a flywheel whose equivalent moment of inertia is equal to the moment of inertia, with reference to the motor shaft, of a washing machine when the tumble is loaded with 5 kilograms of laundry. Two of the ball bearings used at two ends of the rotor shaft in S1 were healthy and new. The second specimen, named S2, is another Atlas motor coupled with the same flywheel. However, one of the ball bearings used in S2 had a damage on the outer ring, manually created by the bearing provider/manufacturer, ORS (Ortadoğu Rulman Sanayi A.Ş.), while the other bearing was healthy and new. An image of the manually-damaged outer ring is given in Figure 3.10. As can be seen in Figure 3.10, the damaged area is a narrow strip along the axial direction of the raceway, which is to ensure that individual balls have to roll over the damaged area under all possible contact angles. The average width of the damaged area is measured to be around 30 micrometres.

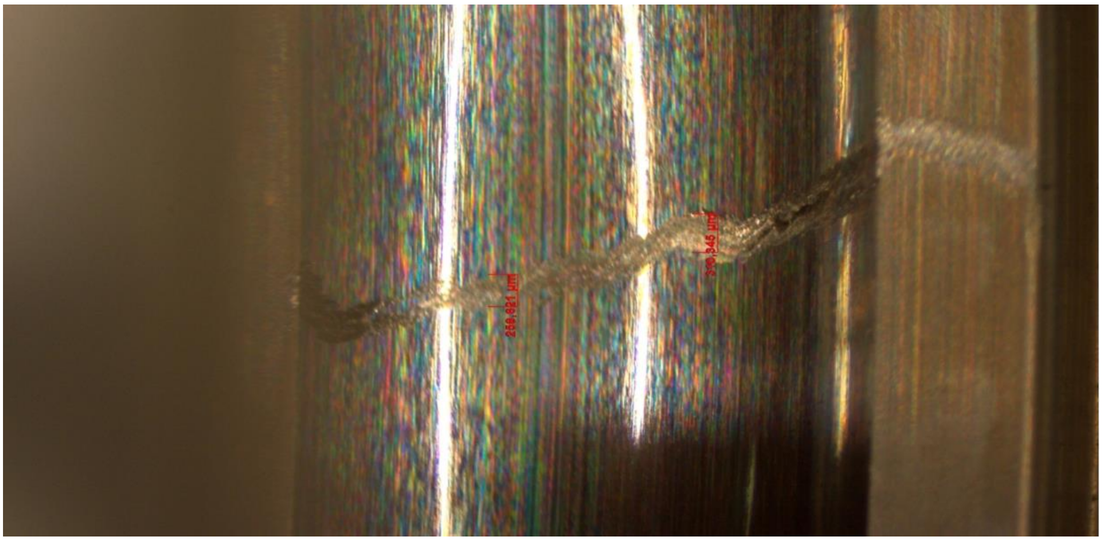

Figure 3.10 : Manually-created damage on the raceway of the outer ring used in one of the bearings of a test specimen.

Both specimens are suspended with very flexible strings again to simulate tests under free-free conditions. The specimens are placed inside a cage for safety considerations. A reflector band is stuck on the flywheel for the tachoprobe to sense the shaft speed and an accelerometer is placed on the stator to capture acceleration signals from the running specimens. The specimens are driven with a speed profile designed for a run-up test. The motor shaft speeds up from 0 RPM to 1000 RPM with a high acceleration of 100 RPM/second to allow for the motor to overcome inertial overhead, and then a constant acceleration of 5 RPM/second is maintained until the shaft speed reaches 10000 RPM. This acceleration profile allowed to capture meaningful data in 1000 - 10000 RPM range. Figure 3.11 shows the specimen S1. The laser light from the tachoprobe, the accelerometer and the suspension can also be seen in the same figure.

Figure 3.11 : One of the specimens used for Campbell Diagram measurements.

Measured Campbell diagrams for specimens S1 and S2 are presented in Figure 3.12a and Figure 3.12b, respectively. Natural frequencies of the system and the excitations caused by the shaft's rotation as well as its harmonics are clearly seen in Figure 3.12. Additionally, resonance regions of the running motors are visually detectable in the Campbell Diagrams in Figure 3.12. In both diagrams, it is seen that the characteristics of the resonance regions do not change significantly as the shaft speed is increased. Additionally, as expected, it is clearly seen that BPFO and its harmonics have higher amplitudes in the Campbell diagram of S2 than that of S1, due to the outer ring damage in the bearing of S2. Due to the increased amplitudes of BPFO harmonics, which excite the system at its natural frequencies as shown in Figure 3.12, increased amplitudes are observed around these natural frequencies in S2 compared to S1.

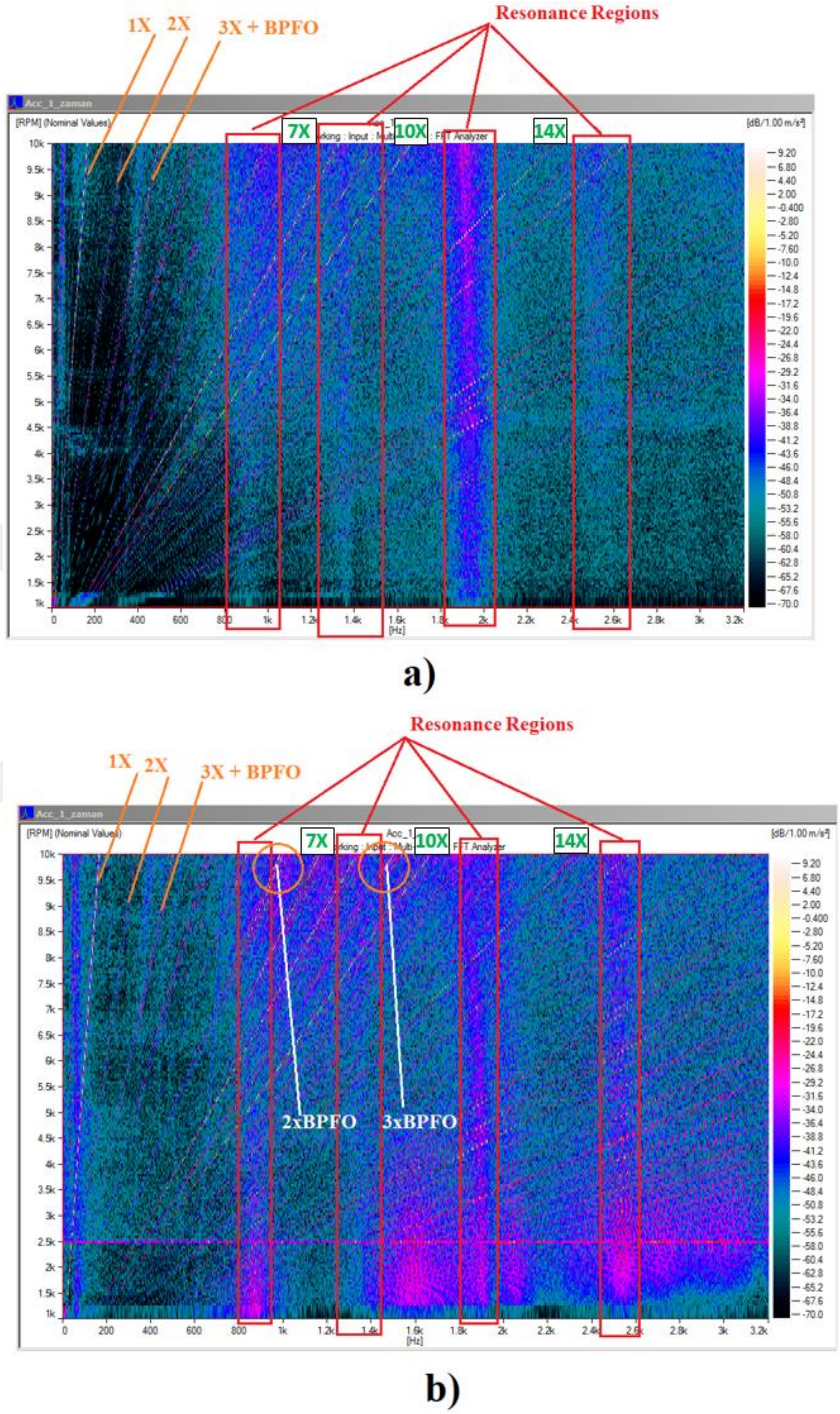

Figure 3.12 : Experimental Campbell diagrams for the specimens a) S1 and b) S2 (with damaged ball bearing).

Steady-state vibration measurements on S1 are made at the running speed of 10000 RPM and the measurement data is used for validation of the dynamic model under steady-state operations. The test setup used for acquiring experimental data to estimate the Campbell Diagrams is also used for steady-state vibration measurements. Frequency spectrum of the measured steady-state acceleration of S1 at 10000 RPM is given in Figure 3.13.

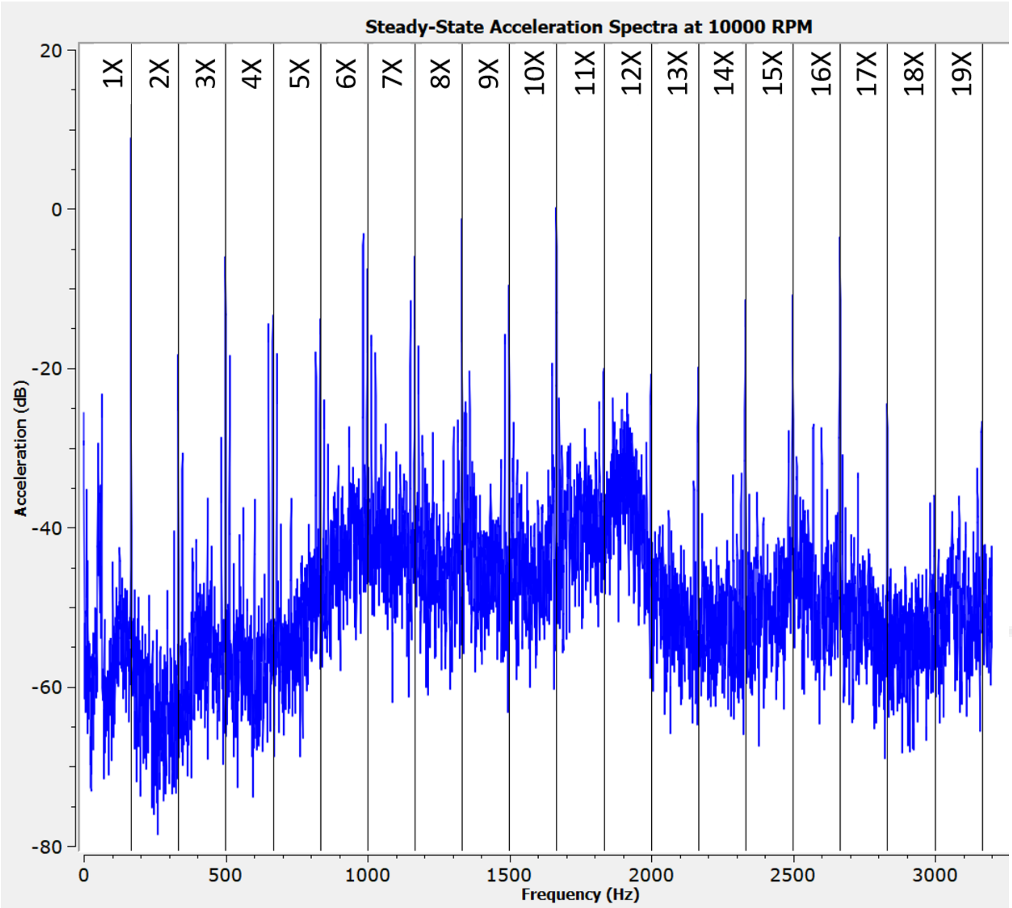

Figure 3.13 : Spectrum of the measured steady-state acceleration of loaded motor at 10000 RPM.

The first engine order, 1X, is nearly 166.5 Hz (~10000 RPM) and its higher orders (harmonics) are clearly visible in Figure 3.13. Furthermore, as also seen in the Campbell Diagram of S1 in Figure 3.12a, resonance regions of the loaded motor around 900 Hz, 1300 Hz, 1900 Hz and 2500 Hz are excited by the higher harmonics of engine orders; resulting in higher vibration amplitudes in these resonance situations. It is also seen that there are sidebands around 1X and its harmonics. When 7X is examined for example, it is seen that there is a pair of sidebands around the 7X frequency peak and the sideband gap is nearly 15 Hz, as shown in Figure 3.14.

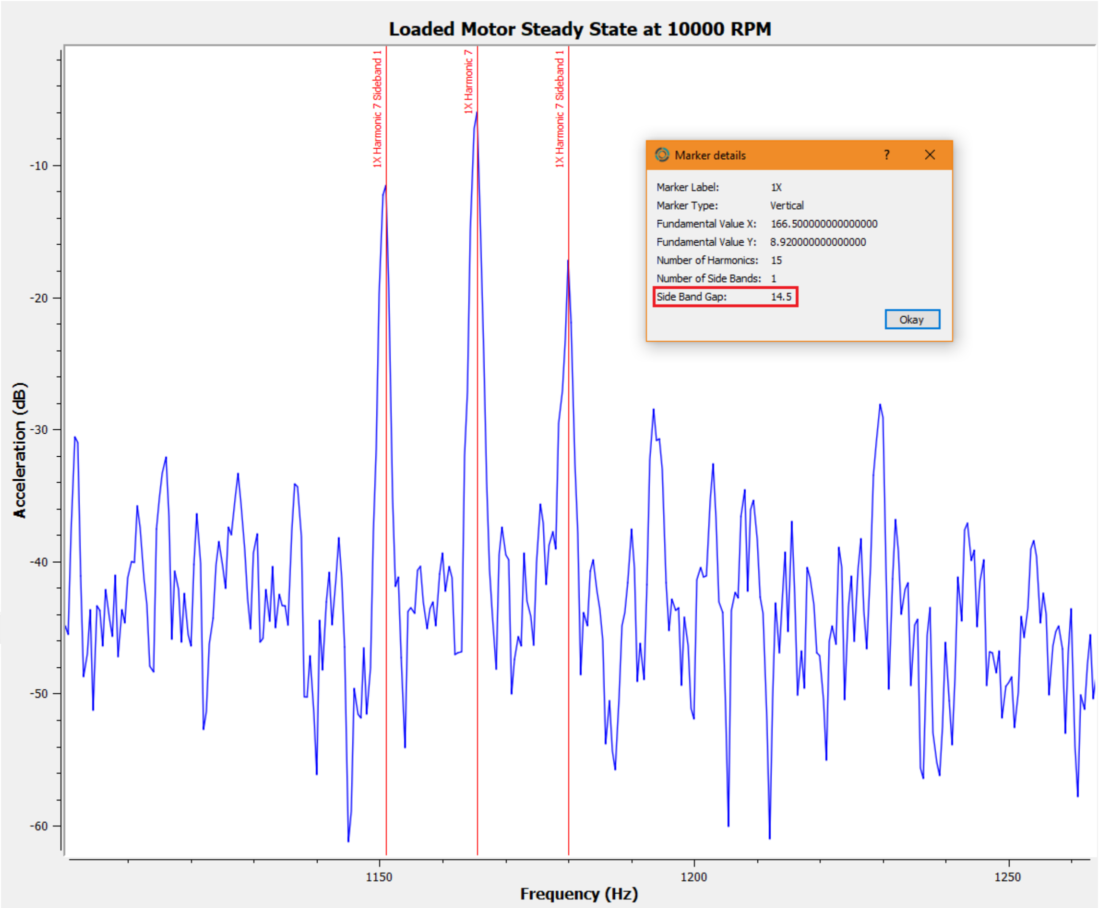

Figure 3.14 : Sidebands around the 7X frequency with a gap of nearly 15 Hz.

In order to confirm that there is in fact only a single pair of sidebands around engine orders, the number of sideband markers are increased in the data analysis software and it is seen that no other pair of sidebands coincide with frequency peaks except for the first pair, as shown in Figure 3.15. In later sections, it will be shown that the frequencies of the sidebands are determined by the contact angle and bearing clearance (in addition to the shaft speed). Thus, it is crucial to model the bearing clearance appropriately to get accurate simulations of the sidebands.

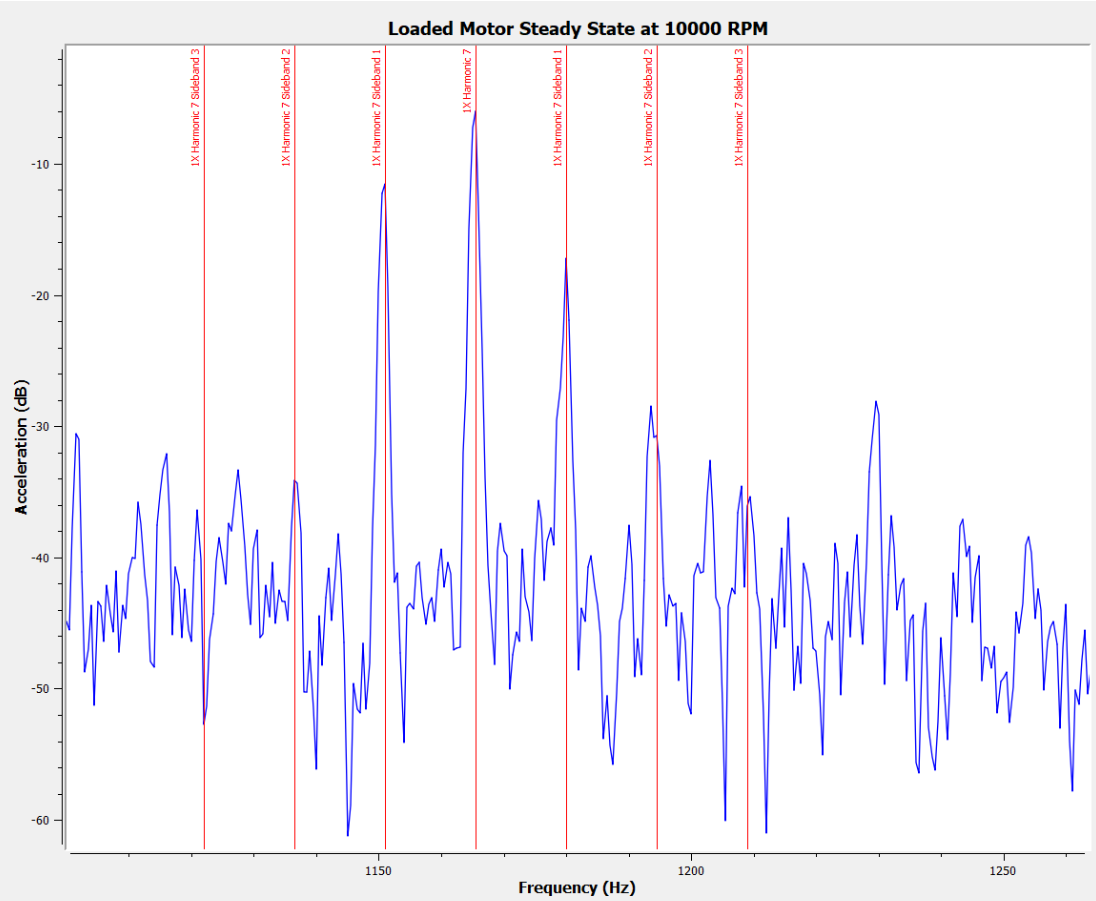

Figure 3.15 : Trial sideband markers for identification of the number of sideband pairs around the 7X frequency.

4. NUMERICAL MODELLING AND SIMULATIONS

In this chapter, numerical modelling of the Atlas motor is explained in detail. As it is crucial for numerical models to be validated by experimental results to achieve the desired accuracy, comparisons of the numerical and experimental results are also presented.

The motor model is divided into constituent submodels for simplicity of presentation and to examine all necessary details carefully. The submodels are grouped under two main groups; the rotary group and the non-rotary group, with regard to whether they belong to the rotating components of the motor or not.

4.1 The Rotary Group

The rotary group model consists of the following submodels: The bearing model, the rotor model and the flywheel model. These models are explained in detail in the following sections.

4.1.1 The bearing model

The bearing model is used to model the two bearings in the Atlas motor. The bearings are modelled as rigid components whose geometric data are imported directly from the 3D digital models provided by the manufacturer. However, the elasticity of the bearing components is included in the bearing model by means of contact stiffnesses defined for the contacts between the bearing components. The kinematic relationships in the bearing model are defined as shown in [25]. Briefly, all components of the bearings (i.e., the inner ring, the outer ring, the rolling elements and the cage structure) are modelled as rigid bodies as the individual components of the bearing have very high natural frequencies which are beyond the working frequency range [25]. The centres of mass of the components of the bearing are constrained to remain in the same plane with each other for the entirety of the simulations by means of planar joints. To model the cage structure as rigid, generalized constrains are applied to the individual balls to ensure that the distance between the centres of mass of the neighbouring balls remains unchanged as the inner ring rotates. Finally, dry (Coulomb) friction is enabled for the contacts in the bearing model. The static and dynamic coefficients of friction are taken as 0.23 and 0.16, respectively, as suggested in [25].

To reduce computational cost, instead of area contact, a line contact method is utilised to model the contacts as it was also used in [25], which will be referred to as the "previous model" within the rest of the thesis. The lines traced by the balls on the inner and the outer rings in the bearing model are referred to as contact circles which are illustrated in Figure 4.1 for one of the bearings. The bearing model presented in this study differs from the previous model in [25] in the way the radii of the contact circles are determined, which, as will be demonstrated later, offers a significant improvement over the previous model in terms of representing the sidebands in vibration spectra of the complete motor. As also briefly stated in Section 3.2, it is observed through numerical simulations that the frequencies of the sidebands are determined by the contact angle and the bearing clearance. The effects of the contact angle and bearing clearance on the frequencies of the sidebands are ignored in [25]. Although the details of this observation will be shared in later sections along with corresponding numerical results, it is found that the effects of the contact angle and bearing clearance are important parameters and should be taken into account to determine the radii of the appropriate contact circles.

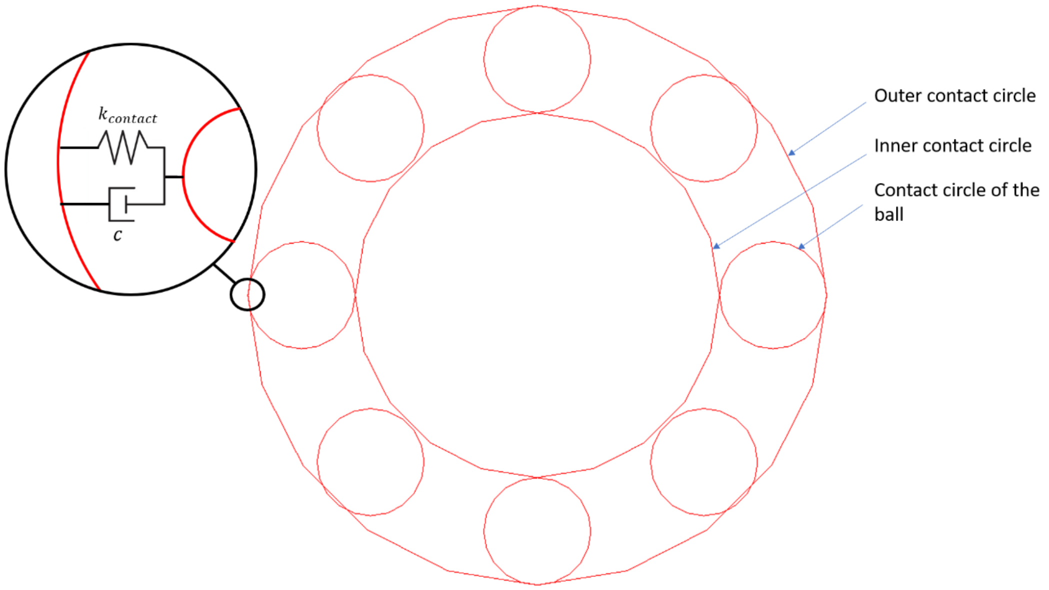

Figure 4.1 : The contact lines used to define the contacts in the bearing model. An example contact definition between lines is shown as a spring-damper pair.

The effect of the contact angle on the radii of the contact circles is depicted in Figure 4.2. As seen in Figure 4.2, firstly, the nominal radii (i.e., when the contact angle is zero radians) of the raceways and the balls are used to obtain the nominal radii of the contact circles. Subsequently, the line of contact between the rings and the ball is drawn by rotating the nominal radial axis by the amount of contact angle as denoted by α. Then, the intersection points between the line of contact and the inner and outer raceways, which are marked with green dots in Figure 4.2, are identified. The radial distance between the bearing axis and these intersection points are determined to be the actual contact radii to be used in the bearing model. The difference between the actual inner and outer contact radii is named contact effective ball diameter, which indicates the diameter of the contact curve used for the balls in the bearing model. Finally, the effect of the bearing clearance is included by enlarging the actual outer contact radius by an averaged value of the bearing clearance.

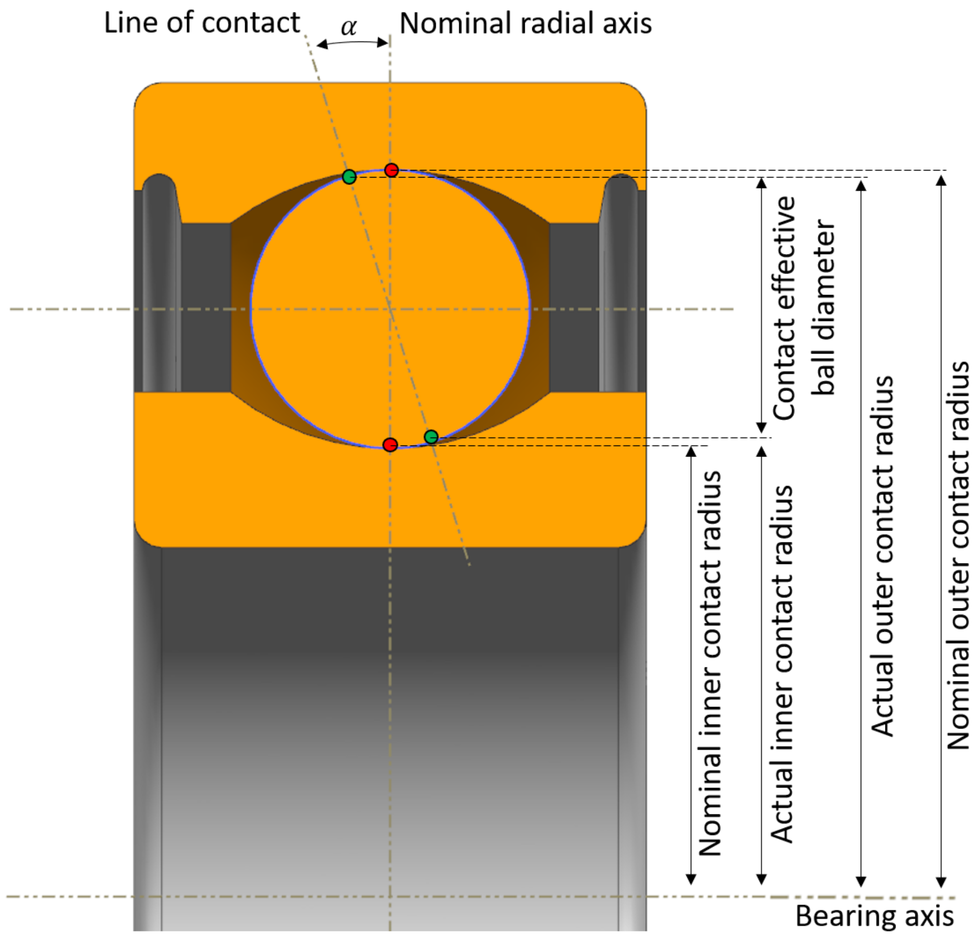

Figure 4.2 : The effect of the contact angle (α) on the radii of the contact circles.

As discussed previously in Section 2.2.3, the contact mechanism between the rolling elements and the rings is fundamental characteristic of ball bearings. The Hertzian contact theory is used in this thesis to model the mechanics of the contacts occurring between the balls and the rings. The mathematical relationships shown in Section 2.2.3 are used to calculate the contact stiffness of the SKF 6202 ball bearings which are used in the Atlas motor under investigation. The contact angle is taken to be 0.3 radians as given in [1]. An average value of the bearing clearance is estimated as 0.018 mm using the clearance range of the SKF 6202 given in [1]. The geometric and material properties used to calculate the inner and outer contact stiffnesses of the bearing model are given in Table 4.1. Using the mathematical procedures given in Section 2.2.3 with the numerical values presented in Table 4.1, the values of the inner and outer contact stiffnesses are calculated as $5.53\,x\,10^5\,N/mm^{3/2}$ and $5.94\,x\,10^5\,N/mm^{3/2}$, respectively. Figure 4.3 shows a fully-parametrised Hertzian-based non-linear contact definition used in the ball bearing model in MSC Adams. Finally, an isometric view of the bearing model is shown in Figure 4.4.

Table 4.1 : The geometric and material properties used for the calculation of the contact stiffnesses of the SKF 6202 bearing.

Property	Value	Unit
Groove radius of the inner ring	9.648	mm
Groove curvature radius of the inner ring	3.250	mm
Groove radius of the outer ring	15.648	mm
Groove curvature radius of the outer ring	3.250	mm
Ball radius	3.000	mm
Young’s Modulus of the rings and the balls (steel)	210000	MPa
Poisson’s Ratio of the rings and the balls (steel)	0.30	-

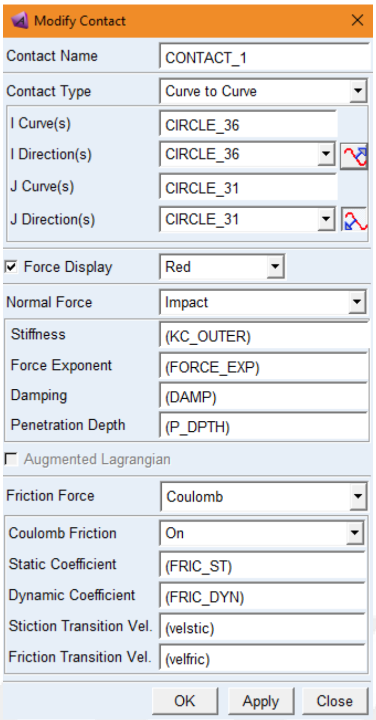

Figure 4.3 : An example of Hertzian-based non-linear contact definition used in the ball bearing model in MSC Adams.

Figure 4.4 : Isometric view of the bearing model for the SKF 6202 bearing.

4.1.2 The rotor model

The rotor model consists of the rigidbody models of the rotor, the magnets, the insulation sheets and the plastic cover to carry the magnets and the insulation sheets. It was shown in Figure 3.6 that the contribution of the isolated rotor's elastic modes to its vibration is negligible within 0 – 3200 Hz range. Thus, the rotor and its aforementioned components are modelled as rigid bodies in the complete motor model.

As stated in Section 3.1, the total mass of the complete rotor is 0.75 kilograms. Therefore, as also shown in Figure 4.5, it is validated that the mass of the rotor model is also around 0.75 kilograms.

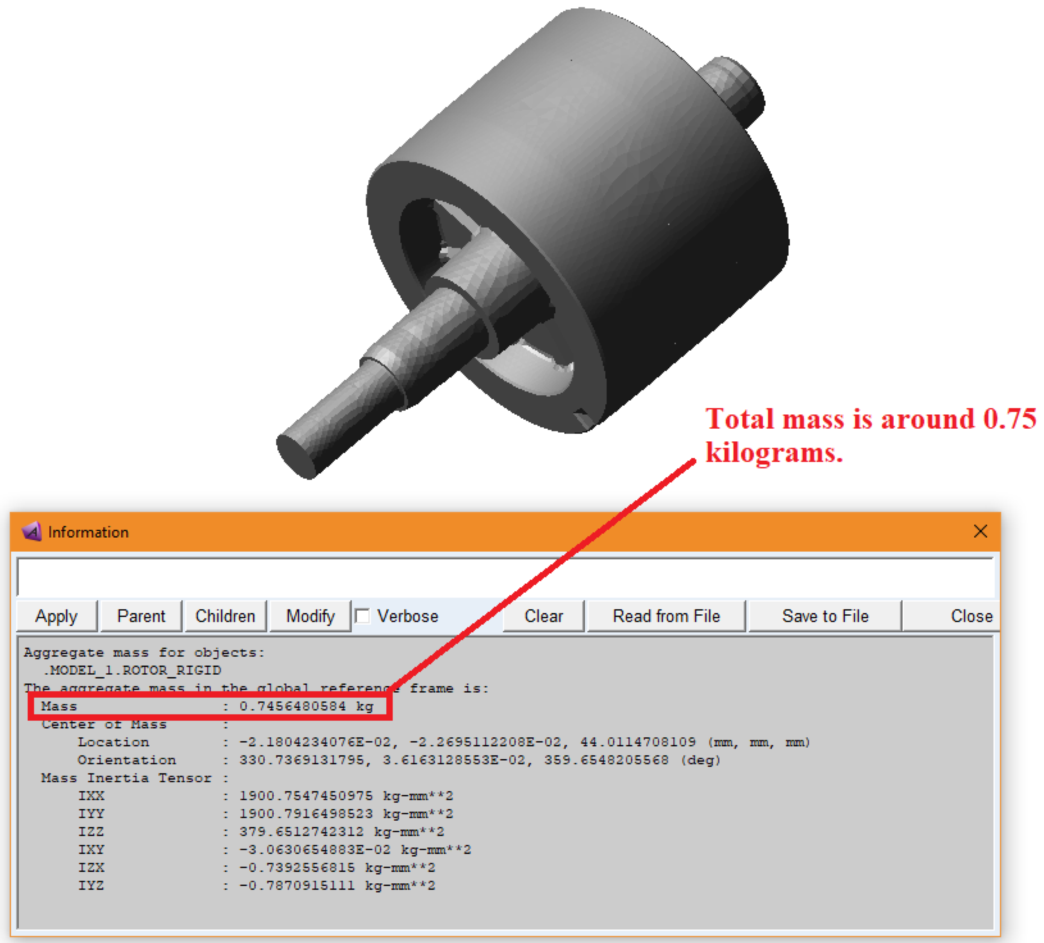

Figure 4.5 : The rigidbody model of the rotor.

4.1.3 The flywheel model

As explained in Section 3.2, a flywheel with an equivalent moment of inertia which is equal to the moment of inertia, with reference to the motor shaft, of a loaded washing machine tumble is used to apply load to the motor during its acceleration. To generate the rigidbody model of the flywheel, the exact dimensions of the flywheel is imported to the simulation environment. The mass and inertia of the flywheel model are validated against the test specimen. In addition, to account for the total unbalance in the motor, a small amount of unbalanced mass is added to the flywheel model near its outer diameter. The amount of the unbalanced mass is iteratively determined such that the amplitude of the first engine order in the numerically-obtained acceleration spectra is equal to that of the experimentally-obtained acceleration spectra. Isometric view of the flywheel model along with its mass and inertia information is depicted in Figure 4.6.

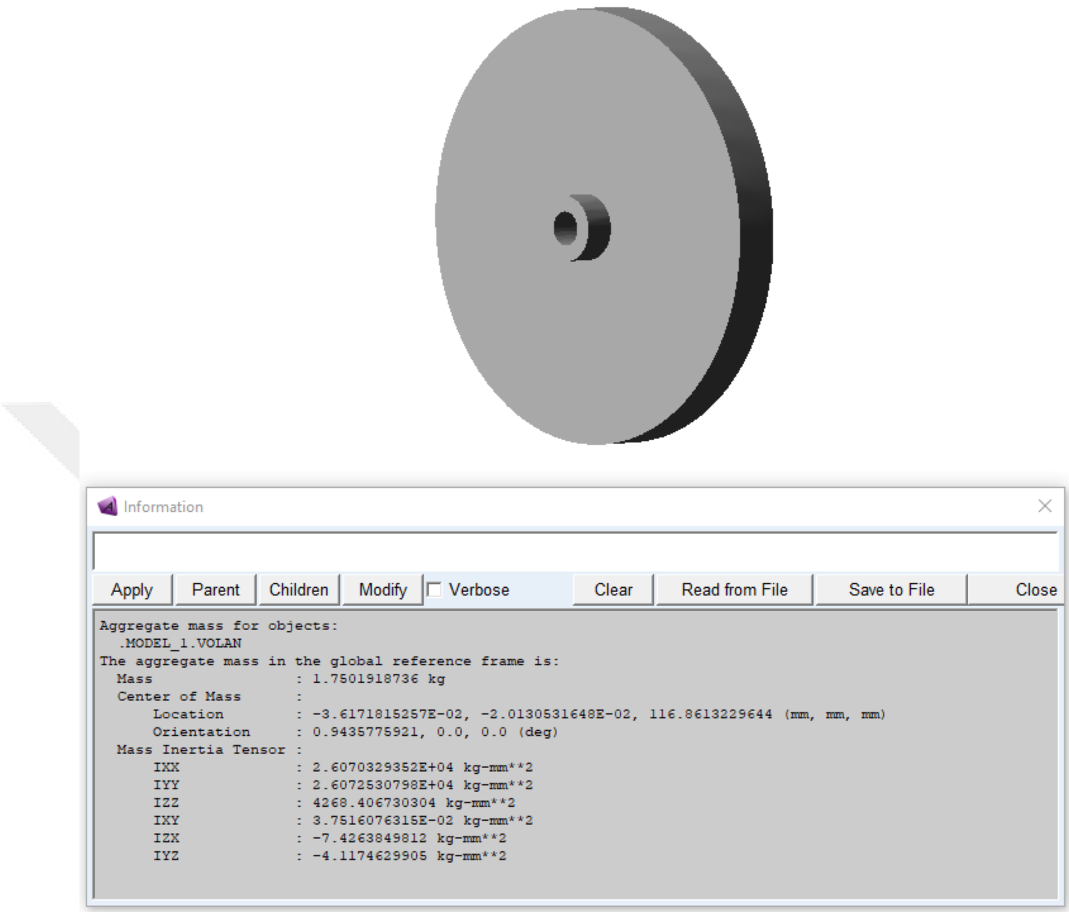

Figure 4.6 : The ridigbody model of the flywheel.

4.2 The Nonrotary Group

The nonrotary group consists of the flexbody models of the KT (front) cover, KTA (back) cover and the stator. As shown experimentally in Section 3.1, the elastic lower modes of these components contribute to the vibration of motor within 0 – 3200 Hz. Hence, flexbody models of these components are used instead of rigidbody models. Firstly, finite element models of the individual nonrotary components are generated and validated against the experimental results. Each of these nonrotary components is modelled using second order tetrahedrons (3D) in order to increase accuracy and prevent the artificial deformation which might be caused by using first order tetrahedrons (i.e., hourglass effect). Subsequently, the validated finite element models of individual parts are assembled to obtain the nonrotary assembly model, which is then converted to a flexbody model.

4.2.1 Finite element model of the KT cover

The CAD geometry of the KT cover is discretized using second order tetrahedrons. Prior to discretization, very small fillets and other surface inconsistencies within the CAD data of the KT cover are eliminated to allow for a consistent, high quality mesh. The finite element mesh generated for the KT cover is shown in Figure 4.7.

Figure 4.7 : The finite element mesh generated for the KT cover to be used for its flexbody model.

To validate the material properties and the modal properties of the finite element model of the KT cover, the total mass of the actual KT cover and the measured FRFs are used. Firstly, to validate the density, it is ensured that the total mass of the flexbody model matches the total mass of the actual KT cover, which is 0.350 kilograms. Secondly, to validate the Young's Modulus of the material and the mass and stiffness distributions of the model, the measured and numerically computed FRFs are compared. A comparison of the measured and numerically predicted FRFs of the KT cover is presented in Figure 4.8.

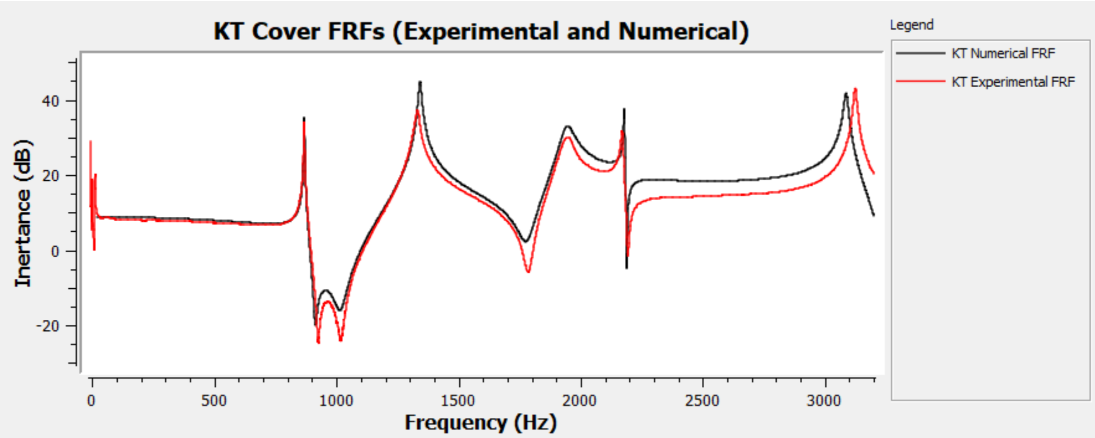

Figure 4.8 : A comparison of the numerical and experimental FRFs of the KT cover.

As seen in Figure 4.8, a very good correlation between the experimental and numerical FRFs is achieved. It should be noted that, though possible through adjusting the modal damping ratios, it is not necessary at this stage of modelling to try to match the amplitudes of the resonance peaks, as the finite element model of the KT cover will later be added to the flexbody model of the nonrotary assembly and the modal damping ratios of the flexbody model of the entire nonrotary assembly will be adjusted. Table 4.2 also presents the numerically computed natural frequencies and their respective errors.

Table 4.2 : Comparison table of the numerical and experimental natural frequencies of the KT cover.

Mode	Experimental (Hz)	Numerical (Hz)	Error (%)
1	872	872	0.00
2	1341	1345	0.30
3	1930	1948	0.39
4	2175	2180	0.23
5	3113	3087	0.84

4.2.2 Finite element model of the KTA cover

Similar to the KT cover, the finite element model of the KTA cover is generated and then validated using the mass information and the measured FRFs of the KTA cover. Firstly, the density of the material is validated by ensuring that the mass of the finite element model is equal to the mass of the actual KTA cover, which is 0.400 kilograms. The finite element mesh generated for the KTA cover is shown in Figure 4.9.

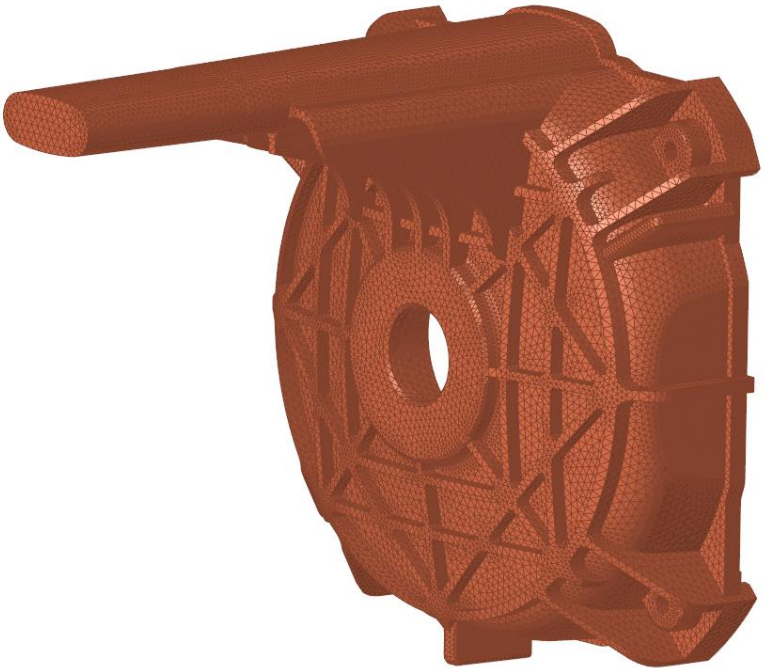

Figure 4.9 : The finite element mesh generated for the KTA cover to be used for its flexbody model.

Secondly, the measured and computed FRFs of the KTA cover are compared in order to validate the mass and stiffness distribution of the finite element model. A comparison of the numerical and experimental FRFs of the KTA cover is presented in Figure 4.10.

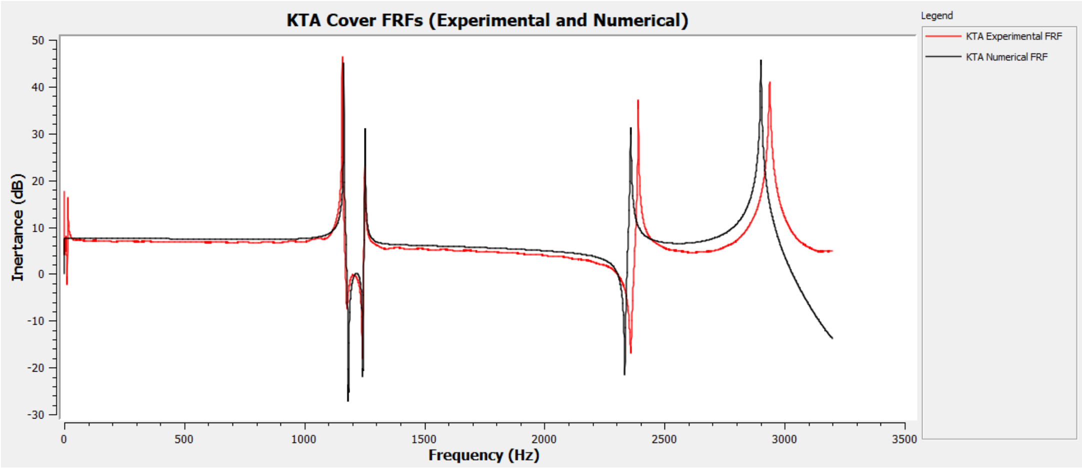

Figure 4.10 : A comparison of the numerical and experimental FRFs of the KTA cover.

As seen in Figure 4.10, a good correlation is achieved between the numerical and experimental FRFs of the KTA cover. Once again, it should be noted that matching the resonance peaks is not necessary at this stage of modelling as the modal damping ratios will be identified for the complete assembly of the flexbody later. The comparison table of the numerical and experimental natural frequencies along with the error between them are given in Table 4.3, where it is seen that good correlation is achieved in terms of natural frequencies between the numerical and experimental results.

Table 4.3 : Comparison table of the numerical and experimental natural frequencies of the KTA cover.

Mode	Experimental (Hz)	Numerical (Hz)	Error (%)
1	1157	1168	0.95
2	1252	1258	0.48
3	2390	2368	0.92
4	2938	2913	0.85

4.2.3 Finite element model of the stator

The stator is a significantly more complex structure to model than the KT and KTA covers as it comprises a plastic insulation, copper wires wrapped around the armatures and steel laminations which are connected to each other by surface friction and four small pins at each corner of the stator. A fine second order tetrahedral mesh is used to model the inertia and stiffness distribution of the actual stator.

A number of simplifying assumptions are made in order to create a linear model and to reduce the modelling and computation time. One of the simplifications made is that the laminations being separate is ignored and the stator is modelled as a unified, homogeneous volume of steel. Another simplification applied is that, instead of modelling the individual mass and stiffness of the plastic insulation and the copper windings, an equivalent mass and stiffness is used for the armatures. This is done by assigning a separate material to the armatures in the finite element model, whose density is determined by ensuring that the total mass of the stator model is equal to the total mass of the actual stator. The finite element model of the stator is shown in Figure 4.11 where the purple colour indicates the armature material and the orange colour indicates steel.

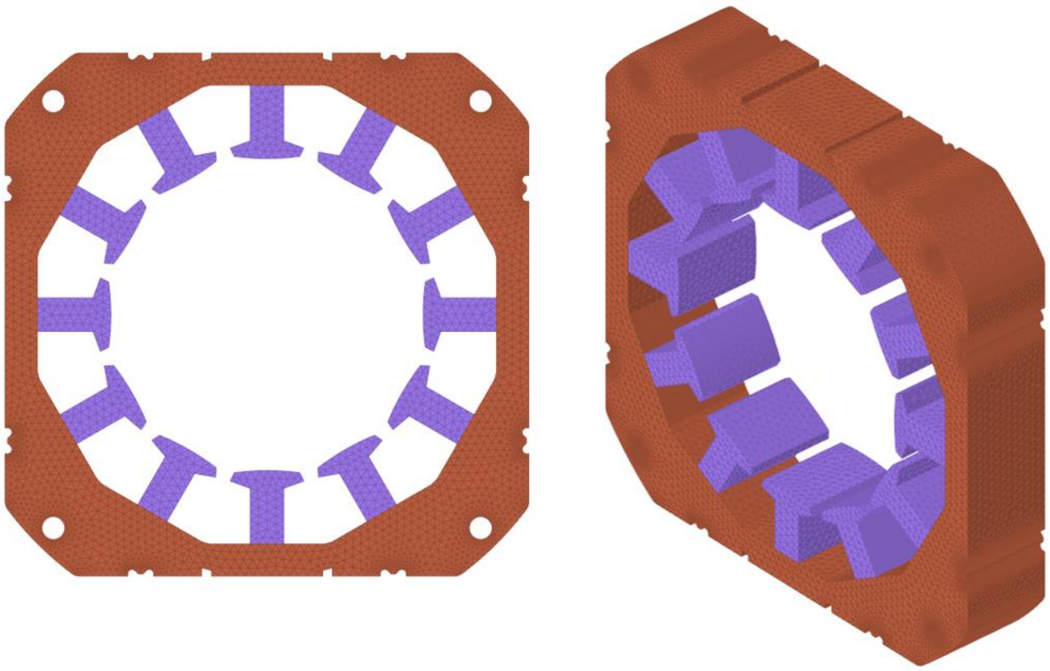

Figure 4.11 : The finite element model of the stator. Purple indicates the armature material that estimates equivalent mass and stiffness for the armatures. Orange indicates steel.

The Young's Modulus of the armatures' material is determined iteratively by comparing the numerical and experimental FRFs and natural frequencies. Firstly, a numerical model analysis of the stator is conducted and the numerically-calculated natural frequencies are compared with the experimental ones which are given previously. A comparison table of the numerical and experimental natural frequencies is given in Table 4.4.

Table 4.4 : Comparison table of the numerical and experimental natural frequencies of the stator.

Mode	Experimental (Hz)	Numerical (Hz)	Error (%)
1	986	978	0.81
2	1516	1493	1.51
3	-	1657	-
4	3133	3160	0.86

As seen in Table 4.4, good correlation between the numerical and experimental results is achieved. However, as also noted previously, the third mode is only visible in the numerical set and not in the experimental set. It is discussed previously that the third mode of the stator is an out-of-plane mode, which is difficult to measure due to the high friction between the laminations. To validate this statement, the third mode shape of the stator is visualized using the validated stator model, as depicted in Figure 4.12. As can be seen in Figure 4.12, the third mode of the stator is indeed an out-of-plane mode, which could not be measured, presumably due to the very high level of modal damping for this mode. However, as the rest of the numerical modes are validated by the experimental results, the third mode of the stator is also accepted as a validated mode in the numerical model.

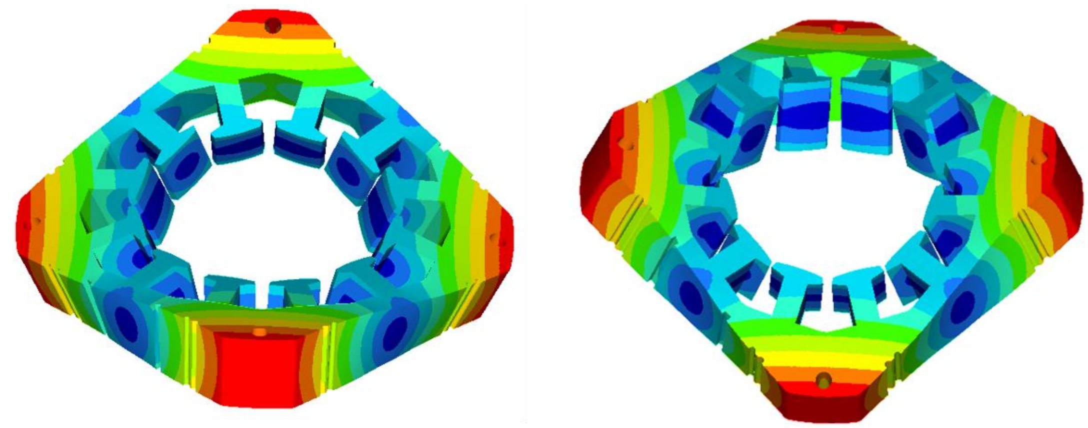

Figure 4.12 : The numerically-computed shape of the third mode of the stator, which is an out-of-plane mode with respect to the measurement direction.

Finally, the numerical and experimental FRFs of the stator are compared. An overlay plot of the numerical and experimental FRFs of the stator is given in Figure 4.13. It is seen in that good correlation is achieved between the numerical and the experimental FRFs. It should be stated that the effects of the third mode are suppressed in the numerical FRF by adding a very high amount of modal damping.

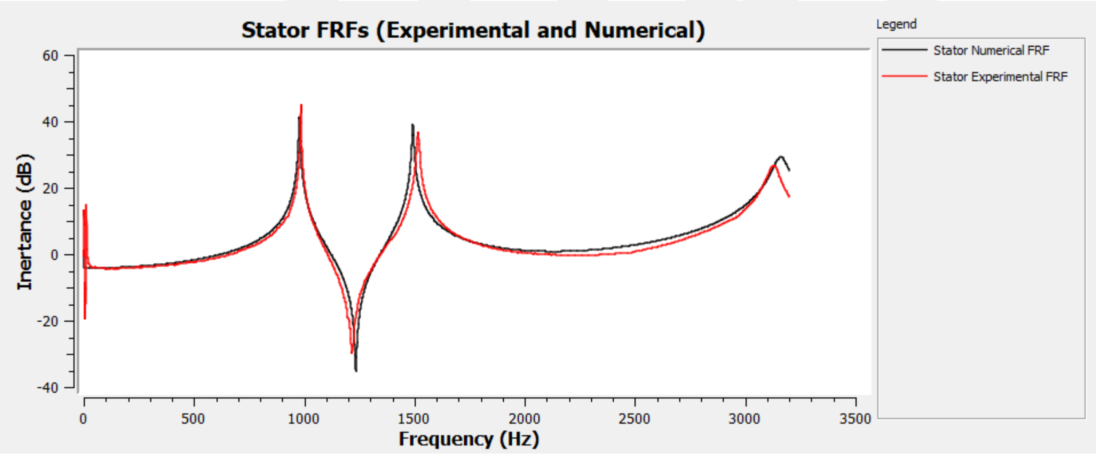

Figure 4.13 : A comparison of the numerical and experimental FRFs of the stator.

4.2.4 Finite element model of the nonrotary assembly

After the individually-validated models of the components of the nonrotary assembly (i.e., the KT cover, the KTA cover and the stator) are generated, they are assembled to obtain the finite element model of the nonrotary assembly. The nonrotary components of the Atlas motor are assembled with the use of four screws which are placed at the corners of the KT and KTA covers. In reality, the nonrotary assembly exhibits nonlinearities at the interfaces where the surfaces of the stator and the covers are contacting under the pressure applied by the screws. To simplify the assembly model, these nonlinearities are neglected and the contact interfaces are instead modelled with node connectivity, where, the nodes at the interfaces of the nonrotary components are shared by the interfacing elements. Additionally, the screws are modelled as beam elements to further simplify the model and to reduce computation time. The pretension of the screws is neglected. A view of the finite element of the nonrotary assembly is presented in Figure 4.14. As seen in Figure 4.14, the screw holes of the covers are connected to the beam element with rigid (RBE2) elements. The assembly model consists of 1.6 million second order tetrahedrons and 2.6 million nodes.

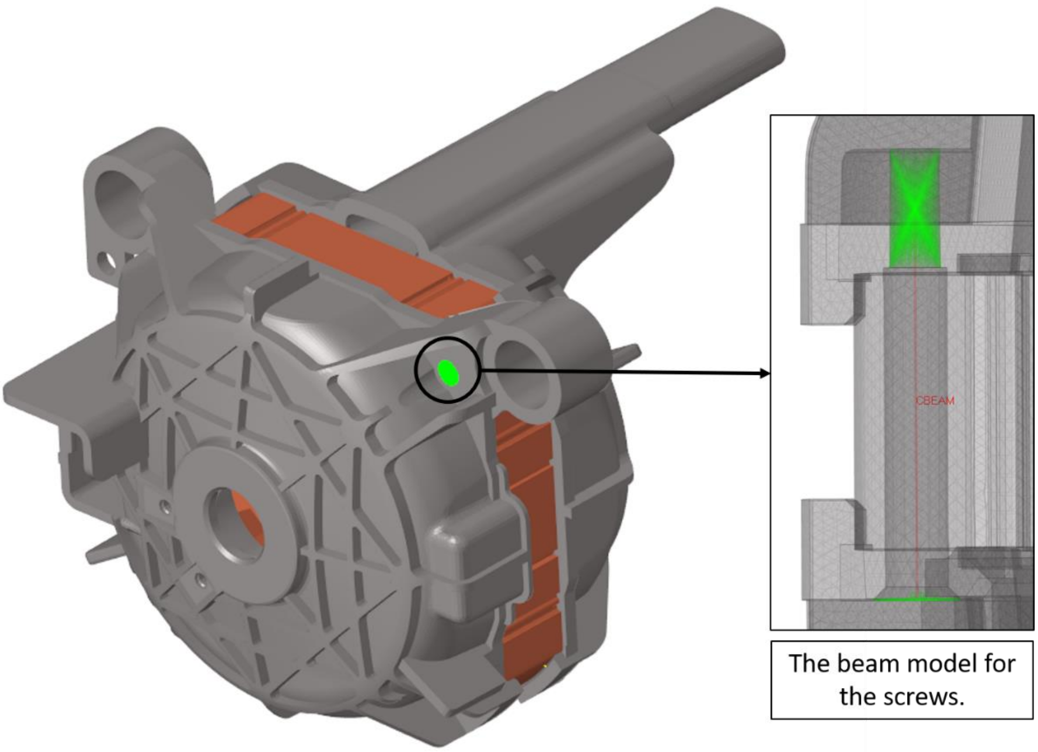

Figure 4.14 : The finite element model of the nonrotary assembly. The beam model without pretension is used to model the screws to reduce the computation time.

A numerical modal analysis of the finite element model of the nonrotary assembly is conducted to calculate the natural frequencies of the assembly and the obtained numerical results are compared with the experimental results which are previously given. The comparison of the numerical and the experimental results is given in Table 4.5. It is seen that a good correlation, with less than 5 percent error, is achieved for all of the natural frequencies.

Table 4.5 : Comparison table of the numerical and experimental natural frequencies of the nonrotary assembly.

Mode	Experimental (Hz)	Numerical (Hz)	Error (%)
1	1306	1260	3.52
2	1997	2091	4.71
3	2667	2616	1.91
4	3180	3051	4.06

The numerical and experimental FRFs are compared for validation purposes as shown in Figure 4.15. As seen, although the numerical FRF reflects the general trend of the experimental FRF, the correlation is low as the nonlinear contacts between the stator laminations as well as the contacts between the front and back covers and the stator are neglected in the nonrotary assembly model.

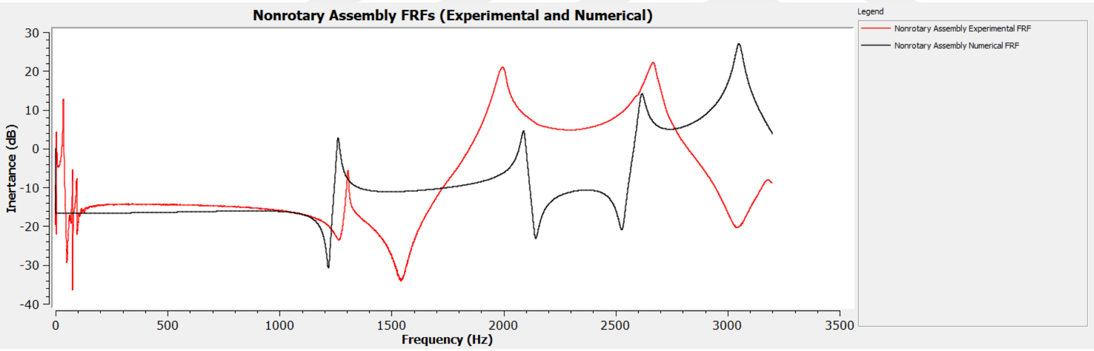

Figure 4.15 : A comparison of the numerical and experimental FRFs of the nonrotary assembly.

4.3 The Multibody Dynamic Model of the Atlas Motor

The flexible-body (flexbody) models of the rotary and the nonrotary groups are assembled by means of appropriate kinematic relationships defined in the widely-known multibody dynamic system modelling software MSC Adams. Firstly, the inner rings of the ball bearings and the flywheel are assembled to the flexbody model of the shaft of the rotary group. The assembly process here is achieved by applying fixed joints between the bodies at the corresponding interface nodes of the shaft as shown in Figure 4.16. Similarly, the outer rings of both bearings are fixed to the flexbody model of the nonrotary group by applying fixed joints (i.e., the joint that allows no relative translation or rotation between the bodies) at the corresponding interface nodes of the nonrotary group.

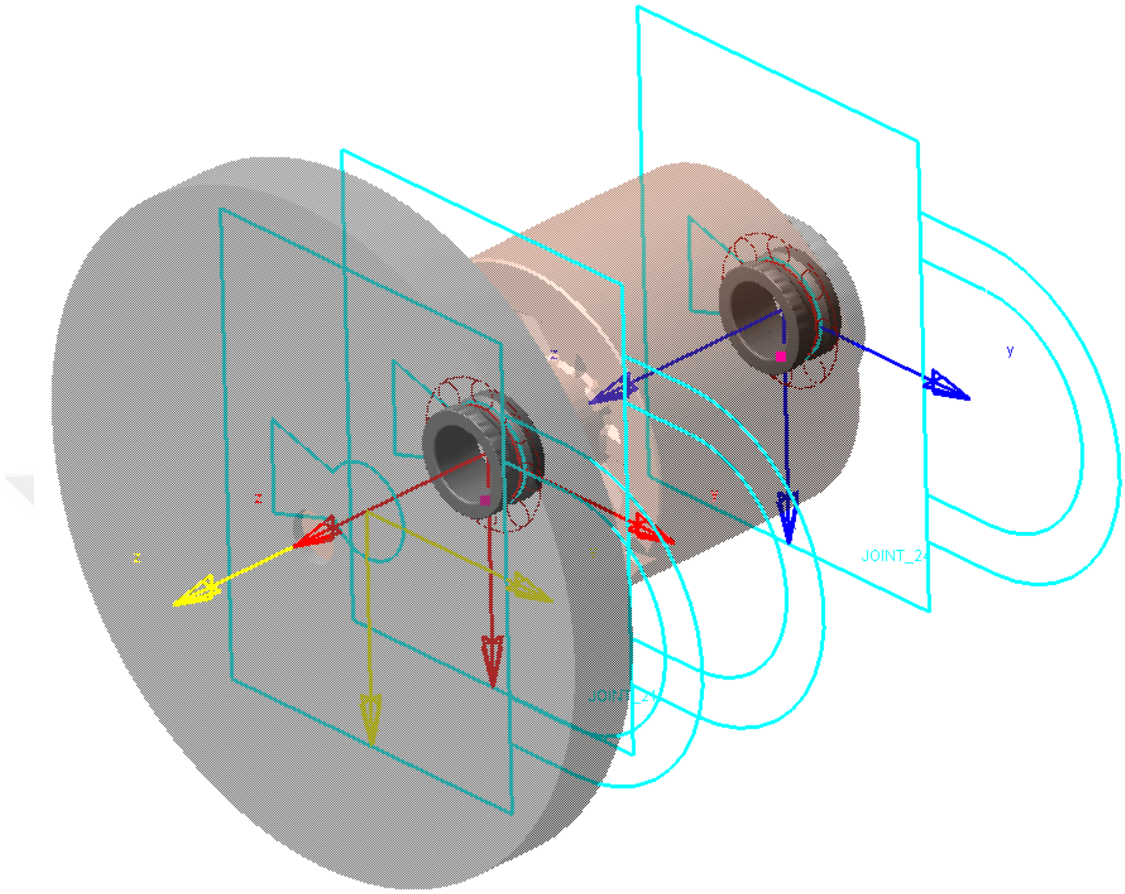

Figure 4.16 : The flywheel, the inner rings of the bearings and the shaft as they are coupled at the corresponding interface nodes of the shaft (yellow, red and blue markers).

At this point, a complete multibody dynamic assembly of the Atlas motor is obtained. To model the suspension used in the tests (see Section 3), one-directional linear spring elements are used with a small amount of damping applied in order to prevent any perpetual oscillations of the assembly on suspension springs. Though accurate modelling of the suspension is not necessary as the numerical vibration data are extracted from the steady-state conditions, an appropriate value is selected as the spring constant for the suspension springs to ensure that the natural frequency of the suspension is less than 10 percent of the first natural frequency of the system. The isometric view of the assembled multibody dynamic model of the Atlas motor is shown in Figure 4.17.

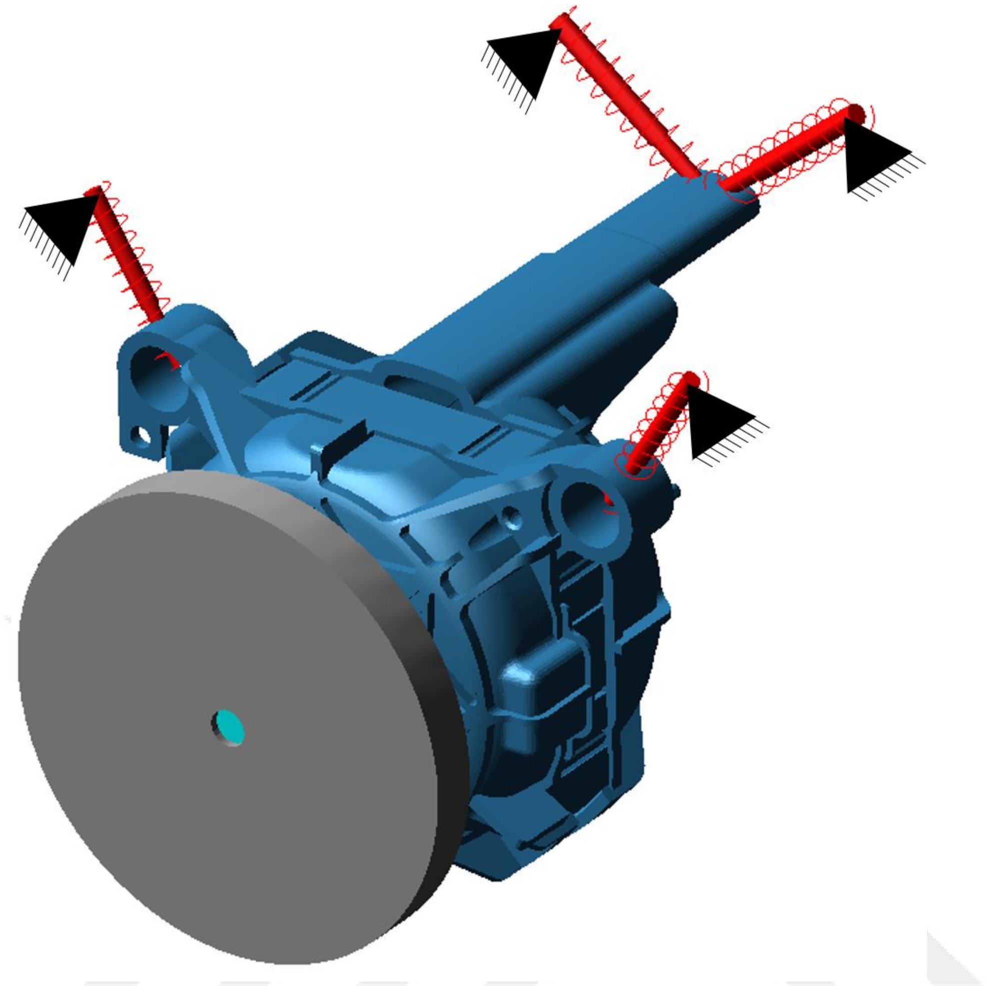

Figure 4.17 : The isometric view of the assembled multibody dynamic model of the Atlas motor. The black triangles indicate ground connection, red elements represent suspension springs in the test rig.

4.3.1 Modelling the electromagnetic excitations in the Atlas motor

As shown in [32], electromagnetic excitations have substantial effects on the vibration of BLDC motors. Therefore, it is important to somehow include (approximate) the electromagnetic excitations to obtained the desired accuracy from multibody dynamic simulations of BLDC motors. As the number of the poles and the slots determines the electromagnetic excitation frequencies, it is important to note that the Atlas motor has 12 slots and 8 poles. As previously stated and demonstrated in [32], the three sources of electromagnetic excitation in the motor and their corresponding frequencies are:

- The cogging torque frequency: the lowest common multiple of 12 and 8 times 1X and its higher harmonics = 24X, 48X, 72X etc.
- Mutual and reluctance torque ripples: 6X and its higher harmonics = 6X, 12X, 18X etc.

- Radial active force fluctuations: 8X and its higher harmonics = 8X, 16X, 24X etc.

Firstly, as seen in Figure 3.13, the frequency range of interest in this research is confined to (0 – 3200 Hz) which covers the first 19 harmonics of the first engine order. Thus, the contribution of the cogging torque to the vibration of the motor can be neglected as the lowest harmonic of cogging torque (24X) is beyond the frequency range of interest. Similarly, for the mutual and reluctance torque ripples, only the first three harmonics (6X, 12X, 18X) are included in the electromagnetic excitation model. Lastly, for the radial active force fluctuations, only the first two harmonics (8X, 16X) are included. These individual harmonic excitations with electromagnetic origin are assigned a random phase using the INVPSD functionality provided in MSC Adams. The amplitudes of these harmonics are iteratively determined by comparing the overall steady-state amplitudes of the measured and predicted acceleration spectra at 10000 RPM. To reduce the modelling and computation time, only the stator is subjected to electromagnetic excitation, not the rotor. The electromagnetic excitation forces are applied to the armatures of the stator through the interface nodes previously defined at the centre of each armature.

4.3.2 Defining the motion and numerical integrator settings

The motion in the multibody dynamic simulations of the Atlas motor is defined by applying a constant angular velocity constraint on the inner ring of the KTA bearing with respect to the ground in MSC Adams. The value of the angular velocities used in the simulations are selected as the rotational speed of the shaft in the tests which is extracted from the corresponding measured spectra. To get a smooth acceleration which typically helps reduce the simulation time, a step function is used to apply the motion. The motor on suspension springs is let fall free under the action of gravity for the first 0.5 seconds to neutralize the initial oscillations. Subsequently, the rotor is accelerated to its terminal speed in the next 0.5 seconds. As MSC Adams accepts angular velocities in degrees per second by default, the corresponding angular velocities are entered in default units as shown in Figure 4.18.

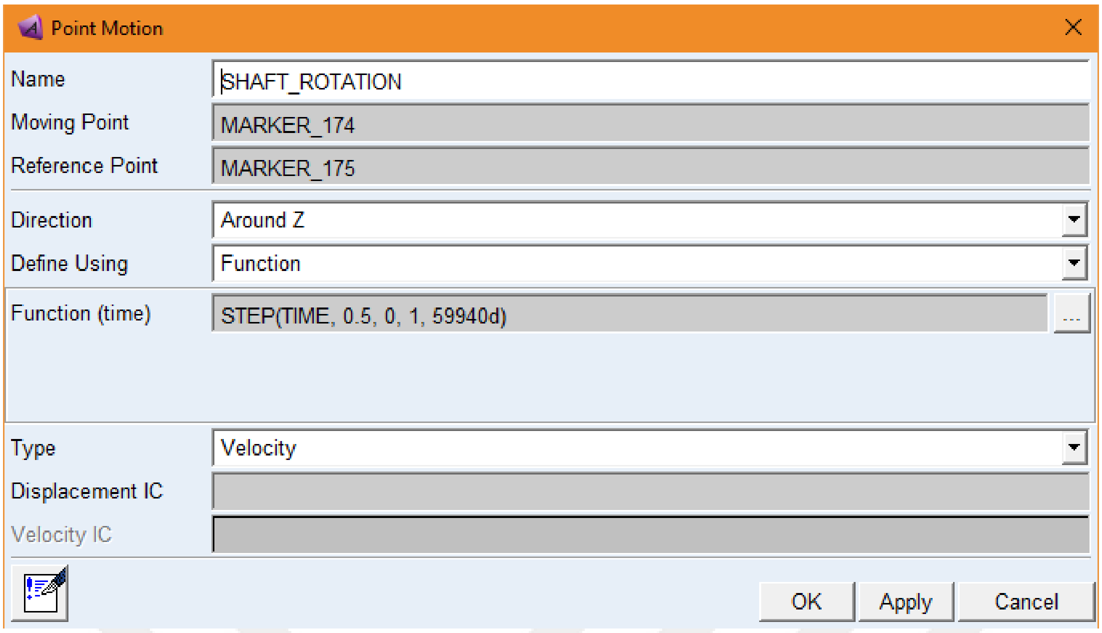

Figure 4.18 : Rotation of the shaft as defined in MSC Adams.

For the numerical integrator, MSC Adams' WSTIFF integrator is used with SI2 formulation as this combination gives the most accurate results for acceleration computations, as stated in the MSC Adams Documentation [36]. The integration tolerance (error) and maximum integration step are set to 10^{-4}.

5. COMPARISONS OF NUMERICAL AND EXPERIMENTAL RESULTS

In this section, the numerical results obtained from the steady-state simulations as well as the Campbell diagrams are compared with the experimental results presented in Section 3. The following three phenomena are considered in the comparisons: the harmonics of the 1X frequency, the sidebands around 1X and its harmonics, the resonance regions. The effects of the bearing model on the numerical steady-state results are also investigated here in order to obtain the most representative bearing model to be included in the numerical model. Finally, in the last section, the results of steady-state simulations of a motor model which includes a bearing model with an outer ring fault is given to demonstrate the ability of the model to predict the response of the system with the aforementioned fault.

5.1 The Effects of the Bearing Model on Predicted Steady-State Response of the Motor

In order to investigate the effects of the bearing model on the steady-state response of the motor model, three distinct bearing models are employed in the motor model and steady-state acceleration spectra are predicted from each model at 10000 RPM. The details of the three bearing models utilised for comparison purposes are given below along with their respective names.

- Model M1: The motor model with primitive joints to model the bearings. The KTA bearing is modelled as a primitive joint, which can be used to constrain translations and rotations independently in all three directions. The KT bearing is modelled as a customized primitive joint that constrains translations in the horizontal and vertical directions but allows for translation in the axial direction and rotations in all directions.
- Model M2: The motor model with linear bushings to model the bearings as linear springs in the horizontal and vertical directions. Equivalent spring constants of the ball bearings in the horizontal and vertical directions are taken

from [37] which uses the same kind of bearings (6202) as the ones in the Atlas motor, to represent the bearings' rigidity in these directions. In the other four directions (i.e., translation in the axial direction and rotation in all three directions), the bushings are given zero rigidity.

- Model M3: The motor model with the detailed bearing model (without the contact angle and bearing clearance effects) as previously introduced in Section 4.

The steady-state response predictions obtained from electric motor models using the bearing models M1, M2 and M3 are given in Figure 5.1 for 10000 RPM.

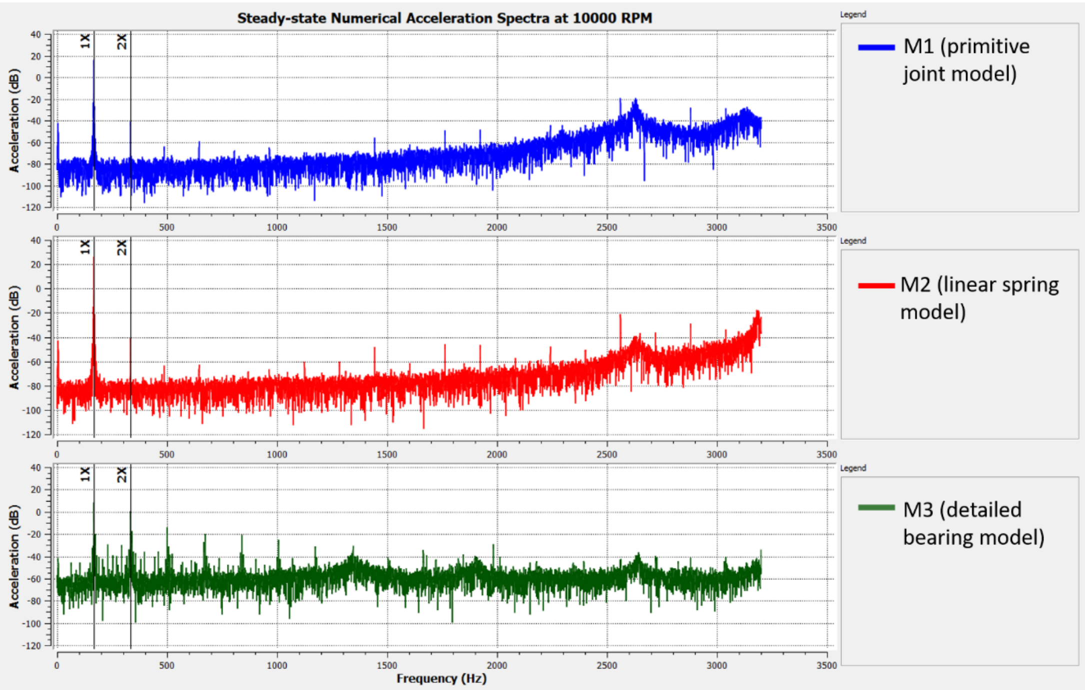

Figure 5.1 : Numerical acceleration spectra obtained from the models M1 (top), M2 (middle) and M3 (bottom) at steady-state conditions.

It is seen in Figure 5.1 that the amplitudes of the harmonics of 1X in the models M1 and M2 are significantly lower than those in the model M3, especially in the 0 – 2000 Hz range. This is obviously due to the absence of the nonlinear effects of the ball bearings in M1 and M2. A nonlinear response is caused by the ball bearings due to the nonlinear contact behaviour between the balls and the rings. This nonlinearity between the input (e.g., unbalanced loads, electromagnetic excitations etc.) and the response creates many harmonics of the frequency of the shaft rotation (i.e., 1X), as seen in the spectrum obtained from M3 in Figure 5.1. As both M1 and M2 models are linear models, the amplitudes of the harmonics of 1X are not predicted when these models are used. In addition, it is observed in Figure 5.1 that the resonance regions around 1300 Hz and 1900 Hz are not excited properly in the models M1 and M2. Therefore, modelling the nonlinear effects of the ball bearings in an electric motor model is crucial in order to effectively represent the response at the harmonics of 1X frequency and how resonance regions are excited by them.

It is also observed that the bearing model affects the prediction of the sidebands in the spectrum. As seen in Figure 5.2, sidebands are created around 1X by the bearings in the model M3 while no sidebands are created around 1X when other models (i.e., M1 and M2) are used. Therefore, it is concluded that the detailed nonlinear bearing model is necessary to predict the sideband vibrations in the motor model.

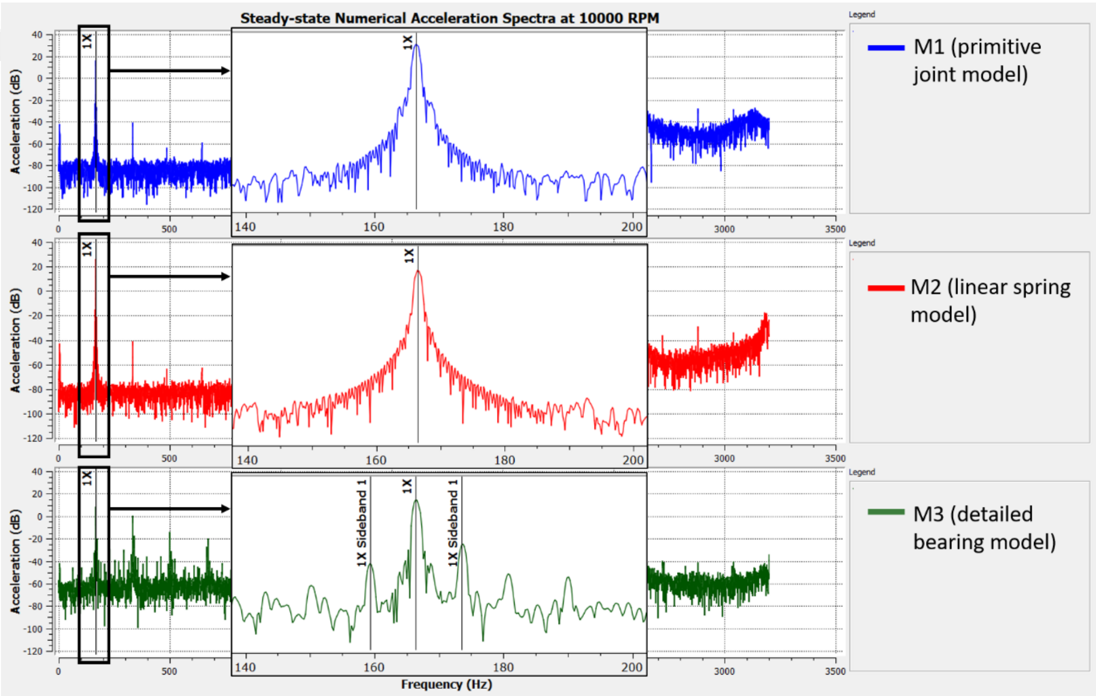

Figure 5.2 : Sidebands around 1X in the acceleration spectra obtained from the motor models M1, M2 and M3.

5.2 Comparison of the Experimental and Numerical Steady-State Response Levels

As demonstrated by the results given in Figure 5.1 and Figure 5.2, the model M3 is capable of predicting the harmonics of 1X, sidebands and the resonance regions on the forced vibration response of the Atlas motor, while the other two models (i.e., M1 and M2) are not. In the next step, the numerical steady-state acceleration spectrum obtained from M3 is compared with the experimental steady-state acceleration spectrum in terms of resonance regions, harmonics of 1X and sidebands at 10000 RPM. These spectra are graphed separately and important aspects are highlighted with the markers, as shown in Figure 5.3.

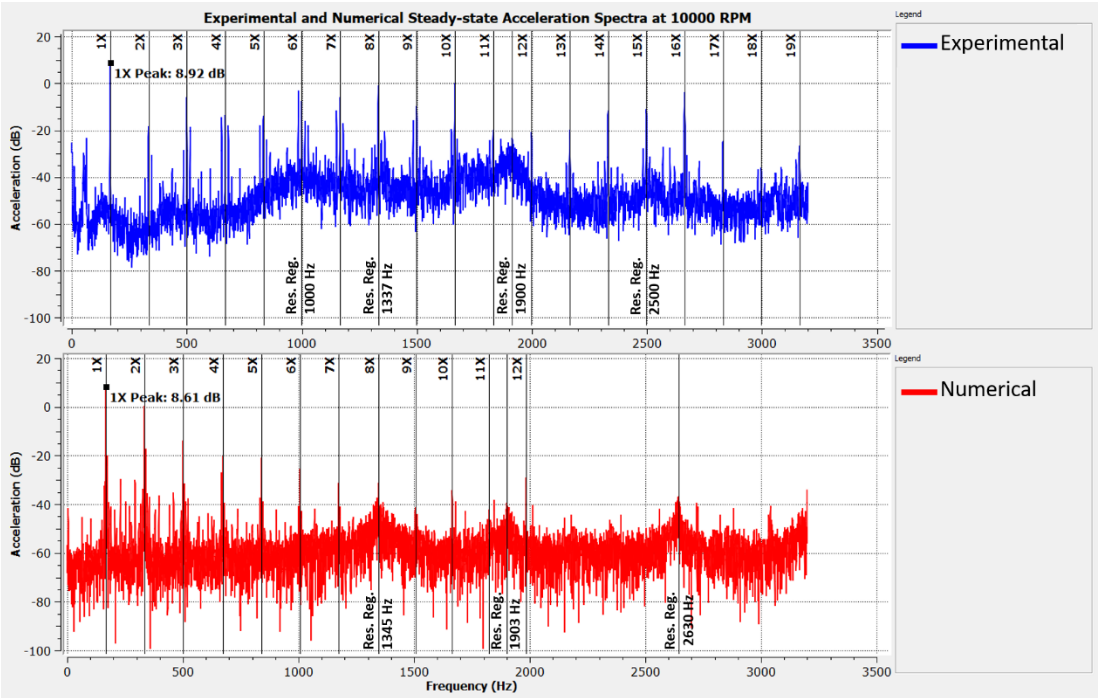

Figure 5.3 : Comparison of the numerical and the experimental steady-state acceleration spectra at 10000 RPM. Res. Reg. stands for resonance region.

Firstly, it is seen in Figure 5.3 that good correlation is achieved in terms of the amplitude of the 1X component between the numerical and the experimental results. The predicted amplitude of 1X is 8.61 decibels (dB) while the experimentally-obtained amplitude is 8.92 dB; which corresponds to an error of 3.48 percent with respect to the experimental results. It should be noted that the error between the two amplitudes can be further decreased by a slight increase in the unbalanced mass in the motor model. In this thesis, the iterations to find the correct amount of unbalanced mass are stopped once a satisfactory prediction of the amplitude of 1X is achieved.

Secondly, the resonance regions are compared between the numerical and the experimental results. The approximate frequencies of the resonance regions are marked as shown in Figure 5.3. As far as resonance regions are concerned, it is seen that good correlation is also achieved between the numerical and experimental results. However, it is worth stating that the first resonance region visible in the experimental results, which is around 900 Hz at lower RPMs and close to 1000 Hz at 10000 RPM as shown through measured Campbell Diagrams in Figure 3.12 and experimental steady-state spectrum in Figure 5.3, is not visible in the numerical results.

Lastly, the sidebands and the harmonics of 1X are compared between the numerical and the experimental results. It is seen in Figure 5.3 that the harmonics up to 12X are clearly visible in the numerical results while the harmonics higher than 12X are not recognisable. The sidebands around all visible harmonics in the numerical and experimental results given in Figure 5.3 are compared to investigate the correlation in terms of sideband frequencies. As an example, the sidebands around 2X are examined in Figure 5.4 which shows that the numerical model is not capable of predicting the sideband frequencies correctly when the geometric effects of the contact angle and bearing clearance are not included in the bearing model. The model without these effects predicts the sidebands with an error of 48 percent with respect to the experimental results.

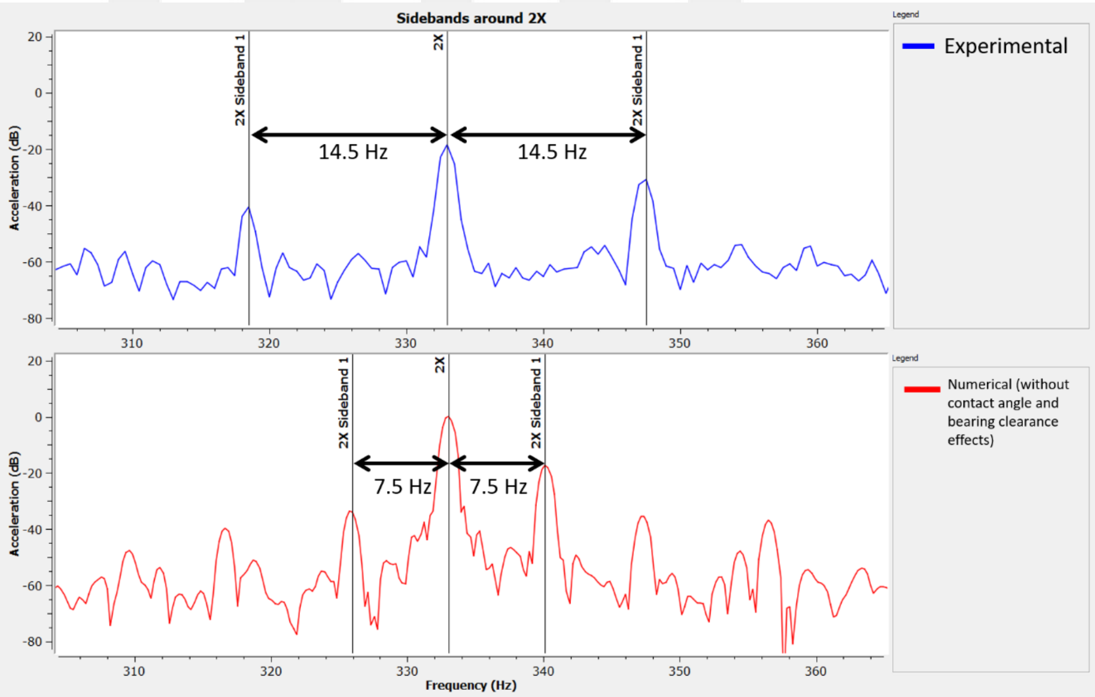

Figure 5.4 : Numerical and experimental sidebands around the second harmonic of the shaft speed at 10000 RPM.

As briefly discussed before in Section 3.2, it is important to include the effects of contact angle and bearing clearance in the bearing model to be able to predict the sideband frequencies with acceptable accuracy. To demonstrate the importance of accurately modelling the contact angle and bearing clearance effects, a motor model with a detailed bearing model including the geometric effects of the contact angle and bearing clearance as depicted in Figure 4.2 is utilised for additional steady-state simulations at 10000 RPM. Then, the results are compared with the experimental results. As shown in Figure 5.5, when the effects of contact angle and bearing clearance are included in the bearing model, the accuracy of the motor model in predicting the sideband frequencies significantly increases. The model with the updated bearing model predicts the sidebands with an error of about 3 percent with respect to the experimental results.

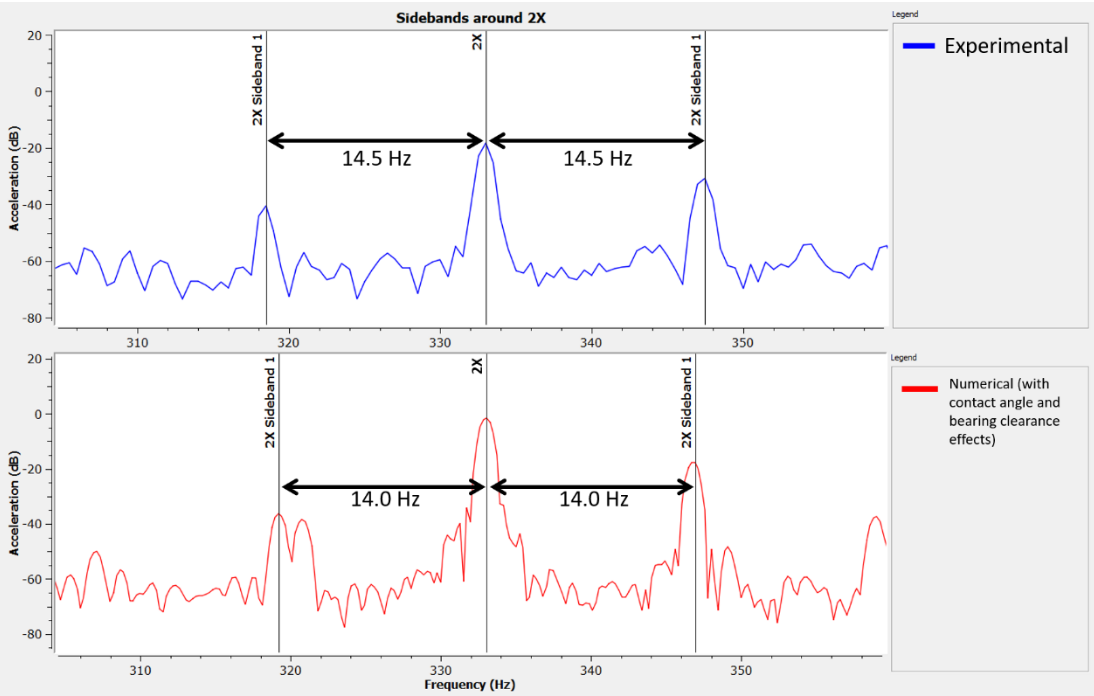

Figure 5.5 : Numerical and experimental sidebands around the second harmonic of the shaft speed at 10000 RPM.

5.3 Comparison of the Numerical and Experimental Campbell Diagrams and Overall Vibration Levels

It is demonstrated in Section 5.2 that, good correlation is achieved between the numerical and experimental results in terms of harmonics of 1X, sidebands and resonance regions at 10000 RPM. To observe the model's response in a wider frequency range, numerical Campbell diagrams are predicted.

As stated previously, in the Campbell Diagram measurement, the acceleration spectra were obtained with 50 RPM resolution between 1000 and 10000 RPM in a run-up test with 5 RPM/sec acceleration. Such a test takes nearly 35 minutes to complete. As it would be impractical to simulate a 35 minute long run-up test in MSC Adams due to

CPU and storage constraints, a series of steady-state simulations are conducted and numerical steady-state acceleration spectra are obtained from each of the simulations. After all of the spectra are obtained, a computer script is used for post-processing so as to obtain the numerical Campbell. The computer script reads the amplitudes in each spectrum and assigns a colour code based on the user-defined minimum and maximum amplitudes of the diagram.

As too many simulations would be required to create the numerical Campbell Diagram for 1000 – 10000 RPM, the RPM range is limited to 6500 – 10000 RPM to reduce the computational cost. This is a convenient range as all of the important phenomena (i.e., harmonics, sidebands, resonance regions) are clearly visible in this range. To further reduce the computational cost, the frequency range is limited to 0 – 2700 Hz range which is a convenient frequency range as there is no important information in the Campbell diagrams beyond 2700 Hz (see Figure 3.12).

Comparison of the experimental and the numerical Campbell diagrams of the Atlas motor is shown in Figure 5.6. Firstly, it is observed in Figure 5.6 that the harmonics of 1X are clearly visible up to 13X, which covers a frequency range between 0 – 2000 Hz. It was shown in the measured Campbell Diagrams that between 0 – 2700 Hz, the harmonics of 1X were visible up to 19X. Therefore, in terms of the harmonics of 1X, it can be concluded that the motor model gives satisfactory results between 0 – 2000 Hz range; however, improvements are needed to increase the visibility of the higher harmonics in 2000 – 2700 Hz range.

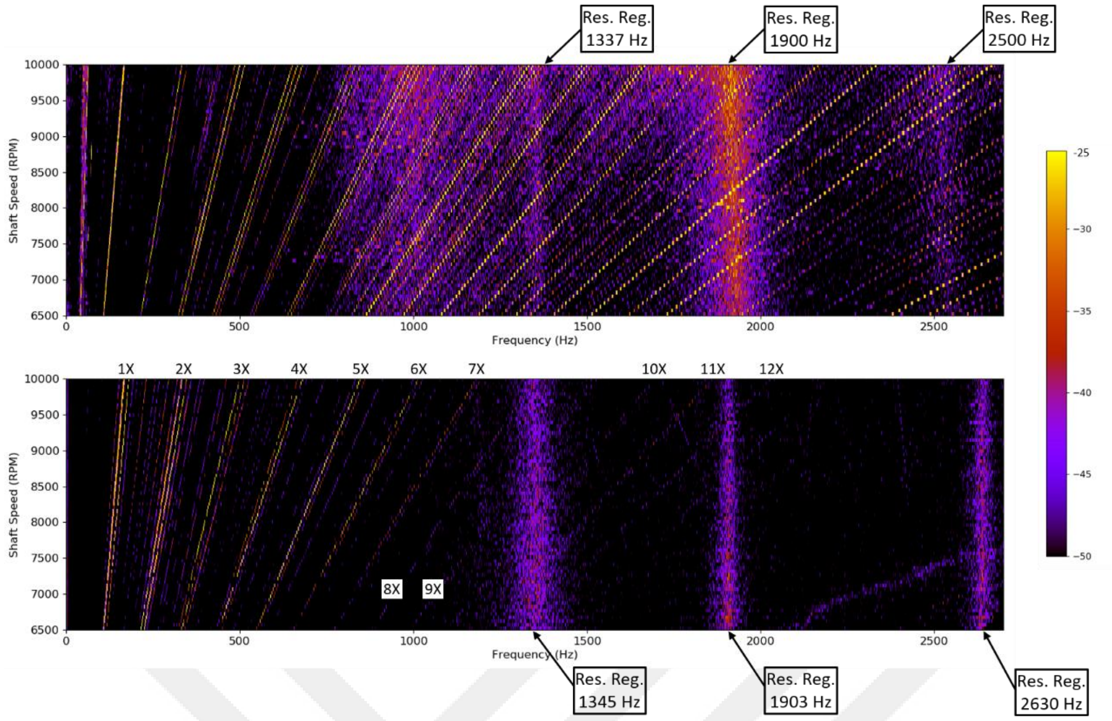

Figure 5.6 : Comparison of the experimental (top) and the numerical (bottom) Campbell diagrams of the Atlas motor. Res. Reg. stands for resonance region.

Secondly, it is seen in Figure 5.6 that the resonance regions at 1350 Hz, 1900 Hz and 2600 Hz are clearly predicted, which are in very good agreement with the experimental results given in Figure 3.12. However, it is also observed that the resonance region at 900 Hz is not visible in the numerical Campbell Diagram, which indicates the motor model's inability to represent that resonance region.

Overall vibration levels are compared between the experimental and the numerical results to further examine the correlation between the results between 6500 – 10000 RPM. Two different frequency ranges, 0 – 2000 Hz and 0 – 2700 Hz, are selected for the comparisons of overall vibrations as the numerical Campbell Diagram is particularly successful at predicting the harmonics of 1X, their sidebands and the resonance regions in 0 – 2000 Hz range. As seen in Figure 5.7, the correlation between the numerical and experimental overall vibrations is higher in 0 – 2000 Hz range than 0 – 2700 Hz range. Based on these results, it can be said that the motor model is able to produce satisfactory predictions in terms of overall vibration of the Atlas motor at higher shaft speeds, particularly above 8500 RPM. It is shown in Figure 5.7 that the correlation of the motor model in terms of overall vibration is especially high at 10000 RPM in both 0 – 2000 Hz and 0 – 2700 Hz ranges with ratios 0.82 and 0.78, respectively.

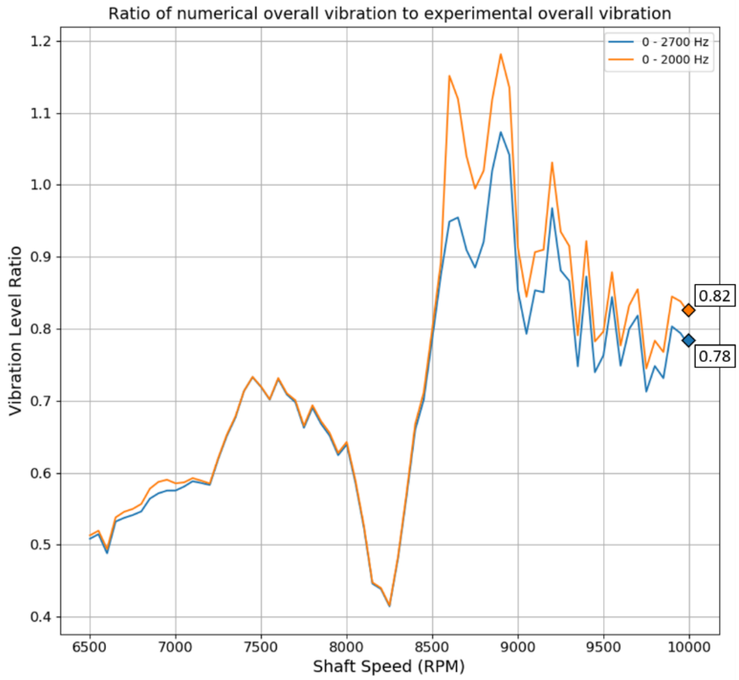

Figure 5.7 : Ratio of numerical overall vibration to experimental overall vibration calculated between 6500 – 10000 RPM for two different frequency ranges.

5.4 Simulations of Motor with a Faulty Ball Bearing

Additional steady-state simulations are conducted in order to demonstrate the ability of the multibody dynamic model developed here for predicting the response of the system when there is a fault in the ball bearing. In two separate motor models, two different faults are modelled on the outer ring contact circle of the KT bearing in the form of small bumps with 0.001 mm and 0.002 mm height to examine the effects of the intensity of the fault on the numerical results. The predicted results are examined in terms of the frequency and the amplitude of the BPFO as well as its harmonics.

A comparison of the results obtained from the motor models including bearing models with no fault, 0.001 mm fault and 0.002 mm fault is given in Figure 5.8. The analytical relationship given in equation 2.9 is used with the geometric values in Table 4.1 along with the contact angle 0.2 radians and the BPFO is calculated as 511 Hz. As seen in Figure 5.8, the BPFO is observed at 513 Hz and its amplitudes increase as the level of the fault increases. The small difference between the analytical and numerical BPFOs is due to the fact that the geometric dimensions of the ball bearing occurring after the addition of the contact angle were projected onto the bearing’s nominal plane to calculate the geometric values for the bearing model as demonstrated previously in

Section 4.1.1 (see Figure 4.2). It is seen in Figure 5.8 that the amplitude of the BPFO increases significantly from no fault to 0.002 mm fault case. Moreover, it is demonstrated that the bearing model is sensitive to changes in faults as small as 0.001 mm. Therefore, it is concluded that the motor model (and thus, the bearing model) developed here is capable of predicting the response due to an outer ring bearing fault in terms of the frequency and amplitude of the BPFO.

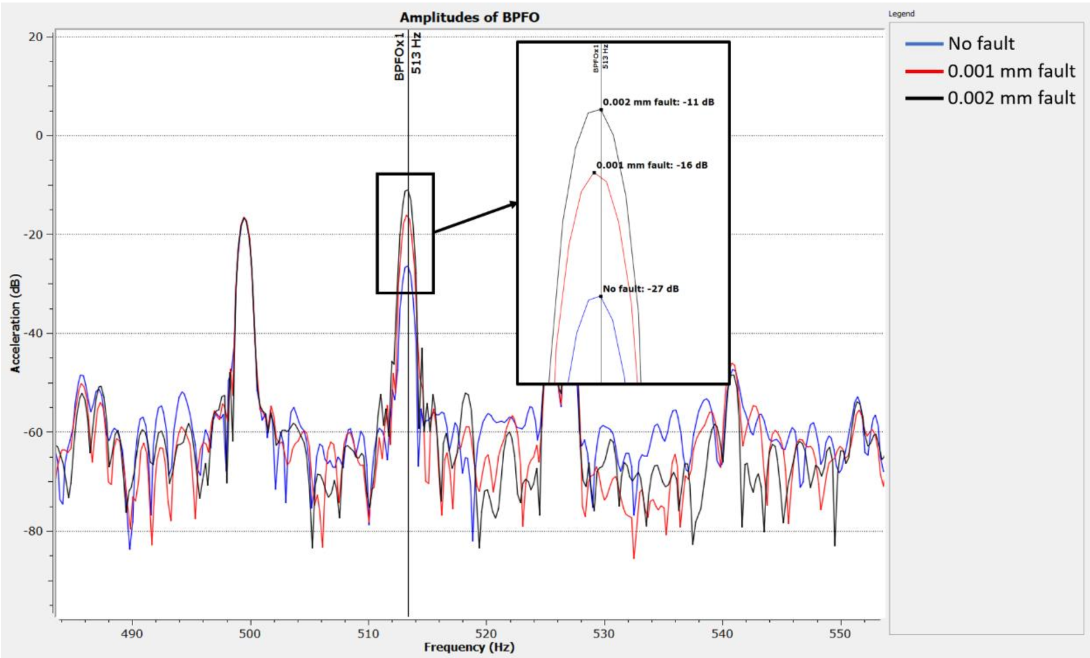

Figure 5.8 : Predicted amplitudes of the ball pass frequency outer race (BPFO) obtained from the motor models with various levels of faults modelled in their bearing models.

Finally, the harmonics of the BPFO are examined. The comparison between the no fault (healthy) model and the 0.002 mm fault (faulty) model is given for the 3rd and the 4th harmonics of the BPFO in Figure 5.9. As seen, the healthy model produces almost no harmonics while the harmonics of the BPFO have significantly higher amplitudes in the results obtained from the faulty model. Hence, it is demonstrated that the model can also predict consistent results in terms of the harmonics of the BPFO as a response to a bearing with a faulty outer ring.

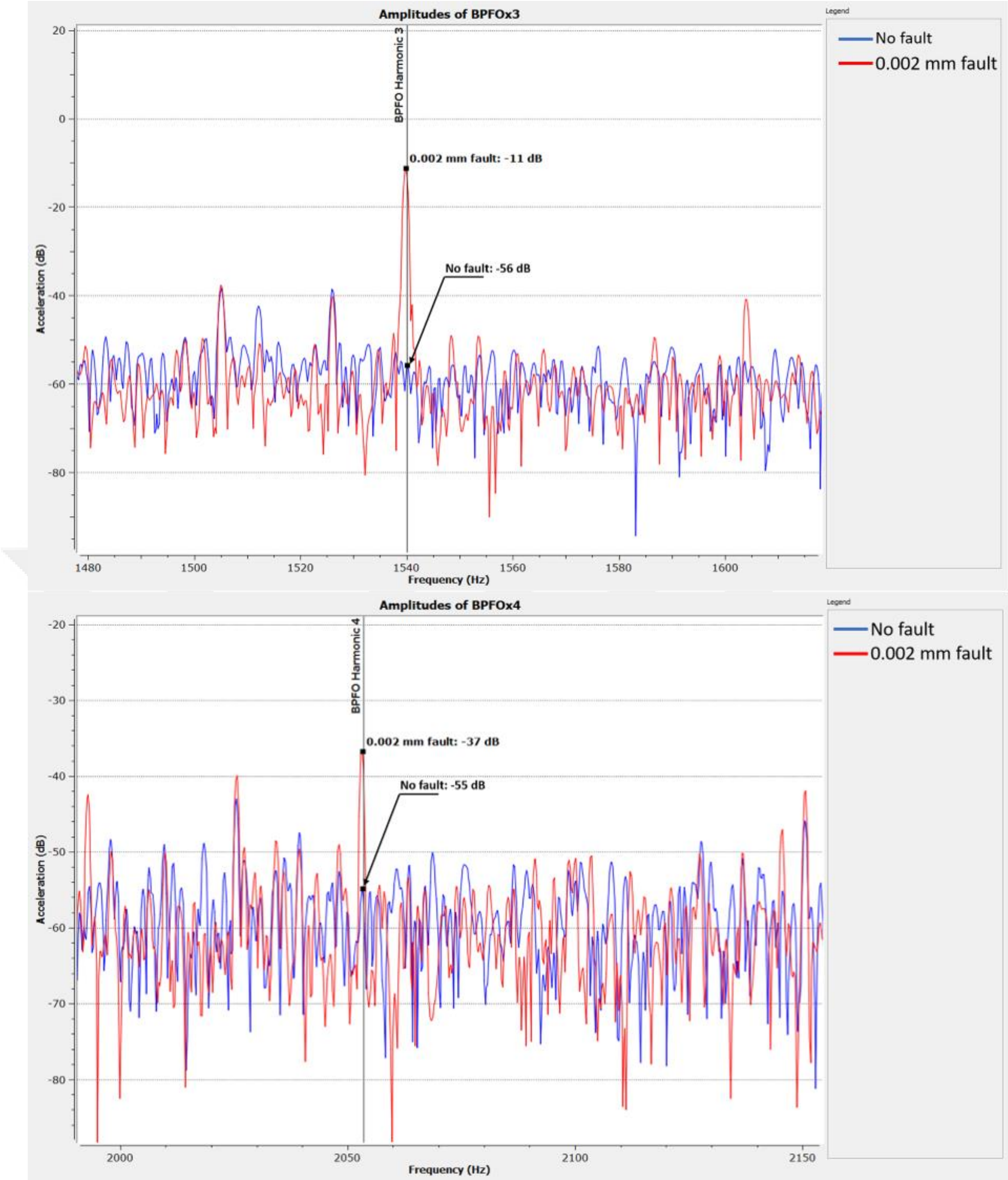

Figure 5.9 : Amplitudes of the third and the fourth harmonics of the ball pass frequency outer race obtained from the healthy and the faulty models.

6. CONCLUSIONS AND SUGGESTIONS FOR FUTURE WORK

6.1 Conclusions

In this thesis, a methodology is presented to model, analyse and experimentally validate the forced vibrations of electric motors. A small brushless DC motor, Atlas, which is manufactured by Arcelik A.S., is selected as the specimen to be used. The study starts with the demonstration of all necessary measurements and tests and then continues with the description of the numerical modelling and the analyses of the Atlas motor. Finally, the numerical results are validated with the experimental results. The most notable findings of this study are stated below:

- It is found that the contact mechanisms between the front cover – stator and the back cover – stator interfaces are rather complex. As demonstrated through frequency response function measurements and numerical modal analyses of the assembly of the covers and the stator, neglecting the friction contacts at these interfaces and assuming that these parts are perfectly joined (welded) together at the matching surfaces in the modelling stage is sufficient to predict the natural frequencies of the assembly with less than 5 percent error within 0 – 3200 Hz range. Although this approach helps reduce the computational cost and modelling time, it is worth stating that that this approach ignores the damping originating from these frictional interfaces, thus adversely affecting the accuracy of forced response level predictions.

- It is demonstrated that modelling the ball bearings with primitive joints or bushing elements do not produce satisfactory results as the nonlinear effects of the ball bearings in the motor are omitted in such linear modelling approach. It is shown through a series of numerical simulations that many higher harmonics of the shaft rotation frequency are created in the acceleration spectra by the nonlinear effects of the ball bearings, which are only represented by a detailed ball bearing model such as the model introduced in this thesis. Additionally, as also demonstrated, some resonance regions of the motor are not excited due to the lack of the excitations by the nonlinear effects when primitive joints or bushings are used to model the bearings.

- It is shown through numerical simulations that the contact angle and bearing clearance strongly affect the frequencies of the sidebands around the shaft rotation frequency and its harmonics. In the previous ball bearing model presented in [25], the contacts between the bearing components were modelled by two-dimensional line contacts rather than three-dimensional area contacts to reduce computational costs and CPU times required for the simulations. Although this approach effectively reduces computational costs, the geometric effects of the contact angle and bearing clearance are ignored in [25]. It is shown in this thesis that the frequencies of the sidebands are not accurately represented when the contact angle and bearing clearance effects are ignored. Furthermore, it is demonstrated that the frequencies of the sidebands are predicted with a level of error about 3 or 4 percent with respect to the experimental results when these geometric effects are included in the bearing model.

In summary, the numerical model of the Atlas motor developed in this thesis is capable of producing results which are in good agreement with the experimental results within 0 – 2700 Hz range, up to 10000 RPM shaft speed.

6.2 Suggestions for Future Work

Although the developed motor model is capable of producing satisfactory results, there are a number of possible improvements that can be made to increase the accuracy delivered by the methodology presented in this thesis. Some of the possible improvements and suggestions for future work are:

- The vibrations of the stator along its axial direction are heavily damped due to the large friction between the laminations. The damping by the friction forces are completely ignored in this model. In order to further improve the accuracy of the results, the damping of the axial vibrations of the stator can be included in the motor model.

- Though the finite element model developed for the assembly of the front cover, the back cover and the stator estimates the natural frequencies of the real assembly with less than 5 percent error, a more detailed modelling of the nonlinear contact mechanisms between the contacting surfaces of these components could increase the accuracy of the model. In this thesis, the nonlinear characteristics of these contacts were neglected.
- It is seen in the numerical Campbell Diagram that, the harmonics above 12X and the sidebands around them are not clearly visible above 2000 Hz. It is demonstrated in this thesis that, detailed modelling of the nonlinear behaviour of the ball bearings are crucial to represent the higher harmonics of the shaft rotation frequency and the sidebands around it. This indicates that the bearing model could be further improved. As stated within the thesis, a number of simplifications and assumptions are made during the development of the bearing model to reduce the modelling time and computational cost. These simplifications and assumptions could be critically reviewed to increase the accuracy of the bearing model, which could offer a more detailed representation of the nonlinear effects.
- The electromagnetic excitations are modelled as combinations of simple harmonic excitations whose frequencies are obtained from the literature. However, a more detailed modelling of the electromagnetic excitations could be employed by defining the mathematical relationships between individual armatures and magnets of the electric motor in the simulations.
- The bearing elements, especially the rings, can be modelled as flexible bodies to include the contribution of the elastic modes of the bearing elements to the vibration of the electric motor.

7. REFERENCES

[1] **Orhan, C., Şanlıtürk, K.Y.**, (2011). *Modeling and forced vibrations for a universal electric motor* (Master's thesis). İstanbul Technical University, Graduate School of Science, Engineering and Technology, İstanbul.

[2] **Low, T. S., Bi, C., Liu, Z. J.**, (1997). A hybrid technique for electromagnetic torque and force analysis of electric machines. *The International Journal for Computation and Mathematics in Electrical and Electronic Engineering*, 16(3), 191–205.

[3] **Ishibashi, F., Noda, S., Mochizuki, M.,** (1998). Numerical simulation of electromagnetic vibration of small induction motors. *IEE Proceedings – Electric Power Applications*, 145(6), 528–534.

[4] **Furlan, M., Cernigoj, A.**, (2003). A coupled electromagnetic-mechanical-acoustic model of a DC electric motor. *The International Journal for Computation and Mathematics in Electrical and Electronic Engineering*, 22(4), 1155–1165.

[5] **Neves, C. G. C., Carlson, R., Bastos, J. P. A.,** (1998). A study on magnetic vibration sources identification in induction motors by FEM simulation and experimental procedures. *IEEE Transactions on Magnetics*, (pp.237 – 242).

[6] **van der Giet, M., Schlensok, C., Schmülling, B., Hameyer, K.**, (2008). Comparison of 2-D and 3-D coupled electromagnetic and structure-dynamic simulation of electrical machines. *IEEE Transactions of Magnetics*, 44(6), 1594–1597.

[7] **Sakamato, S., Hirata, T.,** (1999). Vibration analysis considering higher harmonics of electromagnetic forces for rotating electric machines. *IEEE Transactions of Magnetics*, 35(3), 1662–1665.

[8] **Mohammed, O. A., Liu, S., Ganu, S. C.,** (2002). Computation of transient magneto-mechanical problems in electrical machines. *Proceedings IEEE SoutheastCon*, (pp.187–191).

[9] **Mohammed, O. A.,** (2001). Coupled magnetoelastic finite element formulation of anisotropic magnetostatic problems. *Proceedings IEEE SoutheastCon 2001*, (pp.183–187).

[10] **Hwang, D.-H., Chang, J.-H., Kang, D.-S., Lee, J.-H., Choi, K.-H.,** (2006). A method for dynamic simulation and detection of air-gap eccentricity in induction motors by measuring flux density. *12th Biennial IEEE Conference on Electromagnetic Field Computation*, (pp.69).

[11] **Kobayashi, T., Tajima, F., Ito, M., Shibukawa, S.,** (1997). Effects of slot combination on acoustic noise from induction motors. *IEEE Transactions of Magnetics*, 33(2), 2101–2104.

[12] **Li, Y. B., Ho, S. L., Fu, W. N., Xue, B. F.,** (2009). Analysis and solution on squeak noise of small permanent-magnet DC brush motors in variable speed applications. *IEEE Transactions of Magnetics*, 45(10), 4752–4755.

[13] **Li-xin, X., Yu-hu, Y., Yong-gang, L., Chong-ning, L., Shi-yu, W.,** (2012). Modeling and analysis of planar multibody systems containing deep groove ball bearing with clearance. *Mechanism and Machine Theory*, 56, 69–88.

[14] **Yao, T., Chi, Y., Huang, Y.,** (2012). Research on flexibility of bearing rings for multibody contact dynamics of rolling bearings. *Procedia Engineering*, 31, 586–594.

[15] **Yu, G., Su, M., Xia, W., Wu, R., Wang, Q.,** (2017). Vibration characteristics of deep groove ball bearing based on 4-DOF mathematical model. *Procedia Engineering*, 174, 808–814.

[16] **Yao, T., Xian, L., Wang, L., Liu, X.,** (2017). Multibody contact dynamics on mechanisms with deep groove ball bearing joints. *Journal of Mechanical Science and Technology*, 31(9), 4119–4135.

[17] **Sopanen, J., Mikkola, A.,** (2003). Dynamic model of a deep-groove ball bearing including localized and distributed defects. Part 1: Theory. *Proceedings of the Institution of Mechanical Engineers Part K Multi-body Dynamics*, 217, 201–211.

[18] **Sopanen, J., Mikkola, A.,** (2003). Dynamic model of a deep-groove ball bearing including localized and distributed defects. Part 2: implementation and results. *Proceedings of the Institution of Mechanical Engineers Part K Multi-body Dynamics*, 217, 213–223.

[19] **Çakmak, O., Şanlıtürk, K. Y.,** (2010). A dynamic model of an overhung rotor with deep-groove ball bearings. *The 1st Joint International Conference on Multibody System Dynamics*, Lappeenranta, Finland: May 25–27.

[20] **Wagner, C., Krinner, A., Thümmel, T., Rixen, D.,** (2017). Full dynamic ball bearing model with elastic outer ring for high speed applications. *Lubricants*, 5(2), 17–30.

[21] **Young, H. D., Freedman, R. A., Ford, A. L., Sears, F. W.** (2015). *Sears and Zemansky's university physics: With modern physics*. San Francisco, Pearson Addison Wesley.

[22] **Staelin, D. H.,** (2011). *Electromagnetics and applications*. Cambridge, MA.

[23] **Tiwari, R.,** (2017). *Rotor systems: Analysis and identification*. Florida, Taylor & Francis Group, CRC Press.

[24] **Wensing, J. A.,** (1998). *On the dynamics of ball bearings* (Doctoral dissertation). University of Twente, Enschede, The Netherlands.

[25] **Çakmak, O., Şanlıtürk, K.Y.**, (2010). *Modelling and analysis of rotor-ball bearing systems* (Master's thesis). İstanbul Technical University, Graduate School of Science, Engineering and Technology, İstanbul.

[26] **Aktürk, N., Uneeb, M., Gohar, R.,** (1997). The effects of number of balls and preload on vibrations associated with ball bearings. *Journal of Tribology*, 119, 747–753.

[27] **Harris T. A.,** (1993). *Rolling Bearing Analysis.* Wiley & Sons, New York.

[28] **Taşpınar, O., Şanlıtürk, K.Y.**, (2016). *Rulmanlarda dalgalılık ve rulman titreşimlerine etkisi* (Master's thesis). İstanbul Technical University, Graduate School of Science, Engineering and Technology, İstanbul.

[29] **Kankar, P. K., Harsha, S. P., Kumar, P., Sharma, S. C.,** (2009). Fault diagnosis of a rotor bearing system using response surface method. *European Journal of Mechanics A/Solids*, 28, 841–857.

[30] **Agilent Technologies Inc.,** (1997). *The Fundamentals of Modal Testing (Application note 243-3)*, Agilent Technologies: Santa Clara, CA.

[31] **Url-1** <https://www.mobiusinstitute.com/site2/item.asp?LinkID=2001>, erişim tarihi 03.06.2017.

[32] **Ko, H.-S., Kim, K.-J.,** (2004). Characterization of noise and vibration sources in interior permanent-magnet brushless DC motors. *IEEE Transactions on Magnetics*, 40(6), 3482–3489.

[33] **Hurty, W. C.,** (1965). Dynamic analysis of structural systems using component modes. *The American Institute of Aeronautics and Astronautics Journal*, 3(4), 678–685.

[34] **Bathe, K.-J., Dong, J.,** (2014). Component mode synthesis with subspace iterations for controlled accuracy of frequency and mode shape solutions. *Computers and Structures*, 139, 28–32.

[35] **Craig Jr., R. R., Bampton, M. C. C.,** (1968). Coupling of substructures for dynamic analyses. *The American Institute of Aeronautics and Astronautics Journal*, 6(7), 1313–1319.

[36] **MSC. ADAMS**, Version 2017r2. MSC Corporate Santa Ana, CA – USA.

[37] **Ekşioğlu, M. C., Büyükördek, C., Şanlıtürk, K.Y.**, (2007). *Elektrik motoru yapısal tasarımı* (Bachelor's thesis). İstanbul Technical University, Mechanical Engineering Faculty, İstanbul

CURRICULUM VITAE

Name Surname : **Deniz Bilgili**

Place and Date of Birth : **Balikesir, Nov. 16, 1991**

E-Mail : **dnbilgili@gmail.com**

EDUCATION :

- **B.Sc.** : 2016, Istanbul Technical University, Mechanical Engineering Faculty, Mechanical Engineering Department
- **M.Sc.** : 2018, Istanbul Technical University, Graduate School of Science, Engineering and Technology, Machine Dynamics, Vibration & Acoustics

PROFESSIONAL EXPERIENCE AND AWARDS:

- June 2018 – November 2018: Computation and Simulation Engineer at Mercedes-Benz Türk A.Ş.
- October 2016 – June 2018: Structural Analysis Engineer at Arçelik A.Ş.

PUBLICATIONS, PRESENTATIONS AND PATENTS ON THE THESIS:

OTHER PUBLICATIONS, PRESENTATIONS AND PATENTS:

- **Bilgili D., Kirkayak L., Kirca M.** 2017. The Effects of Intertube Bridging Through Graphene Nanoribbons on the Mechanical Properties of Pillared Graphene, *Composites Part B: Engineering*, 120, 1-9.